



Contents lists available at ScienceDirect

Advances in Colloid and Interface Science

journal homepage: www.elsevier.com/locate/cis

Historical Perspective

Dissipative particle dynamics simulations in colloid and Interface science: a review



Kolattukudy P. Santo, Alexander V. Neimark*

Department of Chemical and Biochemical Engineering, Rutgers, The State University of New Jersey, Piscataway, NJ 08854, United States

ARTICLE INFO

Keywords:

Coarse-grained simulations
Dissipative particle dynamics
Parameterization
Polymers
Surfactants
Nanoparticles

ABSTRACT

Dissipative particle dynamics (DPD) is one of the most efficient mesoscale coarse-grained methodologies for modeling soft matter systems. Here, we comprehensively review the progress in theoretical formulations, parametrization strategies, and applications of DPD over the last two decades. DPD bridges the gap between the microscopic atomistic and macroscopic continuum length and time scales. Numerous efforts have been performed to improve the computational efficiency and to develop advanced versions and modifications of the original DPD framework. The progress in the parametrization techniques that can reproduce the engineering properties of experimental systems attracted a lot of interest from the industrial community longing to use DPD to characterize, help design and optimize the practical products. While there are still areas for improvements, DPD has been efficiently applied to numerous colloidal and interfacial phenomena involving phase separations, self-assembly, and transport in polymeric, surfactant, nanoparticle, and biomolecules systems.

1. Introduction

The power of modern computers has been increasing rapidly every year. Currently, the FUGAKU supercomputer at the RIKEN Center of Computational Science, Japan, is the world's fastest computer with speed of half the exaFLOPS, while the public-distributed folding@home project achieved exascale speed in 2020 to simulate the Spike protein dynamics of SARS-CoV2 virus for 0.1 s [1]. Other powerful resources, such as ANTON can handle millisecond time scales and systems containing up to billions [2] of atoms. The next goal of achieving the exascale computing (10^{18} or 1 quintillion floating point operations per second (FLOPS)) is being boosted up with the \$500 million project of Department of Energy and Argon National Laboratory for building the first exascale super computer AURORA in 2021. However, such powerful resources are not commonly available and cannot meet the growing demands of the current computational material research. Moreover, although parallel computing can facilitate simulations at larger length scales through the domain decomposition, this is associated with longer time simulations to be performed sequentially.

The gold standard in computational materials modelling is the atomistic molecular dynamics (MD) simulations that can model the structural, thermodynamic, and transport properties using *discrete* representation of the systems under consideration, comprised of individual

atoms and molecules, whose collective Newtonian dynamics is solved numerically using efficient algorithms. However, the applicability of atomistic MD is limited to small time and length scales, of the order of a few tens of nanometers and a few hundreds of nanoseconds, with today's typical computational resources. The development of graphic processing units (GPU) have increased computational speed by over an order of magnitude. At the length/time scales of real-life macroscopic objects, the systems possess significant levels of local uniformity and are described by *continuum* models, which consider colloidal and interfacial systems as composed of bulk phases governed by classical thermodynamics and fluid dynamics equations. Between the atomistic and macroscopic scales lies the domain of mesoscopic scales spanning from several nanometers to micrometers and from nanoseconds to microseconds. At the mesoscale, the continuum models break down due to system inherent inhomogeneities, while the discrete atomistic methods become computationally inefficient. Characteristic examples of mesoscale systems include polymeric and surfactant solutions, foams and films, nanoparticles and bio-colloids, lipid membranes and vesicles to name few. The goal of mesoscopic simulations is to bridge the gap between the microscopic atomic scales and the macroscopic continuum scales, which as pointed out by Groot and Warren [3–4], is the '*holy grail*' of theoretical physics.

Mesosopic scales can be approached computationally from either

* Corresponding author.

E-mail address: aneimark@rutgers.edu (A.V. Neimark).

macroscopic continuum or microscopic atomistic representations. From atomistic representation, a mesoscopic model can be derived by a coarse-graining (CG) procedure, in which atoms are grouped into CG particles (beads), and the effective interaction potentials between the CG particles are derived by matching structural and/or thermodynamic quantities with those from atomistic simulations. In this strategy, generally termed as *bottom-up* coarse-graining, the matching quantities include atomic pair distributions, correlation functions, and the like. The interaction CG potentials are obtained as the potential of mean force [5]. Various bottom-up strategies include direct and iterative Boltzmann inversion [6], reverse Monte Carlo [7], force matching/multiscale coarse-graining [8], and variational approaches [9]. Additionally, to arrive at correct dynamics at the mesoscale, the frictional forces between the CG particles can be derived from atomistic simulations by the advanced methods like Mori-Zwanzig projection operator technique [10–11].

The mesoscale description can also be reached from the continuum macroscale by the so-called *top-down* models, which employ mathematically much simple interaction potentials between CG beads chosen to reproduce the experimentally measurable properties, such as pressure, density, compressibility, surface tension, diffusion coefficients, etc. Alternatively, the continuum theories can be extended to incorporate the fluctuations arising from the inherent system discreteness at the mesoscale, by solving the deterministic continuum equations with stochastic flux terms [12]. Such approaches include the fluctuating hydrodynamics (FHD) described by the Landau-Lifshitz-Navier-Stokes (LLNS) equations [13] and similar stochastic treatments on heat equation and on diffusion [14].

There are several popular mesoscale computer simulation methods, which include particle-based off-lattice methods of Dissipative Particle Dynamics (DPD) [4,15–17], Brownian Dynamics (BD) [18] and coarse-grained MD (CGMD) MARTINI models [19], and lattice methods of Lattice Boltzmann [20] (LB) and Lattice Gas Automata [21] (LGA). The conventional DPD model, originally formulated in the seminal paper of Groot and Warren (GW) [7], has found numerous applications in modelling colloidal and interfacial systems due to its computational efficiency. DPD uses pair-wise dissipative forces that lead to conservation of momentum and, therefore, preserves hydrodynamics. DPD models can be made chemically specific [5] using rigorous parameterization procedures, which most often employ both top-down and bottom-up strategies of matching certain atomistic and thermodynamic quantities. Such chemically specific, parametrized DPD models are currently widely employed by the industrial community because of its capability of predicting practically relevant properties that are not

implementation. Section 3 describes the improved versions of DPD, the MDPD, SDPD, FPM, DPDE, reactive DPD as well as methods of dynamic coarse-graining and implementation of solid-fluid boundaries in DPD systems. The main parametrization strategies, including the conventional GW approach and its modifications based on the compressibility matching and mapping onto Flory-Huggins parameters [3–4,41], matching infinite dilution activity coefficients (IDAC) [42], matching water-octanol activity coefficients [22], parameterization schemes with different bead sizes [43–44], and methods for incorporation of electrostatic interactions [45–49], are reviewed in Section 4. Section 5 illustrates the characteristic applications of DPD modelling of thermodynamic, morphological, and transport properties of various colloidal and interfacial systems: surfactant and polymeric solutions, functional nanoparticles, polyelectrolyte and lipid membranes, etc. Overall conclusions are summarized in Section 6.

2. The DPD formulation

2.1. Original DPD model

DPD was originally proposed by Hoogerbrugge and Koelman [15] (HK) as an off-lattice, momentum conserving, Galilean invariant mesoscopic method, the coarse-grained dynamics of which obeys the Navier-Stokes equations and preserve hydrodynamics. Later, Espanol and Warren [17] reformulated the DPD model in terms of a stochastic differential equation,

$$\mathbf{f}_i = \frac{d\mathbf{v}_i}{dt} = \sum_{j \neq i} \mathbf{F}_{ij}^C + \sum_{j \neq i} \mathbf{F}_{ij}^D + \sum_{j \neq i} \mathbf{F}_{ij}^R \quad (1)$$

The right-hand side of Eq. (1) amounts to the total force on the particle i due to pair-wise interactions with other particles in the system via conservative, \mathbf{F}_{ij}^C , dissipative, \mathbf{F}_{ij}^D , and stochastic random, \mathbf{F}_{ij}^R , forces, which vanish beyond an interparticle distance $r_{ij} = R_c$. In addition, the forces depend only on the differences in the particle positions and velocities, $\mathbf{r}_{ij} = \mathbf{r}_i - \mathbf{r}_j$ and $\mathbf{v}_{ij} = \mathbf{v}_i - \mathbf{v}_j$ which ensure the Galilean invariance. The particle motion obeys Newton's equation,

$$\frac{d\mathbf{r}_i}{dt} = \mathbf{v}_i; m_i \frac{d\mathbf{v}_i}{dt} = \mathbf{f}_i \quad (2)$$

where the mass of the particles m_i is assumed to be unity. The conservative force is presented as a simple soft-core potential, which is the key feature of DPD that makes it computationally efficient, allowing for large time steps and increased computational speed. This potential is repulsive,

$$V_{ij}(r_{ij}) = \frac{1}{2} \sum_j a_{ij} \left(1 - \frac{r_{ij}}{R_c}\right)^2; \mathbf{F}_{ij}^C(r_{ij}) = a_{ij} \left(1 - \frac{r_{ij}}{R_c}\right) \hat{\mathbf{r}}_{ij}, \text{ for } r_{ij} \leq R_c \text{ and 0 otherwise.} \quad (3)$$

readily available experimentally [4,22–25].

The DPD method has been expanded in its theoretical framework and applicability in the past two decades that has been documented in several reviews [26–28]. Important improvements of the conventional GW model include many-body DPD (MDPD) [29–30], smooth dissipative particle dynamics (SDPD) [31–32], Fluid Particle Model (FPM) [33], DPD with energy conservation (DPDE) [34–37] and reactive DPD approaches [38–40]. In this review, we present a detailed critical description of the DPD methodology focusing on the DPD models formulation, parameterization, and its applications in various colloidal and interfacial systems.

The paper is organized as follows: In Section 2, we present a concise description of the original DPD model along with its numerical

Here, a_{ij} is the conservative repulsion parameter, and $\hat{\mathbf{r}}_{ij} = \mathbf{r}_{ij}/r_{ij}$ is the unit vector along the distance vector \mathbf{r}_{ij} . The cut-off distance of the repulsive potential, R_c , determines the coarse-graining scale and represents the effective diameter of the beads. Note that this scheme implies the equal size of all the beads representing different components. Using the soft-core conservative potential is justified on a mesoscopic scale. It is an effective potential between the groups of several hard-core (Lenard-Jones type) atoms that is, as many studies confirm, essentially soft [50]. However, the choice of \mathbf{F}_{ij}^C in the linear form (Eq. (3)) is by no means mandatory. In fact, an all-repulsive conservative interaction between the beads essentially means that the vapor-liquid coexistence cannot be

simulated in DPD [4], as there is no attractive force in the system that would keep the liquid particles from escaping into the space. This deficiency is addressed by many-body DPD [29] (MDPD, see below) with the use of a density-dependent many-body conservative potential with attractive and repulsive terms. Meakin and coworkers [51] introduced F_{ij}^C with short-range repulsive and long-range attractive conservative forces.

The random and dissipative forces constitute the DPD thermostat and are given by,

$$F_{ij}^D = -\gamma w^D(r_{ij}) \left(v_{ij} \cdot \hat{r}_{ij} \right) \hat{r}_{ij}; F_{ij}^R = \sigma w^R(r_{ij}) \theta_{ij} \hat{r}_{ij}, \quad (4)$$

where θ_{ij} is a Gaussian white noise with zero mean, w 's are the weight functions that depends only on r_{ij} . DPD can be viewed as CGMD with soft conservative inter-particle interactions (Eq. (3)) coupled with the DPD thermostat (Eq. (4)). The DPD thermostat, like the Langevin thermostat, conserves temperature, since whenever any increase in the noise causes heating up the system, the dissipative forces also increase, slowing down the system to bring back to the given temperature. If θ_{ij} is chosen to be symmetric ($\theta_{ij} = \theta_{ji}$), then Eq. (4) provides a *pair-wise Brownian dashpot* [28] (Fig. 1) that ensures the momentum conservation. The dissipative

$$r_i(r + \Delta t) = r_i(t) + \Delta t v_i(t) + \frac{1}{2}(\Delta t)^2 f_i(t)$$

$$\bar{v}_i(t + \Delta t) = v_i(t) + \lambda \Delta t f_i(t) f_i(t + \Delta t) = f_i(r_i(t + \Delta t), \bar{v}_i(t + \Delta t)) v_i(t + \Delta t) = v_i(t) + \frac{1}{2} \Delta t (f_i(t) + f_i(t + \Delta t)) \quad (6)$$

force is like a dashpot damping the fluctuations caused by the random force that accounts for the Brownian motion. Espanol and Warren [17] considered the Fokker-Plank equation governing DPD and noted that the steady-state solution should essentially lead to the equilibrium distribution in the Gibbs canonical ensemble, which implies the following relationships between the amplitudes and weight functions of random and dissipative forces,

$$w^R = \sqrt{w^D}; \sigma = \sqrt{2\gamma k_B T} \quad (5)$$

Eq. (5) represents the *fluctuation-dissipation theorem*, which relates the stochastic and dissipative parameters [4,17]. This relationship essentially allows one of the weight functions to be arbitrary. Groot and Warren [4] (GW) used $w^R(r_{ij}) = 1 - r_{ij}/R_c$ for $r_{ij} < R_c$ which has been generally used in DPD simulations since then. The friction coefficient, γ , determines the value of the random force amplitude, σ . Note that the

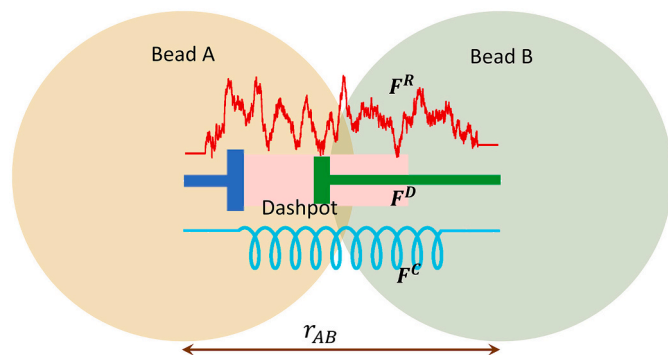


Fig. 1. The pairwise forces between two DPD particles. The conservative force is harmonic and is represented by the spring. The dissipative force is the dashpot that dampens the effects of the random force that accounts for the Brownian motion, and hence they together form the Brownian dashpot. (For interpretation of the references to color in this figure legend, the reader is referred to the web version of this article.)

dissipative force in Eq. (4) is zero when the radial vector r_{ij} is perpendicular to the relative velocity v_{ij} . This excludes shear forces between any pair of particles, while the effective shear results from the coupling of interactions between several particles. The inclusion of pair-wise shear forces led to subsequent development of the Fluid Particle Model (FPM, see below) [33].

2.2. Numerical implementation

In general, the velocity Verlet [52] algorithm, which possesses time-reversibility is used in MD simulations, often termed *md-vv*. Groot and Warren [4] introduced a modified velocity Verlet algorithm for numerical integration of the DPD equations of motion. The Euler method used previously [15,17], is avoided in MD simulations due to a lack of time-reversibility although this is not much a problem in DPD. Numerical integration is more problematic for DPD than MD due to the dependence of forces on velocities and vice versa. The GW scheme differs slightly from the usual velocity-Verlet algorithm and utilizes a parameter λ to deal with the velocity dependence of forces,

In Eq. (6), the mass of the particles is assumed unity, as stated before. This algorithm predicts the velocities at $t + \Delta t$ and then corrects it in the later step (*predictor-corrector* approach). The parameter $\lambda = 0.5$ corresponds to usual *md-vv*, otherwise, it represents a ‘tuning parameter’ used to account for the effects of stochastic forces. GW [4] reported the optimum value of $\lambda = 0.65$, that can be used with a certain range of timesteps. In addition, the random force requires inclusion of an extra $\Delta t^{-1/2}$ to account for the correct measure for the Gaussian noise upon discretization [4],

$$F_{ij}^R(r_{ij}) = \sigma w^R(r_{ij}) \theta_{ij} \Delta t^{-1/2} \hat{r}_{ij} \quad (7)$$

However, this scheme does not completely remove the artifacts that arise with the velocity-dependent forces. For instance, as cautioned earlier by Marsh and Yeomans [53], the time-step dependence of major structural and thermodynamic quantities, such as temperature, radial distribution functions and pressure [54–55], may occur in the simulations, and unphysical system configurations may appear at large timesteps [56]. To avoid these shortcomings, some level of self-consistency needs to be achieved between the forces and velocities at each time-step. Novik and Coveney [57], analyzed the performance of different finite-difference schemes of DPD, including Euler (HK), velocity Verlet (GW) and Runge-Kutta methods and found the GW method most suitable for DPD simulations, with a better performance at $\lambda = 0.5$ than at $\lambda = 1.0$. Later, several alternative integration schemes were suggested to improve the DPD simulations. Among them are the self-consistent leapfrog scheme by Pagonabarraga et al. [58], the *DPD-vv* scheme by Gibson et al. [59], algorithm of den Otter and Clarke based on stochastic dynamics [60], Shardlow splitting method [61], Trotter integration schemes of Serrano et al. [62] and Thalman and Farrago [63], and Lowe’s method [64]. Nikunen et al. [54] investigated the performance of these approaches and found that the splitting algorithm of Shardlow and Lowe’s method are superior. For the hybrid models of polymers, where the polymers are described by hardcore potentials and the solvent by soft potentials, time-staggered schemes were suggested by Symeonidis et al. [65]

Lowe's method does not suffer from the artifacts caused by the velocity dependence of the dissipative force, because it does not use the DPD thermostat. The systems with CG atoms interacting with DPD conservative soft forces are thermo-stated in a momentum conserving fashion, similar to the momentum conserving Anderson thermostat [66] (so named as Lowe-Anderson thermostat). The Lowe-Anderson thermostat is particularly useful in overcoming the well-known Schmidt number problem of DPD. The Schmidt number (S_c) of liquids, which is the ratio of kinematic viscosity to the mass diffusivity is in the range of 1000s for normal liquids but is of the order of 1 in DPD, which has been shown to affect several non-equilibrium properties of polymer solutions [67]. With Lowe's method, S_c can be increased to the realistic values. Peters [68] suggested a generalized Lowe's thermostat. Stoyanov and Groot [69] introduced a combined use of a Galilean invariant Nose-Hoover thermostat and Lowe-Anderson thermostat (NHLAT) and reported a better computational efficiency compared to the standard DPD thermostat. Recent advances also include developments of a pairwise adaptive Langevin thermostat [70] and inclusion of damping along the perpendicular components of the particle relative velocity [71].

3. Advances of the DPD method

3.1. Smoothed dissipative particle dynamics

Although the original DPD method was introduced as a top-down approach in order to address the problem of scale bridging, it cannot provide a direct link to the mesoscale either from atomistic or from continuum length and time scales. An ensemble of collectively moving DPD particles lacks a clear statistical mechanical base and a unique mapping [72]; as the soft potentials between the particles representing packets of fluid generally fail to reproduce the correct structure and virial pressure simultaneously. Flekkoy et al. [73–74] introduced a bottom-up procedure of DPD coarse-graining starting from the atomistic MD systems using the Voronoi tessellation with dissipative particles corresponded to the Voronoi cells of variable shapes, masses and sizes, instead of spherical particles implied in the standard DPD framework. Serrano and Espanol [75] devised a thermodynamically consistent fluid particle model as a top-down model, by a finite volume Lagrangian discretization of the hydrodynamic equations using Voronoi tessellation. Subsequently, Espanol and Ravenga [32] introduced smoothed dissipative particle dynamics (SDPD), by combining the elements of Smoothed Particle Hydrodynamics (SPH), a discretized macroscale model for Navier-Stokes flow, originally proposed to study astrophysical problems, with the thermal fluctuations in DPD, incorporated in the GENERIC (General Equation for Non-Equilibrium Reversible-Irreversible Coupling) framework of Ottinger [76]. Starting with the Lagrangian hydrodynamic equations, SDPD employs a finite volume discretization procedure of SPH, describing as a system of fluid particles with physical variables represented in terms of an interpolant (smoothing) bell-shaped weighting function. The dissipative terms are then introduced, into the deterministic dynamics of SPH, leading to fluctuating hydrodynamics. The Voronoi fluid particle model has computational complexities due to the tessellation procedures, however, the computational efficiency of SDPD is restricted due to a requirement of a larger neighbor list [28,77]. SDPD can be considered as a top-down model that provide scale bridging between molecular and continuum scales. It can also support multiscale description of the system, with subdomains of different resolution [78]. SDPD has been successfully applied to various problems such as, dynamics of polymer solutions [79] suspensions of particles [80], phase-separating liquid mixtures [81], blood flow [82] and movement of micro/nanoparticles in blood [83], while additional extensions [84] include multicomponent systems [85] and incorporation of angular momentum conservation [86].

3.2. Fluid particle model

FPM developed by Espanol [33] is based on the Voronoi tessellation of continuum fluid. The coarse-graining is performed by introducing a set of randomly distributed mesoscopic fluid particle centers and grouping the fluid atoms within nearest particle centers. The resulting Voronoi cells of variable sizes and shapes represent the coarse-grained particles, as packets of fluid specified by their position, linear and angular velocities. The CG particles interact with each other by conservative, friction and stochastic forces in the DPD style, except for the friction forces, which include additional shear terms. The FPM friction force has contributions from translational and rotational motion of the fluid particle,

$$\begin{aligned} F_{ij}^{Trans}(r_{ij}) &= -\gamma m M^T(r_{ij}) \mathbf{v}_{ij}; \\ F_{ij}^{Rot} &= -\gamma m M^R(r_{ij}) \left(\mathbf{r}_{ij} \times \frac{\boldsymbol{\omega}_i + \boldsymbol{\omega}_j}{2} \right) \end{aligned} \quad (8)$$

Here, m is the mass of the fluid particles and $\boldsymbol{\omega}_i$ are the angular velocities. Note that the pair-wise definition of angular forces leads to conservation of angular momentum. The matrices M^T and M^R have the forms,

$$M^T(r_{ij}) = A(r_{ij})\mathbf{I} + B(r_{ij}) \hat{\mathbf{r}}_{ij} \hat{\mathbf{r}}_{ij}; M^R(r_{ij}) = C(r_{ij})\mathbf{I} + D(r_{ij}) \hat{\mathbf{r}}_{ij} \hat{\mathbf{r}}_{ij} \quad (9)$$

The dimensionless coefficients A , B , C and D represent contributions from various linear and angular friction components. $A(r_{ij})$ is the range of the frictional force in the direction of the relative velocity \mathbf{v}_{ij} , which corresponds to the shear forces, while the $B(r_{ij})$ corresponds to the common DPD frictional force that vanishes when \mathbf{r}_{ij} and \mathbf{v}_{ij} are normal to each other. $C(r_{ij})$ gives rise to the frictional force at the *surface* of the particle when it rotates. $D(r_{ij})$ is actually zero and is included for a convenient mathematical formulation. FPM improves the simple frictional forces used in DPD. FPM has been successfully applied to study dynamics of aggregation of red blood cells [87], fibrin aggregation in the blood [88], where the fluid particles are simulated along with solid particles to provide the elastic frame work to keep the cell shape and colloidal agglomeration [89]. The same group also implemented efficient parallelization to handle several millions of particles [90].

3.3. Many-body DPD

The soft, slowly varying conservative potential of DPD has the disadvantage that it leads to an equation of state (EOS) that is quadratic in density [4] and rules out the possibility to having phase coexistence within a pure single component system. Using the density-functional theory, Pagonabarraga and Frenkel [91] introduced MDPD with density-dependent conservative potentials. MDPD was subsequently extended to multicomponent systems by Trofimov et al. [92] In MDPD, the conservative potential has the form [29,93],

$$F_{ij}^C(r_{ij}) = A_{ij} W_c(r_{ij}) \hat{\mathbf{r}}_{ij} + B_{ij} \left(\frac{\bar{\rho}_i}{\bar{\rho}_i + \bar{\rho}_j} \right) W_d(r_{ij}) \hat{\mathbf{r}}_{ij} \quad (10)$$

Here, the first term represents an attractive interaction with $A_{ij} < 0$, while the second term is repulsive $B_{ij} > 0$. $W_c(r_{ij}) = 1 - r_{ij}/r_c$ and $W_d(r_{ij}) = 1 - r_{ij}/r_d$, where r_c and r_d respectively are the interaction ranges of attractive and repulsive interactions, with $r_d < r_c$. The local density functions $\bar{\rho}_i$ are given by [29,93]

$$\bar{\rho}_i = \sum_{j \neq i} w_\rho(r_{ij}) = \sum_{j \neq i} \frac{15}{2\pi r_d^3} \left(1 - \frac{r_{ij}}{r_d} \right)^2 \quad (11)$$

The weighting function w_ρ vanishes for $r > r_d$, and is normalized [29]. MDPD leads to an EOS that is a cubic pressure-density relation and has the potential to exhibit vapor liquid coexistence [29].

Warren [29–30] used MDPD to model the vapor-liquid coexistence and late stage of bubble coarsening during the phase transition. Two-

phase flow involving vapor and liquid phases was modelled by Tiwari and Abraham [94]. Surface properties of MDPD fluid were investigated by Arenti et al. [95], and Ghoufi and Malfreyt [96]. Atashafrooz and Mehdipour [97] studied the vapor-liquid coexistence curve of sodium. A recent review of MDPD simulations is given by Ghoufi et al. [98]

3.4. DPD with energy conservation

The original DPD implies the isothermal (NVT) canonical ensemble governed by the random and dissipative forces in the equations of motion that act as the DPD thermostat. The incorporation of the energy conservation into DPD was introduced by Avalos and Mackie [34], and Espanol [36] by defining an additional internal energy variable u_i , which obeys stochastic equations that describe mesoscopic heat flow between the particles. The pair-wise dissipation causes increase in the internal energy by rising the particle temperature θ_i , while the random forces cause cooling down the particle decreasing u_i . The temperature difference between the particles ($\theta_i - \theta_j$) induces the heat flow. Note that u_i contains the degrees of freedom within the fluid particle that can store energy, which is not explicitly described in the DPDE model. In a later work, Espanol and coworkers [99] introduced an energy conserving coarse-graining scheme with the CG model equivalent to DPDE. More recently, Avalos et al. [100] introduced a refined generalized DPDE (GenDPDE) approach, where the particle internal energy variables, u_i , are local density and temperature-dependent. Adopting a bottom-up definition of particles based on the Voronoi tessellation, GenDPDE defines particle thermodynamics with the particle local density and particle temperature as entangled fluctuating variables, while in DPDE, the forces depend entirely on the particle separation distance. Density-dependent potentials improve transferability and accuracy beyond parametrization, by incorporating many-body effects.

The DPDE model has been used to study thermal conductivity [34–35], phase change in materials [101], melting of solid particles under shear flow [102], heat conduction in nanocomposites [103] and nanoparticle suspensions [72], convection heat transfer [104], high explosives [105] and shock wave effects on lipid membranes [106]. Chaudhri et al. [107] extended DPDE to study multicomponent systems. Pastewka et al. [108] developed another energy conserving DPD method that is equivalent to DPDE. It is worth noting that the extension of DPD to other isothermal ensembles such as NPT and NP_{NT} (constant surface tension ensemble used for modelling lipid membranes) involves the introduction of a barostat, like in the Langevin piston method [109]. Trofimov et al. [110] simulated constant pressure MDPD by coupling to the Anderson barostat. Coupling DPDE to a barostat leads to the isenthalpic DPD or DPDH [111]. Several studies report DPD simulations in the grand canonical ensemble [112–113].

3.5. Boundary conditions in DPD

DPD simulations of hydrodynamic flows, like the flow of suspensions of solid nanoparticles or motion of fluids through microchannels and porous media, often involve solid boundaries or walls. In their original works, Hoogerbrugge and Koelman studied fluid flow through an array of cylinders [15] and flow of suspensions of hard spheres under shear [16]. To simulate a patch of a large system, periodic boundary conditions are employed. For non-periodic systems, such as Couette or Poiseuille flows, the boundary conditions have to be carefully imposed. For instance, for a particle that is close to a non-periodic boundary, the interactions beyond the boundary are cut that leads to an imbalance in interactions with other particles, causing an increase of fluid density near the boundary and subsequent layering. Additional boundary forces have to be used to avoid the density fluctuations. Such boundary forces can be derived for regular walls such as planar or spherical, but not for boundaries with complex geometries. A physically-based and convenient method that works for all geometries is to use the walls built of frozen DPD particles. However, the CG soft potential cannot reproduce

the specifics of wall-particle interactions unless carefully parameterized reproducing underlying realistic wall characteristics. As a result, there are two major problems in using frozen DPD walls in flow simulations: (1) the soft potentials will allow permeation of fluid particles into the walls and (2) the all-repulsive forces between particles cause slip of the flow near the walls. The slip is not completely unrealistic, as it can really occur in microfluidic flow at large contact angles between the fluid and the wall, such as water flow in super hydrophobic channels [114]. To impose impenetrability of the walls, algorithms such as specular, bounce-back, or Maxwell reflections have been used, while to avoid the slip, several no-slip boundary conditions have been suggested [102,115–128]. Nevertheless, implementing effective wall boundaries in DPD is still challenging.

To generate a Couette flow with a linear velocity profile across the system, sliding walls at the boundaries may be used. The Lees-Edwards boundary conditions [115], in which the effects of the sliding walls is incorporated as a special boundary condition, is efficiently utilized to analyze the rheology of suspensions [129–130], and metal-complexed polymer solutions [131]. In this approach, the neighboring periodic cells in the Y direction are set to move in the X-direction with respect to the central simulation cell, with a speed V_d that corresponds to the specified shear rate. This will create a velocity gradient in the Y direction, given by,

$$v(y) = V_d \left(\frac{y}{L} - \frac{1}{2} \right) \quad (12)$$

where L is the length of the cell in Y-direction. V_d is specified by the desired shear rate $\gamma_s = \partial v(y)/\partial y = V_d/L$. Backer et al. [116] suggested a reverse Poiseuille flow method to model effects of wall and measure viscosity of fluids. Revenga et al. [117] calculated the effective boundary forces assuming that the walls consist of frozen DPD fluid particles and the impenetrability of the walls is imposed by the bounce-back boundary conditions. However, this method showed strong density fluctuations near the walls. Several authors [119,122] used frozen solid walls with additional strategies to secure no-slip boundary conditions, such as increasing the wall density [123], and the wall repulsive force [124], enforcing a random velocity distribution with zero mean in the thin layer near the solid wall [122], by tuning the wall-fluid force to adjust with the force exerted by the fluid on the wall [125], imposing bounce-back velocities on the fluid particles upon entering the wall [127] and utilizing a phase field function to reproduce the sharp wall-fluid interface [128].

3.6. Reactive DPD

Modelling of chemical reaction in DPD is challenging as it involves decomposition of molecules with formation and dissociation of chemical bonds that leads to changes in the structure and thermodynamic variables such as temperature and energy. Lisal et al. [38–39] devised reaction ensemble dissipative particle dynamics (RxDPD) to model reaction equilibrium of polymeric systems. This approach combined elements of DPD to account for the dynamics and reaction ensemble Monte-Carlo (RxMC) to model the polymerization reactions, utilizing the concept of the *fractional particle* that was introduced by Cagin and Pettitt [132]. To describe polydisperse systems containing polymers of type A (say) at reaction equilibrium, $A_i \rightleftharpoons A_{i+1}$, DPD systems contained the *full* polymers A_i and one ‘fractional polymer’ fA_n that has a fractional particle at one of its ends. The fractional particle serves as a potential polymerization or depolymerization site, and the fractional polymer can become full polymer with increase or decrease of chain length by one, depending on the value of the parameter λ that couples the fractional particle to the system. The changes of coupling parameter λ can be introduced either by performing *random* changes with acceptance determined by the transition probability derived from a grand canonical partition function (RxDPD(τ)), or by solving the *deterministic* equations

of motion corresponding to an extended DPD Lagrangian that includes the fractional particle variables (RxDPD(d)).

The RxDPD method was demonstrated to consistently describe the effects of system density and the polymer conformational and diffusion properties on the polydispersity. Subsequently, an alternative formulation of RxDPD was developed to model reaction equilibrium of supramolecular diblock copolymers (SDC), $A_n + B_m \rightleftharpoons A_n B_m$. In this formulation, the changes in the coupling parameter λ are accepted with a transition probability derived from an *expanded ensemble* [133] grand canonical partition function, which is computationally more efficient in this case. This approach was used to demonstrate the rich phase behavior of several SDC systems. Note that due to the use of fractional particles, the total momentum of the system is only partially conserved; RxDPD is a robust method to describe thermodynamic equilibrium, but the hydrodynamic behavior is not properly accounted for.

Another approach of reactive DPD, DPD-RX, was developed within the DPDE or DPDH framework, in which the reaction process is described implicitly, without explicitly describing the bond formation or breaking. The method was introduced by Stoltz and coworkers [134] for modelling shock and detonation waves and shock-induced detonation reaction in explosives. Each molecule is described as a *CG reactor* particle [40] obeying DPDE or DPDH equations of motion with additional variables describing the *extent-of-reaction* and the energy u_i^{chem} that is associated with the changes in chemical composition. The changes in chemistry of the particle are governed by a chemical reaction mechanism and kinetics, according to a reaction model. DPD-RX was efficiently applied to shock-to-detonation transition of liquid nitromethane, and shock-wave induced energy exchange between inter and intramolecular degrees of freedom in crystalline 1,3,5-triamino-2,4,6-trinitrobenzene (TATB) [135]. DPD-RX was also applied to decomposition of cyclotrimethylene trinitramine (RDX) by Lisal and coworkers [40].

Reactive DPD models that utilizes Morse type potentials have been developed to model reversible links such as hydrogen bond and metal complexation. The Morse potential was first introduced in DPD by Vishnyakov et al. [136] for modelling protein conformations, and later applied for modelling dissociation and proton transport in polyelectrolytes [137–140], hydrogen bonding [136,141], and metal coordination in polymeric solutions [131,142–143]. The general form of the Morse potential represents a potential well,

$$u_M(r, r_0) = K_M \{ \exp[-2\alpha_M(r - r_0)] - 2\exp[-\alpha_M(r - r_0)] \} \quad (13)$$

where K_M is the attraction strength, r_0 is distance at the energy minimum and α_M is the curvature at the potential energy minimum. Eq. (13) is truncated and smoothed at an interaction cut off R_M . Several examples of the application of the Morse potential in DPD systems are illustrated below (Section 5).

3.7. Bottom-up derivations

The basic formalism of DPD [4,17] was suggested as an ad hoc method, with no clear connection between either macroscale or microscale system specifications. GW and others [22–23,44,144–145] presented it as a top-down approach suggesting parametrization schemes based on matching quantities such as solvent density, compressibility, etc. and utilizing Flory-Huggins parameters, to bridge the macroscopic and mesoscopic scales. Bottom-up approaches that connect DPD to atomistic MD simulations results were also developed [73–74,146–154]. Rigorous derivations and parametrization, however, are possible only for simple fluid systems. Practical parameterization of complex fluids involving polymers or multicomponent systems requires hybrid methods that combine both top-down and bottom-up procedures with some parameters determined from matching the atomistic properties revealed in *ab-initio* [155–156] or MD simulations [42,139,143,155,157–159] and other parameters determined from matching the macroscopic properties.

Static equilibrium properties of a CG system can be mapped from its microscopic description using standard coarse-graining procedures [5] of calculating the potential of mean force, like iterative Boltzmann inversion [6], inverse Monte Carlo [7], force matching [8], minimum relative entropy [9] and other methods. In fact, a substantial amount of literature exists for such parametrization of the CG potentials in polymeric and biomolecular systems [5,155,160–161]. Such CG potentials can account for the conservative part of the CG force field, and reproduce the structural and equilibrium properties, such as the radial distribution functions, with respect to the reference atomistic MD simulations. However, such procedures are insufficient for modelling the dynamic properties, such as diffusion coefficients and velocity autocorrelation functions (VACFs). The averaging out the fast degrees of freedom results in a dynamics that is too fast compared to reality, and one needs to rescale the simulation time to correlate with the diffusion and transport properties of the reference atomistic system. A dynamically correct, fully-coarse-grained model requires a re-parametrization of the dissipative and random forces; the corrected frictional force should account for the effects of the averaged out fast degrees of freedom on the motion of CG particles.

Several attempts in the literature addressed the bottom-up derivation and parameterization of conservative and dissipative forces in DPD models [73–74,146–147,149,151–154,162–165], in which the meso-scale DPD model is systematically derived from the corresponding microscopic atomistic representation. A rigorous dynamic coarse-graining can be done with the Mori-Zwanzig (MZ) projection operator technique [10–11] that was originally formulated to derive Generalized Langevin Equation (GLE) from the microscopic system trajectories. MZ-DPD was derived for harmonic chains and lattices by Espanol and others [146–147,149,151–154]. Espanol [146] considered harmonic chains on a one-dimensional lattice and derived equations of motion for relevant mesoscopic coarse-grained variables from the microscopic description of atoms connected by harmonic springs. The harmonic lattice, representing an elastic solid system, was found to obey the same frictional and random force laws as in the DPD fluid systems. Cubero and Yaliraki [147] pointed out that Non-Markovian effects can be present in the initial formulation of harmonic chains, while Hijon et al. [151], showed that these non-Markovian effects become suppressed for *nonlinear chains* that interact with non-linear potentials such as Lenard-Jones and therefore Markovian assumption is appropriate for realistic systems. Later, Hijon et al. [153] showed that the MZ procedure can be tuned to obtain the Markovian GLE to derive full CG dynamics. Kinjo and Hyodo [152], derived equations of DPD and BD using the projection operator technique. Li et al. [154] compared 3 MZ-DPD models for star polymers differed by inclusion non-radial interactions between the CG beads, with standard DPD model and reported excellent and much better agreement of MZ-DPD models with MD systems, compared to the conventional DPD model. MZ-DPD was applied to account for non-Markovian effects in the chain dynamics of polymer melts [166]. Trement and coworkers [167] employed the projection operator technique to develop fully coarse-grained models of n-alkanes and obtained a dynamically consistent CG model for n-pentane that correctly reproduces self-diffusion and viscosity coefficients. Several other dynamic coarse-graining methods [168–169] were suggested based on minimization of the relative entropy [9] and Bayesian optimization [170].

3.8. Advanced modifications of DPD

3.8.1. Single particle DPD

In DPD simulations, large colloidal particles are represented as collection of several tens or hundreds of interconnected DPD particles. While this increases the computational load, such particles overlap with solvent particles due the soft nature of the DPD forces that allows for applying the standard computational scheme. Single particle DPD was developed by Pan et al. [171–172], to study the rheological properties of suspensions of colloidal particles. This method represents solid particles

as single DPD particles that are bigger than the solvent beads and experiences non-central shear dissipative forces. This approach draws some comparison with FPM, which includes similar contributions to the drag force. In single particle DPD, the drag force term includes both rotational and translational components, while the conservative interactions between the solid particles and between solid particles and the solvent beads are modelled by exponential forces, referred to as hard-core DPD forces

$$F_{Sj}^c = \frac{a_{Sj}}{1 - e^{-b_{Sj}}} \left(e^{-\frac{b_{Sj}r_{ij}}{R_c}} - e^{-b_{Sj}} \right) \quad (14)$$

where S represents the solid particle type, while a_{Sj} and b_{Sj} are parameters. Introduction of hard-core conservative forces prevents unphysical overlap between the solid particle and other beads. Pan et al. [171] reported that the use of this force, although at the expense of much smaller timesteps, resulted in the rheological properties in agreement with experimental data. The hard-core potential, Eq. (14), has been used for modelling rheology of dilute bubble suspensions [173] and surfactant adsorption on gas-liquid interfaces [174].

3.8.2. N-varied DPD

N-varied DPD with varying number of particles was developed by Hong et al. [175] to simulate the budding (protrusion) dynamics of the domains within multicomponent lipid membranes. This phenomenon occurs due to the domain line tension, which causes the membrane geometry to deviate from the ideal planar configuration. To model the process of membrane corrugation, neither the NVT ensemble nor the constant surface tension ensemble computations are applicable. In the N-varied approach, lipid molecules are added to the corrugating membrane during the simulation to keep the local lipid density constant, while the lateral dimensions of the system remain fixed with the *quasi-periodic* boundary conditions, in which the periodic boundary conditions are applied along with lipid addition and removal. This approach was subsequently applied to investigate the membrane curvature effects due to anchored proteins [176], and nanoparticle-membrane interactions [177].

4. DPD parametrization

Extensive applications of DPD in studying various soft matter systems necessitated the development of various strategies to systematically parameterize the CG potentials, in order to correctly reproduce the mesoscale system dynamics. Below, we provide a review of the DPD parameterization methods based on the conventional GW formulation of DPD and its modifications that are employed for modelling colloidal and interfacial systems.

4.1. The GW approach and its modifications

4.1.1. The equation of state

Groot and Warren [4] formulated a systematic parameterization scheme for DPD simulations, based on a *top-down* approach, which has become the conventional DPD model widely used for modelling various systems of practical interest. The GW model implies the soft-core linearly decaying conservative repulsion forces according to Eq. (3) with equal bead size R_c for all system components. The key requirement in this approach is that the density fluctuations in the system are correctly described in order to reproduce the correct thermodynamics. In a single component system, this is done by matching the isothermal compressibility κ_T . The bead density ρ is constant throughout and is expressed in reduced units ($R_c = k_B T = 1$). GW considered pressure of the system in the *virial* form, formulated in more detail by Maiti and McGrother [144]

$$p = \rho k_B T + \frac{1}{6V} \sum_{i \neq j} \langle \mathbf{r}_{ij} \cdot \mathbf{F}_{ij}^c(r_{ij}) \rangle, \quad (15)$$

which for a single component system governed by the conservative force Eq. (3) with the repulsion parameter, a , takes the form,

$$p = \rho k_B T + \frac{2\pi}{3} a \rho^2 \int_0^{R_c} r^3 \left(1 - \frac{r}{R_c} \right) g(r) dr. \quad (16)$$

Here, $g(r)$ is the radial distribution function, which in general is a function of ρ and the interaction parameter a , but for single component systems or non-segregated (well-mixed) mixtures, it has been shown [144] to be slowly varying with both ρ and a in the range $3 \leq \rho \leq 5$; $a \geq 15$, and consequently, one can define the constant parameter,

$$\alpha = \frac{2\pi}{3R_c^4} \int_0^{R_c} r^3 \left(1 - \frac{r}{R_c} \right) g(r) dr = \text{const.} \quad (17)$$

Therefore, the GW EOS is quadratic in density,

$$p = \rho k_B T + \alpha a \rho^2 \quad (18)$$

The value of the parameter α was estimated by GW as $\alpha = 0.101 \pm 0.001$. Note that, assuming $g(r)$ is unity, Eq. (17) leads to the mean-field value $\alpha = \frac{\pi}{30} = 0.105$ ($R_c = 1$ is assumed as unit of DPD length). The quadratic second term in Eq. (18) represents the excess of pressure due to interaction between the beads and the quadratic prefactor, αa , corresponds to the *second virial coefficient*. However, as shown by GW, for small densities, $\rho < 2$, the ratio of the excess pressure, $p - \rho k_B T$, to the density squared deviates considerably from the second virial coefficient (Fig. 2). Maiti and McGrother [144] also showed that when $\rho < 3$, the value of α deviates substantially from 0.1.

4.1.2. Intracomponent repulsion parameter

The intracomponent repulsion parameter for a single component system is obtained from matching the compressibility. The EOS Eq. (18), can be used to estimate the dimensionless compressibility as

$$\kappa^{-1} = \frac{1}{nk_B T \kappa_T} = \frac{1}{k_B T} \left(\frac{\partial p}{\partial n} \right)_T = 1 + \frac{0.2a\rho}{k_B T} \quad (19)$$

where n is the number density of the component and κ_T is the isothermal compressibility of the system, also given by Eq. (19). κ^{-1} calculated from the experimental value of κ_T , which for water is 4.58×10^{-10} Pa, gives $\kappa_{exp}^{-1} \sim 16$ at 298 K and using this in the GW Eq. (19) gives $a_{WW} = 25 k_B T$ when $\rho = 3$. Alternatively, once can calculate κ_{sim}^{-1} from the simulations by calculating $(\partial p / \partial \rho)_T$ in the simulations [42]. Note that in Eq. (19), it is assumed that the mapping number, the number of water

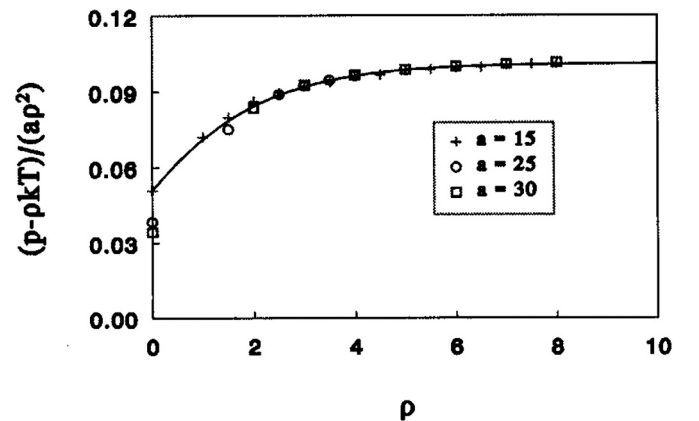


Fig. 2. Excess pressure/ $(a\rho^2)$ of a simple DPD system deviates from $\alpha = 0.1$ at low densities. Reprinted from Groot and Warren, ref. [4] with permission of AIP Publishing.

Table 1

Water intracomponent parameters at different coarse-graining levels (Reprinted from supporting information of ref. [42]).

N_w	R_c (nm)	$a_{WW}(\text{sim}), k_B T/R_c$	$a_{WW}(\text{GW}), k_B T/R_c$
1	0.45	23.4	25.0
2	0.56	51.0	51.7
3	0.65	78.5	78.3
4	0.71	106.1	104.9
5	0.77	133.7	131.6
6	0.81	161.2	158.3

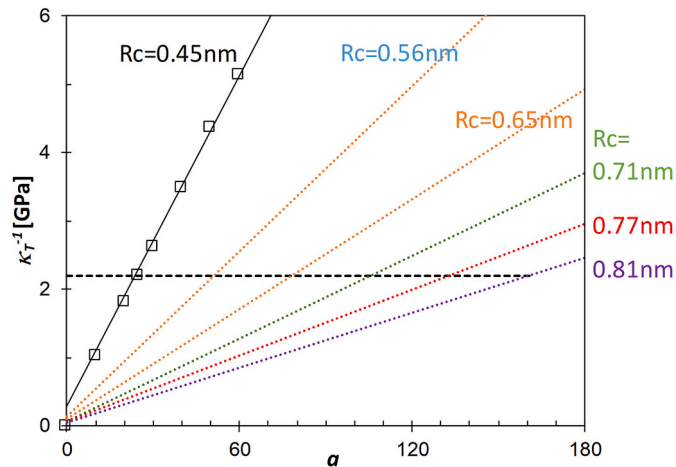


Fig. 3. The reference correlations between the inverse compressibility κ_T^{-1} with the repulsion parameter at different coarse-graining level indicated by the R_c values (Table 1). The horizontal line corresponds to the experimental compressibility of water and its intersection with various lines corresponds to the value of that matches compressibility. (Adapted from the supporting information of ref. [42]). (For interpretation of the references to color in this figure legend, the reader is referred to the web version of this article.)

molecules per bead, $N_m = 1$. However, in general, for any value of N_m , the relation in Eq. (19) results in $\kappa_{sim}^{-1}(a) = \kappa_{exp}^{-1} N_m$, in order to match the compressibility, as $n = \rho/N_m v_w$, v_w being the molecular volume of a water molecule. Thus, for $N_m > 1$, the repulsion parameter a needs to be scaled by N_m [41–42]. This scaling is linear until high values of $N_m > 6$ as depicted in Table 1, which presents the values of the repulsion parameter a_{WW} that matches κ_{sim}^{-1} obtained from simulations and the a_{WW} values that is obtained by GW prescription in Eq. (19), at various coarse-graining levels N_m . It also depicts the corresponding values of $R_c = (\rho N_m v_w)^{1/3}$. Fig. 3 shows reference correlations between the inverse isothermal compressibility κ_T^{-1} with repulsion parameter a at difference coarse-graining levels represented by the R_c values. The experimental value of $\kappa_T^{-1} = 2.18$ GPa, is represented by the horizontal line, intersections of which at various coarse-graining levels gives the desired a value that matches the compressibility.

The linear scaling of the repulsion parameter a results in the increased repulsion between DPD beads at large N_m with the conservative potential becoming steeper and steeper, and the DPD beads starting to behave like hard spheres. This effect causes solvent freezing beyond an upper coarse-graining limit, N_m^{limit} through a Kirkwood-Alder transition [178]. Dzwil and Yuen [179] estimated that this upper limit is in fact very low, $N_m^{limit} < 10$, which is very disappointing, since it makes DPD formulation unsuitable for large coarse-grained scales. Additionally, Trofimov et al. [92] pointed out that, in DPD, both compressibility and pressure cannot be matched simultaneously with the real systems, and for this reason, the parametrization schemes [22,24] that were formulated later disregard compressibility matching and focus on matching other parameters such as density and pressure.

The problem of DPD scaling was further analyzed by Fuchslin et al.

[180], who claimed that the scale invariance of the DPD equations can be achieved by scaling not just repulsion parameter, but also other parameters such as the interaction range and the length unit R_c , the DPD time unit τ and friction coefficient γ . The compressibility decreases in DPD system as the mapping number increases because, the density decreases (as the total number of DPD particles decreases due to larger coarse-graining) but at the same time, the interaction range remains the same. This causes reduction in compressibility, which then needs to be compensated by increase in repulsion parameter. Fuchslin et al. [180] suggested that the interaction cutoff should increase with the coarse-graining level, showing that the scalings $a, \gamma \sim N_m^{2/3}$ and $\tau, R_c \sim N_m^{1/3}$ would keep the DPD equations scale invariant (in 3-dimensions).

4.1.3. Intercomponent parameters

To model and simulate multicomponent systems such as binary liquid mixtures, GW used mapping with Flory-Huggins (F-H) solution theory identifying DPD as the continuum version of the Flory-Huggins lattice model. In F-H theory, the Flory-Huggins parameter χ gives the segmental energy of mixing of the polymer. For a two-component system A and B, correspondence with F-H theory led to restrictions such as equal bead sizes and constant overall density. Additionally, GW took all the intracomponent repulsion parameters to be equal, $a_{AA} = a_{BB}$. The EOS in this case was not provided by GW but subsequently by Travis et al. [23] and Maiti and McGrother [144]

$$p = \rho k_B T + \rho^2 [a_{AA} \alpha_{AA} x^2 + 2(1-x)x a_{AB} \alpha_{AB} + (1-x)^2 a_{BB} \alpha_{BB}] \quad (20)$$

where $x = N_A/N$ is the fraction of the component A, and α_{ij} , are defined in terms of the respective radial distribution functions,

$$\alpha_{ij} = \frac{2\pi}{3R_c^4} \int_0^{R_c} r^3 \left(1 - \frac{r}{R_c}\right) g_{ij}(r) dr \quad (21)$$

α_{ii} , as before can be taken to be equal and constant over the range $\rho > 3$. While α_{AB} could be different from α_{AA} and α_{BB} , they can still be assumed constant in the range $\rho > 3$, since as long as g_{AB} is slowly varying with ρ and a , any deviation in the value of α_{AB} can be absorbed to a_{AB} [23]. Assuming $\alpha_{ij} \sim \alpha$, and $a_{AA} = a_{BB} = a$, and mapping with Flory-Huggins free energy of mixing, one gets [4,144]

$$\chi_{AB} = \frac{2\alpha(a_{AB} - a)\rho}{k_B T}. \quad (22)$$

In this way, the intercomponent parameter a_{AB} can be obtained from the F-H parameter χ_{AB} , since the intracomponent parameter a is known from matching the compressibility. Note that χ_{AB} may be calculated with $\alpha = 0.1$, only when $g_{AB}(r)$ isotropic, that is below the segregation point, $\chi < \chi^{critical} = 2$. Above $\chi^{critical}$, g_{AB} is anisotropic being nonzero only at the interface between the segregated phase, and consequently, the correlation between χ and a_{AB} can be significantly different from Eq. (22). GW performed simulations and showed that the linear relation between χ and the mismatch parameter, $\Delta a_{AB} = a_{AB} - a$, holds,

$$\chi_{AB} = (0.286 \pm 0.002) \Delta a_{AB} (\rho = 3); \chi_{AB} = (0.689 \pm 0.002) \Delta a_{AB} (\rho = 5)$$

This relationship was further analyzed with Gibbs Ensemble Monte Carlo (GEMC) simulations by Wijmans et al. [181] who combined a mean field approach with GEMC simulation to show a similar behavior.

Maiti and McGrother [144] noted that χ_{AB} , can be calculated from solubility parameters (δ), that scales with the bead size; $\chi_{AB} = \frac{V_{bead}}{k_B T} (\delta_A - \delta_B)^2$, where V_{bead} volume of the bead. There is an advantage in using δ , as it can be calculated from the cohesive energy E_{coh} , which is the energy difference of the system between condensed phase and the gas phase, that may be obtained from atomistic or ab-initio simulations; $\delta = \sqrt{\frac{E_{coh}}{V_{system}}}$. With this approach, the surface tension of various liquid-liquid interfaces involving water was fairly reproduced. Travis et al. [23] mapped DPD with the regular solution theory (RST), defining a_{AB} in terms of Hildebrand solubility parameters instead of χ ,

$$(\delta_A - \delta_B)^2 = -\alpha [\rho_A^2 a_{AA} - 2\rho_A \rho_B a_{AB} + \rho_B^2 a_{BB}] \quad (23)$$

which gives a_{AB} when a_{AA} and a_{BB} are known from a compressibility matching, assuming $\alpha = 0.1$. Alternatively, the authors proposed that a_{ii} can be calculated directly from δ_i^2 , from thermodynamic considerations, taking the cohesive energy density as internal pressure (Eq. (20) without the kinetic term) for one-component systems.

4.2. Parameterization by matching infinite dilution activity coefficients

Vishnyakov et al. [42] introduced a parameterization approach that utilizes infinite dilution activity coefficients (IDAC) to determine the intercomponent repulsion parameters. A systematic parametrization scheme was developed that involves several steps: (1) Choosing the coarse-graining level and the subsequent dissection of molecules according to the CG level into near-equal volume fragments, (2) determination of the intracomponent repulsion parameter a_{ii} , by matching the compressibility of the solvent with a chosen DPD density, (3) parametrization of the bond and angle potentials between the beads within molecules by fitting with conformations in atomistic MD simulations, and (4) determination of intercomponent parameters by matching the infinite dilution activity coefficient in binary solutions of reference compounds to the results of MC simulations of respective DPD fluids.

Fig. 4 describes the coarse-graining procedure suggested in ref [42] in the case of surfactants of the type C_nE_m , where C represents an alkyl CH_2/CH_3 group while E represents the ethylene oxide ($-CH_2-O-CH_2-$) groups. The atoms are grouped into CG beads of equal volumes according to $V_{(CH_2)_2} = V_{CH_2-O-CH_2} = V_{2H_2O}$ and CG levels corresponding to the mapping number $N_m = 3 - 6$ were analyzed. The CG representation of the surfactants consists of two bead types, the hydrophobic tail beads (T) consist of several Cs and the hydrophilic head (H) group beads composed of several Es. To calculate the bead volumes, one can use group-contribution methods like ASOG and UNIFAC [182] or estimate by ab initio calculations, for example, using the COSMO [183] software. The intracomponent parameter, taken equal for all components, is determined by the GW prescription of matching the isothermal compressibility of water. To properly account for coarse-graining, the compressibility obtained from simulations needs to be scaled by the mapping number N_m , which results in scaling the a_{ii} by the same factor.

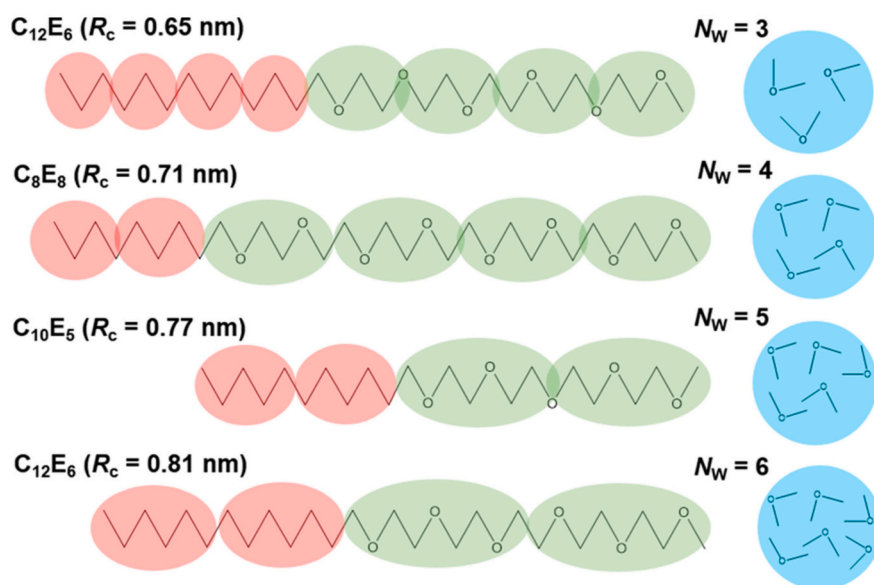


Fig. 4. Coarse-graining of C_nE_m surfactants at different CG levels defined by the number of water molecules N_M in a CG water bead (Adapted with permission from Lee et al. ref. [42], Copyright 2016, American Chemical Society). (For interpretation of the references to color in this figure legend, the reader is referred to the web version of this article.)

To calculate repulsion parameters a_{ij} between dissimilar beads, the authors suggested to choose the appropriate reference compounds comprised of the bead types in the coarse-grained system that are liquids at ambient conditions. For instance, in the case of C_nE_m surfactant, linear alkanes such as hexane are chosen to be reference compounds for the T beads. To parametrize the head group beads, although ether molecules such as $CH_3OCH_2CH_2OCH_3$ appear to be appropriate, due to shortage of activity data on such compounds, short PEO oligomers with molecular weight of 400 Da were taken as reference compounds, as the data on water activity in PEO–water solutions has been reported for a wide range of concentrations [184]. To calculate IDAC, the insertion energies E_{ij}^{ins} of the reference solute bead i in a system of reference compound of bead type j are calculated as a function of the mismatch parameter $\Delta a_{ij} = a_{ij} - a_{ii}$, by performing Widom insertion, as depicted in Fig. 5a-b. This is performed for monomer or dimer beads. The experimental IDAC γ_{ij}^∞ obey the relation [42],

$$\ln \gamma_{ij}^\infty + \ln \left(\frac{b_j \rho_i}{b_i \rho_j} \right) = \ln \langle e^{-E_{ij}^{ins}/k_B T} \rangle - \ln \langle e^{-E_{jj}^{ins}/k_B T} \rangle \quad (24)$$

b_i , b_j are the mapping number of the respective beads, that is the number of molecules represented by the beads. E_{ij}^{ins} is the Widom insertion energy of molecule i into a bath of j molecules, calculated from MC simulations at constant pressure. ρ_i and ρ_j are densities of i and j molecules in the simulations, keeping constant pressure. They are different for monomer and dimer molecules, since the DPD pressure is lower for dimer. E^{ins} is calculated as a function of the mismatch parameter Δa_{ij} , and the activity coefficients predicted by Eq. (24) is matched with experimental value of IDAC. In this way, a_{ij} are obtained by a calibration relationship between γ_{ij}^∞ and Δa_{ij} (Fig. 5c).

4.3. Bond parameters

The bond interaction potentials are responsible for the flexibility and conformations of chain molecules modelled as connected beads. No top-down procedure exists to introduce and parameterize the inter-bead bond potentials in DPD. The bond interaction potentials employed in in DPD are of the same type as generally used in atomistic MD simulations. For the harmonic bond potential, the bond force is given by,

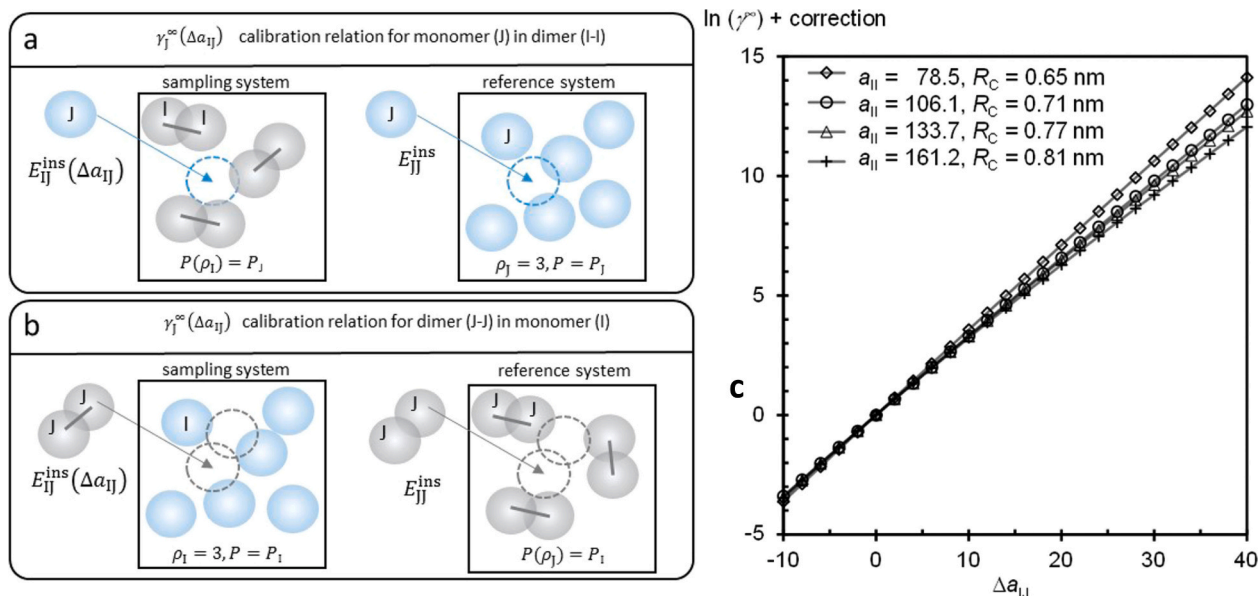


Fig. 5. Depiction of the Widom insertion method to calculate the (a) monomer and (b) dimer insertion energies of bead type j in the systems with bead types i and j . (c) The scaling of activity coefficient with mismatch parameter Δa_{ij} . (Adapted with permission from Lee et al. ref. [42], Copyright 2016, American Chemical Society.) (For interpretation of the references to color in this figure legend, the reader is referred to the web version of this article.)

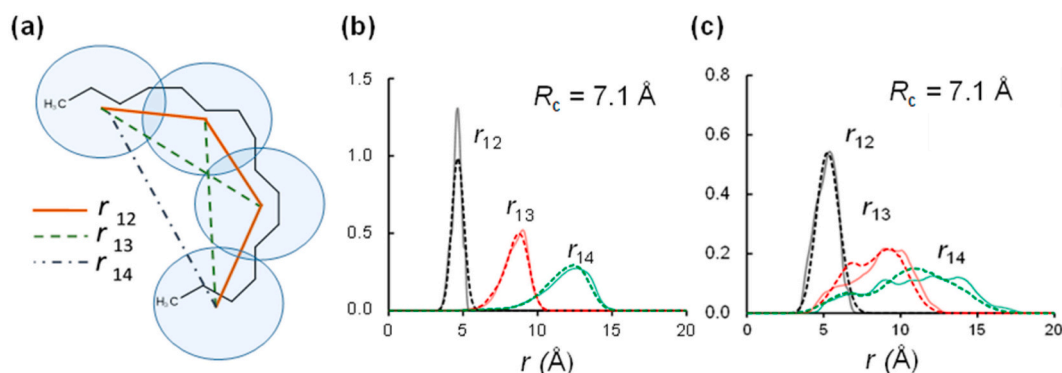


Fig. 6. (a) Nearest (r_{12}), second nearest (r_{13}) and third nearest r_{14} neighbor distances in a polymer chain. (b) Distributions of r_{12} , r_{13} and r_{14} for n-alkanes in atomistic MD (solid) simulations and DPD (dashed) simulations at the CG level corresponding to $R_C = 0.71 \text{ nm}$. (c) Distributions of the same for PEO. (Adapted with permission from Lee et al. ref. [42], Copyright 2016, American Chemical Society.) (For interpretation of the references to color in this figure legend, the reader is referred to the web version of this article.)

$$\mathbf{F}_{ij}^B(r_{ij}) = -K_B(r_{ij} - r_0)\hat{\mathbf{r}}_{ij}. \quad (25)$$

In the case of the finite extensible nonlinear elastic (FENE) bonds,

$$\mathbf{F}_{ij}^B(r_{ij}) = -\frac{K_B(r_{ij} - r_0)}{1 - \frac{(r_{ij} - r_0)^2}{r_M^2}}\hat{\mathbf{r}}_{ij}; 0 \leq r_{ij} \leq r_M. \quad (26)$$

Here, K_B is the force constant, r_0 is the equilibrium bond length, and r_M is the divergence length. These parameters are calculated using a bottom-up approach, by matching the radial distributions functions with the results of atomistic MD simulations. Since the CG beads represents certain atom groups, a bond that is defined between the center of mass of two atom groups is good definition of a CG bond. In modelling chain molecules, like C_nE_m surfactants, additional second nearest-neighbor (1–3) bonds can be introduced in order to account for the chain rigidity [42]. To estimate the bond parameters, K_B and r_0 , radial distribution functions of the center of mass distances of the first (r_{12}), second (r_{13}) and third (r_{14}) nearest neighbor beads (see Fig. 6a) obtained from CG simulations are matched with the distributions of the corresponding atomic groups in an atomistic simulation. Fig. 6b-c shows matched bond

distributions for n-alkanes (Fig. 6b) and polyethylene oxide (PEO) (Fig. 6c). It was shown that the chain rigidity significantly affects morphology of surfactant solution, in particular the critical micelle concentration (CMC) [159].

However, bonding introduces certain errors in DPD simulations. One effect is that the bonding increases the local density when the bond length is small, as the bonded beads gets closer than the free beads in the bulk. Another effect is that the bonded solute repels the solvent beads more strongly than the monomer solute, because of the proximity of the neighboring beads. Such effects were considered recently by Saathoff [24], adopting parameterization based on matching the infinite dilution activity coefficients [42].

4.4. DPD parameterization with different bead volumes

The restriction of equal bead volumes and equal intracomponent repulsion parameters in the GW DPD formulation is a result of direct mapping onto F-H theory. This restriction does not allow for a proper parameterization of the chemical differences between the components and the local density variations. In particular, it implies equal

compressibility and density of coexisting phases that is rarely the case. Backer et al. [185] performed DPD simulations containing beads at two coarse-graining levels, with the larger CG beads representing the more coarser bulk solvent system. The parameters of different-sized beads were obtained keeping the mass density constant and particles were distributed in three different regions: one region containing only smaller CG particles, other region consisting of only larger ones while an overlapping region containing both smaller and larger particles. Essentially the same approach was used later by Spaeth et al. [186] to model polymer chains of different bead sizes.

A general parametrization approach to allow different sizes of beads in a multicomponent DPD system was suggested by Kacar et al. [44], who defined 'pure' phase densities of the components with respect to a reference system, for example, water. The reference system is assumed to obey the GW EOS, with a reference interaction cutoff R_{DPD} which need not be effective diameter for all bead types,

$$p = \rho k_{BT} + \alpha \rho^2 R_{DPD}^3 \quad (27)$$

where the reference density $\rho R_{DPD}^3 = 3$ is a common choice. The pure phase density of component i , ρ_i , *pure*, is in general different from ρ , but the pure system obeys the GW scheme,

$$p_i = \rho_{i,pure} k_{BT} + \alpha a_{ii} \rho_{i,pure}^2 R_{DPD}^3 \quad (28)$$

The self-repulsion parameters, a_{ii} are calculated by solving Eq. (28), requiring that pure phase systems attain the reference pressure p ,

$$a_{ii} = \frac{p - \rho_{i,pure} k_{BT}}{\alpha \rho_{i,pure}^2 R_{DPD}^3} \quad (29)$$

Hence, $a_{ii} \neq a_{jj}$, as long as the pure phase densities of the components i and j are different. This allows for the phase separation of components, which differ by density and compressibility. The intercomponent parameters are found using F—H theory mapping by defining a neutral repulsion parameter, which for a two-component system is defined using the combining rule, as $\hat{a}_{ij} = \sqrt{a_{ii} a_{jj}}$. With this definition the intercomponent parameters are given in terms of the Flory-Huggins parameter χ_{ij} .

$$\Delta a_{ij} = \frac{p}{0.0454 (a_{ii} \rho_{i,pure} + a_{jj} \rho_{j,pure})} \chi_{ij} k_{BT} \quad (30)$$

where $\Delta a_{ij} = a_{ij} - \hat{a}_{ij}$.

The reference pressure p is chosen to secure either the overall compressibility or the compressibility of a key component. As such, it is not the compressibility, but the density of the components that is the basis for the parametrization. The authors developed this method in order to simulate polymeric systems with proper local densities, for the reverse-mapping into the corresponding atomistic systems. In such a multi-scale approach, DPD can be employed to equilibrate a large length-scale system for long time-scales, which can be reverse-mapped into its atomistic version. The authors applied this multiscale approach to study cross-linked polymers [187], and structural and elastic properties of wet and dry polyethylene glycol [188]. Other studies include drug encapsulation by Pluronic [189] and poloxamer micelles [190].

4.5. Extensions of GW EOS

In addition to the undesirable feature that the bead sizes are equal, another issue with GW formalism is that the EOS deviates significantly in the low-density regime from the second virial coefficient for densities, $\rho < 2$ (Fig. 2). To address this limitation of the GW formulation, Liyana-Arachchi et al. [145] considered liquid-liquid equilibrium and suggested a revised GW formulation, based on the formalism suggested by Kacar et al. [44] to include different bead volumes. The revised GW EOS (rGW EOS) has the form,

$$p_{rGW}(\rho, T) = \rho k_{BT} + \rho^2 [f_{B2}(\rho) B_2(a_{ii}) + f_a(\rho) a_{ii}], \quad (31)$$

where $f_{B2}(\rho)$ and $f_a(\rho)$ are two density-dependent switching functions and $B_2(a_{ii})$ is the second virial coefficient, which is a function of the repulsion parameter a_{ii} . Eq. (31) corrects GW EOS at low density, the ratio of the excess pressure to the density approaches B_2 in the low-density limit. B_2 is given by the Mayers function,

$$B_2(a_{ii}) = -2\pi \int_0^{R_c} \left(e^{-\frac{u(a_{ii}, r)}{k_{BT}}} - 1 \right) r^2 dr, \quad (32)$$

and can be fitted to a polynomial function of a_{ii} . The authors found empirically the switching functions fulfilled the following relations,

$$f_{B2}(\rho) = \frac{1}{1 + \rho^3}; f_a(\rho) = \frac{c_1 \rho^2}{1 + c_2 \rho^2} \quad (33)$$

Where the constants, $c_1 = 0.0802$ and $c_2 = 0.7787$, were found by fitting with simulation data. The resulting rGW EOS for a single component system is given by

$$p_{rGW}(\rho, T) = \rho k_{BT} + \left[\frac{B_2(a_{ii})}{1 + \rho^3} + \frac{c_1 \rho^2}{1 + c_2 \rho^2} a_{ii} \right] \rho^2. \quad (34)$$

For large densities, ρ , as $f_{B2}(\rho)$ decays rapidly and pre-factor of the quadratic term in the Eq. (34) approaches $\frac{c_1}{c_2} a_{ii} = 0.103 a_{ii} \sim \alpha a_{ii}$, the rGW EOS becomes close to the GW EOS. The value of c_1/c_2 in this case is closer to the mean field value of $\frac{\rho}{30} = 0.1047$. Comparison of GW and rGW EOSs in simulations with different ρ and a_{ii} showed that rGW EOS is significantly more accurate, as the mean unsigned percentage errors (MUPE) are 11.5% and 0.7% respectively over a large fraction of (a_{ii}, ρ) space.

The intercomponent parameters are calculated for athermal ($\chi = 0$) and thermal ($\chi \neq 0$) liquid mixtures. For athermal mixtures, the intercomponent parameter, a_{ij} , is calculated analogously to the approach of Travis et al. [23], assuming that the difference in solubility parameters vanishes (see Eq. (23)),

$$a_{ij}^{ath} = \frac{h(a_{ii}, \rho_{i,pure}) a_{ii} \rho_{i,pure}^2 + h(a_{jj}, \rho_{j,pure}) a_{jj} \rho_{j,pure}^2}{2 \rho_{i,pure} \rho_{j,pure} \sqrt{h(a_{ii}, \rho_{i,pure}) h(a_{jj}, \rho_{j,pure})}} \quad (35)$$

Here, $h(a, \rho) = f_a(\rho) + \frac{B_2(a) f_{B2}(\rho)}{a}$ is the factor in rGW EOS that corresponds to the quadratic prefactor αa in GW EOS. For thermal mixtures, the Flory-Huggins parameters are expressed in terms of infinite dilution chemical potentials, which are then solved iteratively to obtain a general fitting equation for a_{ij}^{th} ,

$$a_{ij}^{th} = a_{ij}^{ath} + \frac{30.17 \chi}{\rho_{i,pure} \rho_{j,pure}} + \frac{561.6 \chi^{1.667}}{(\rho_{i,pure} \rho_{j,pure})^{2.864}}. \quad (36)$$

The authors employed this method for modelling liquid-liquid equilibrium of binary mixtures, which led to satisfactory prediction of liquid-liquid coexistence curves [145]. Tang et al. [191] used the rGW EOS formalism to study the effects of salt and perfume raw materials on the rheology of surfactant body-wash micellar solutions.

Minkara and coworkers [25] further extended the rGW EOS to homogeneous polymeric systems. In general, an equation of state for a polymer system differs from the corresponding monomer fluids due to contribution from bonding and chain connectivity. The bonding effects are introduced in DPD analogous to the EOS for Lenard-Jones chains [192] utilizing the first order thermodynamic perturbation theory (TPT1), in which the pressure is given by,

$$p = p_R + \frac{1 - n_p}{n_p} \rho_R k_{BT} \left[1 + \rho_R \frac{\partial \ln y_R(l_b)}{\partial \rho_R} \right] \quad (37)$$

p_R , ρ_R and $y_R(l_b)$ are the pressure, density and the cavity correlation function of the reference monomeric system. n_p is the number of monomers in the chain and l_b is the bond length. If the DPD systems consists of the monomeric beads, the value of p_R is given by the GW or rGW EOS. Using the rGW EOS Eq. (34) in Eq. (37) gives the chain-revised GW EOS (crGW EOS) for the polymeric system, which is given by,

$$\frac{p}{k_B T} = \rho_{chain} + f_{B2}(\rho_{chain}) B_2(a_{ii}, n_p, l_b) \rho_{chain}^2 + f_a(n_p, \rho_{chain}) (n_p \rho_{chain})^2 \left[a_{ii} - \frac{\eta(n_p - 1)}{n_p + \beta} \frac{\partial \ln y_R(l_b)}{\partial (n_p \rho_{chain})} \right] \quad (38)$$

Here, η and β are additionally introduced parameters in order to smoothly fit to the $n_p \rightarrow 1$ limit. The parameterization of a_{ij} in both athermal and thermal mixtures follows the rGW scheme.

The crGW EOS is an improvement over the rGW EOS for the case of homo-oligomeric systems accounting for the bonding effects such as a reduction in pressure due to linking of beads. It predicts the pressure, second virial coefficient, and upper critical solution temperature for chain molecules significantly more accurately than both the rGW EOS and GW EOS, especially when the bond lengths are small.

4.6. Parameterization by matching water-octanol partition coefficients

Recently, Anderson et al. [22] presented a systematic parameterization scheme for DPD, based on matching experimental densities and water-octanol partition coefficients. This is another alternative methodology to the GW approach that allows for using different sizes of beads. The level of coarse-graining is defined by the water mapping number N_w and the number density set to $\rho = 3, 5$, etc. The authors demonstrated this coarse-graining procedure by deriving parameters for a number of compounds that involve alkanes, alcohols, ether, amines and aryl liquids, employing a 1–3 heavy atom mapping with $N_w = 2$. Multi-bead molecules are connected by harmonic bonds, and rigidity of the structure is induced by imposing angle-dependent potentials.

As in the parametrization scheme by Kacar et al. [44], water is taken as the reference compound, and the interaction length R_c of water is assumed to be unit of DPD length. The intracomponent repulsion parameter for water a_{WW} is taken to be $25 k_B T$, irrespective of the coarse-graining level. The intercomponent interaction cutoff lengths, R_{ij} , are determined by the simple mixing rule $R_{ij} = 1/2(R_{ii} + R_{jj})$, where the self-repulsion cutoffs R_{ii} are calculated from the molar volumes of the fragments represented by the respective bead types. The self-repulsion parameters, a_{ii} , are calculated by matching the experimental pure component densities. The intercomponent repulsion parameters are determined by a two-step procedure. First, the initial guess is made using the combining rule, $a_{ij} = 1/2(a_{ii} + a_{jj})$, and then, the parameters are refined by matching the water-octanol partition coefficients (P_{OW}) of several reference compounds consisting of the bead types,

$$\log_{10} P_{OW} = \log_{10} \frac{[S]_O}{[S]_W} \quad (39)$$

where $[S]_{O/W}$ represents the molar concentration of the solute in the octanol/water phase. The authors validated their approach by simulating aggregation of alkyl ethoxylate and alkyl sulfate [193] surfactants in water reproducing critical micelle concentration (CMC) in good agreement with the experiments. This was also used for studies of the phase behavior of sodium lauryl ethoxy sulfate [194] in aqueous solutions.

4.7. Electrostatic interactions in DPD

4.7.1. Groot model

The soft conservative DPD potential represents an effective van der Waals type interactions between the beads, it does not include the electrostatic interaction. To incorporate electrostatic interaction in DPD was a challenge since the usual Coulomb interaction diverges at $r = 0$,

which when applied between soft beads leads to unphysical ion pairing between the oppositely charged beads. It is necessary to ‘soften’ the electrostatic interaction as well. Inclusion of electrostatic interaction is essential in several physical systems, such as polyelectrolytes, ions, ionic surfactants and bio-membranes containing charged lipids. Groot [45] first introduced electrostatic interactions in DPD, with a field-theoretical solution for the Poisson equation for the electrostatic field, while the divergence of the field at $r = 0$, is avoided by using a smearing charge density

$$\frac{\rho_e(r)}{Q} = \frac{3}{\pi R_e^3} \left(1 - \frac{r}{R_e} \right); r < R_e \quad (40)$$

which is zero for $r > R_e$, Q is the charge on the bead and R_e is the smearing radius. When the Poisson equation is solved for this charge density, it leads to an electrostatic potential that is finite at $r = 0$, with value $U(r = 0) = 1.64/R_e$ for $N_m = 3$. Groot followed the numerical method of Beckers et al. [195] to solve the electrostatic field on a lattice that is referred to as the particle-particle-particle-Mesh (PPPM).

4.7.2. Ewald summation and Slater type charges

Later, Melchor et al. [196] introduced Ewald summation into DPD. The Coulomb interaction between charge species in a cubic periodic cell of side length L is given by total potential

$$U = \frac{1}{4\pi\epsilon_0\epsilon_r} \sum_i \sum_j \sum_n' \frac{Q_i Q_j}{|\mathbf{r}_{ij} + \mathbf{n} L|} \quad (41)$$

The summation over $\mathbf{n} = (n_x, n_y, n_z)$ which form a simple cubic lattice, accounts for the long-range contribution from periodic cells, $\mathbf{n} = 0$ corresponding to the original system for which $i = j$ terms are excluded - indicated by the prime. Q_i are the charges, and ϵ_0, ϵ_r are respectively the permittivity of vacuum and dielectric constant of the medium. When the charge densities are used, the summand in Eq. (41) is replaced by an integral.

To perform Ewald summation, the charge density at a point \mathbf{r} due to the presence of a point charge Q_i placed at \mathbf{r}_i is split into short-range and long-range contributions by adding and subtracting a Gaussian charge distribution $Q_i G_\nu$ with

$$G_\nu(r) = \frac{1}{(2\pi\nu^2)^{3/2}} \exp\left(-\frac{r^2}{2\nu^2}\right) \quad (42)$$

The splitting of the charge densities in the Ewald method leads to faster convergence of the short-range term of the electrostatic potential, while the long range contribution can be easily evaluated in the reciprocal space. For point charges, $\rho_e^i(\mathbf{r} - \mathbf{r}_i) = Q_i \delta(\mathbf{r} - \mathbf{r}_i)$, but in DPD some other finite distributions have to be used to avoid the unphysical ion-pairing.

Gonzalez-Melchor et al. [196] chose Slater-type charge densities instead of the linear ones suggested by Groot,

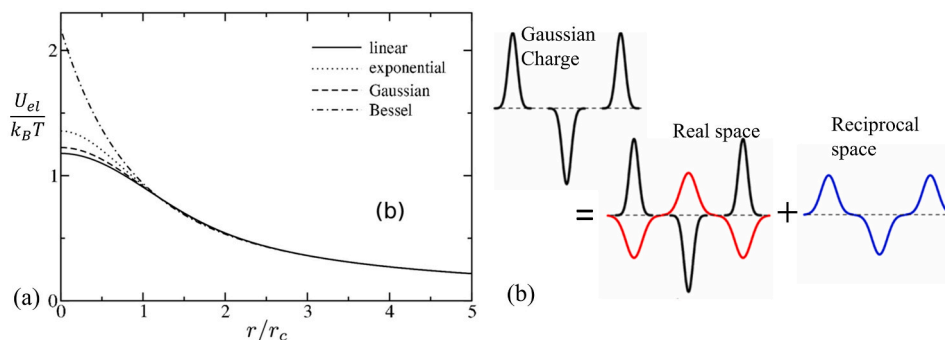


Fig. 7. (a) Comparison of the electrostatic interaction potentials of four charge models. (Adapted with permission from Warren and Vaslov, ref. [82]. @ AIP Publishing). (b) Depiction of Ewald summation of Gaussian charges (Adapted with permission from Eslami et al., ref. [49], Copyright 2019, American Chemical Society). (For interpretation of the references to color in this figure legend, the reader is referred to the web version of this article.)

$$\frac{\rho_e(r)}{Q} = \frac{1}{\pi\lambda^3} e^{-\frac{r}{\lambda}} \quad (43)$$

where λ is the decay length. Using this charge density Melchor et al. [196] showed that the pair-wise electrostatic force between two charged beads is,

$$F_{ij}^E(r_{ij}) = \frac{k_B T R_c \Gamma}{4\pi} \frac{Q_i Q_j}{r_{ij}^2} \left\{ 1 - e^{-\frac{2r_{ij}}{\lambda}} \left[1 + 2 \frac{r_{ij}}{\lambda} \left(1 + \frac{r_{ij}}{\lambda} \right) \right] \right\} \frac{\hat{r}_{ij}}{r_{ij}} \quad (44)$$

The constant $\Gamma = e^2 / (k_B T \epsilon_0 \epsilon_r R_c)$, defined by Groot [45].

4.7.3. Gaussian and Bessel charge densities in DPD

Gaussian charges has been employed in other contexts such as polarizable water models [197], and ultra-soft primitive model (URPM) [198] for polyelectrolytes. In DPD, Warren et al. [47] first introduced the use of Gaussian [47] and Bessel [199] charge densities for softening the electrostatic potential. Warren and Vlasov (WV) [48] later compared the four charge models (linear, Slater-type exponential, Gaussian and Bessel) in DPD and Fig. 7a shows the electrostatic potential in each case. WV concluded that choice of the type of the distribution does not have any physical significance, and so it can be chosen to improve the computational efficiency. In this regard, use of Gaussian charge densities in DPD has recently received more attention. The attractive feature is that it is most convenient to use with Ewald sums, as choosing ρ_e to be Gaussian makes Eq. (42) all-Gaussian in the summation procedure. In addition, choosing ρ_e to be the same as G_j add to computational efficiency by making the short range contribution to the electrostatic energy vanish, and this was utilized by URPM models and the recent DPD simulations on surfactant micelles from Larson's group [200]. Eslami et al. [49] implemented Gaussian charges in their in-house DPD program, and showed that it is more effective to choose different Gaussians for representing charge density and performing the Ewald sums. The

Ewald summation of Gaussian charges is schematically described in Fig. 7b.

5. Applications of DPD

The prodigious effectiveness of DPD in simulating soft matter has been demonstrated in studying various phenomena in colloidal and interfacial systems. In the following, we systematically review DPD studies on various mesoscale polymeric, colloidal, interfacial and biological systems.

5.1. Polymeric systems

5.1.1. Dilute polymer solutions

DPD was recognized to be well-suited for modelling polymers, immediately after its inception. The mesoscopic scales of DPD are appropriate for bead-spring representation of polymers and the conformational relaxation dynamics. Unlike in random walk (RW) and other models, excluded volume and hydrodynamic interactions are naturally incorporated in DPD and thus it becomes possible to relate micromolecular dynamics to the macroscopic properties such as rheology. Initial works analyzed general properties of dilute solutions, effects of solvent quality, rheological properties, and scaling laws [201–205]. Schlijper, Hoogerbrugge and Manke used weak (Hookean) and strong (Fraenkel) spring models of polymers in good solvent and showed that DPD simulations fairly reproduce Rouse-Zimm model scaling exponents, for radius of gyration $R_g \sim N^\nu$ and relaxation times, $\tau_R \sim N^\alpha$ [203]. They obtained $\nu = 0.51$ and 0.52 and $\alpha = 1.93$ and 1.83 for weak and strong spring models respectively while the theoretical values being $\nu = 0.59$ and $\alpha = 2$ [206]. Different solvent conditions can be effectively incorporated by tuning the polymer solvent repulsion parameter, for instance, $a_{PS} = a(1 + \xi)$, where a is the intracomponent parameter. Changing ξ from negative to positive leads to change in

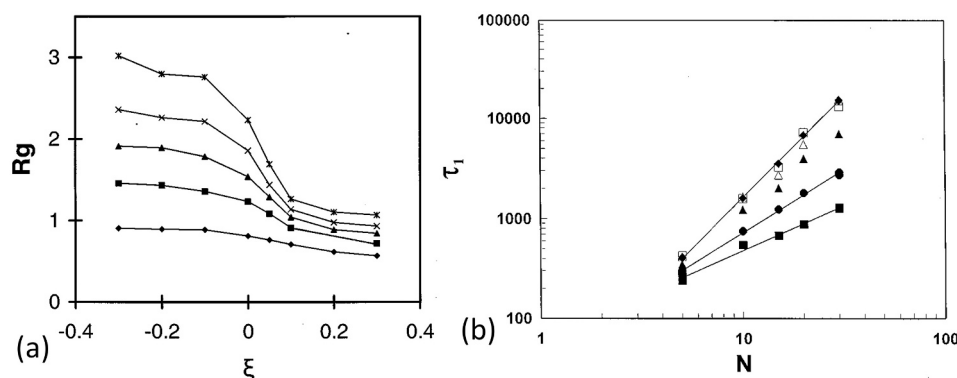


Fig. 8. (a) Variation in radius of gyration R_g in DPD simulations as the solvent quality ξ is changed from good (–ve) to poor (+ve) for different chain lengths $N = 5$ (diamonds), 10 (squares), 15 (triangles), 20 (\times) and 30 (\ast). (b) Relaxation times of conformational correlations scaling with chain lengths at different solvent qualities, $\xi = -0.3$ (diamonds), -0.2 (∇), -0.1 (Δ), 0 (O), 0.05 (dots), 0.1 (open squares) and 0.3 (dark squares). Adapted from Kong et al. (ref. [202]) with permission of AIP Publishing.

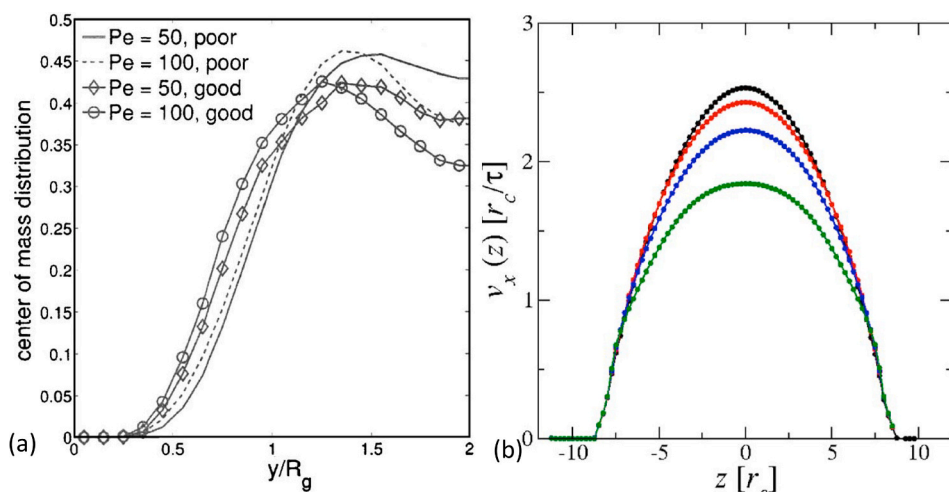


Fig. 9. (a) Center of mass distributions of polymer (chain length = 16) in a Poiseuille flow at different solvent quality and Peclet numbers (Pe). Adapted from Fedosov et al. ref. [208], with permission of AIP Publishing. (b) Velocity profiles of polymer solutions at different concentrations in a slit-like channel under pressure-driven flow. Curves correspond to polymer volume fractions 0 (black), 0.06 (red), 0.12 (blue) and 0.24 (green). Adapted from Millan et al. ref. [209], with permission of AIP Publishing. (For interpretation of the references to color in this figure legend, the reader is referred to the web version of this article.)

solvent quality from good to poor [202]. Kong et al. [202] showed using DPD simulations that the radius of gyration and the relaxation times obtained from the decay of the conformational correlation function undergo sharp first-order like transitions from extended to collapsed state, as ξ is increased (Fig. 8). The scaling exponents varied in the ranges $\nu = 0.32 - 0.61$, $\alpha = 0.9 - 2.03$ as the solvent quality is changed poor to good, in agreement with Rouse-Zimm theory.

DPD simulations showed [201] that the polymers in dilute solutions in regions of confinement between two parallel walls, exhibited dissimilar dynamical modes in parallel and perpendicular directions as the channel gap narrowed. The radius of gyration and configurational autocorrelation functions scaled differently in these modes, consistent with confined polymer systems such as polymer nanocomposites that exhibit chain mobilities enhanced in parallel but reduced in perpendicular directions of the walls [207]. Such confinement effects also occur in physical processes involving polymer flow in micro/nano channels, such as chromatographic processes that are used to separate polymers, lubrication processes that use polymer additives, and polymer transport. Several authors [102,208–209] considered flow of dilute and semi-dilute solutions of linear polymers through capillary channels. Flow of linear polymers in rectangular channel of various sizes under a pressure driven flow was studied by Willemson et al. [102], who measured axial velocity of polymers as a function of chain length/radius of gyration. In confined systems, depletion of chains that occurs near the regions close to the solid walls, has been observed experimentally, which arises due to entropic effects, the steric repulsion from the wall. Fedosov et al. [208] performed DPD simulations of polymers in slit-like channels of different widths to investigate depletion effects as functions of channel width, solvent quality, wall-polymer interactions, and polymer chain length and obtained the polymer center-of-mass distributions at different distances from the wall and the shape of the polymer from the components of local radius of gyration. Further, this study analyzed the polymer migration through channels in a Poiseuille flow, created by applying a pressure gradient as a constant force on solvent and polymer particles, showing that the depletion effects were affected by the flow and the center of mass distributions peaked at an intermediate region between the wall and the center line, (Fig. 9a) which was attributed to the hydrodynamic Segre-Silberberg effect [210].

As the polymer concentration increases in a pressure driven flow, the solution exhibits a slip at the boundary, because in a Poiseuille flow, the shear rate reduces towards the center and therefore the polymers tend to remain in the central region. Millan et al. [209] studied, using DPD simulations, the pressure driven flow of dilute and semi-dilute polymer solutions in nanoscale slit-like channels. The velocity profiles of the polymer solutions at different concentrations deviated from the

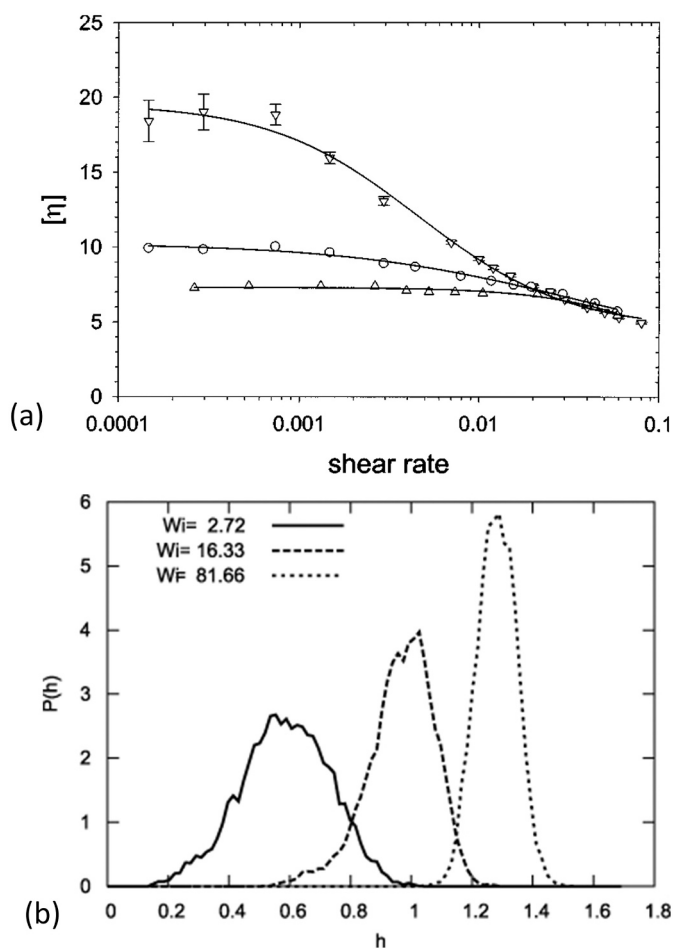


Fig. 10. Intrinsic viscosity $[\eta]$ of a 10-bead polymer solution as a function of shear rate in good (∇), near θ (\circ) and poor (Δ) solvent conditions. Reprinted from Pan and Manke, ref. [212] with permission of AIP Publishing. (b) SDDP simulations of Litvinov et al., ref. [213]: the distribution of the mean square end-to-end distance of the DNA h at different shear rates, represented as the dimensionless w_i -shear rate multiplied by the relaxation time of the polymer chain. © IOP publishing reproduced with permission. All rights reserved.

quadratic form, with the slip at the boundary increased and the velocity in the central region decreased, as polymer concentration increased (Fig. 9b). This study also showed that polymers tend to remain in the

intermediate region between the wall and the center. Millan and Laradji [211] investigated cross-stream migration of polymers in a Poiseuille flow at different Schmid numbers using a modified and generalized DPD formalism developed by Fan et al. [121] to remedy the low Schmid numbers exhibited by conventional DPD, and observed migration of the polymers away from the walls as Schmid number is increased.

Polymers exhibit viscoelastic properties, are capable of modulating viscosity with change in shear flow, and are used as lubricant additives in many occasions involving lubricated surfaces. Rheological properties of dilute polymer solutions were analyzed by Kong et al. [204] who performed DPD simulations of short linear polymers connected with Fraenkel springs and observed shear-thinning. Pan and Manke [212] showed that rheology of dilute solutions of a 10-bead chain connected with FENE springs depends on the solvent quality that was modelled in terms of the effective repulsion between solvent and the polymer beads. The intrinsic viscosity of the solutions increases as the solvent quality increases and shear thinning is more pronounced at higher solvent qualities (Fig. 10a). Simulation results can directly link the rheology to polymer configurational properties; the radius of gyration of the polymer R_g decreases as solvent quality decreases, leading to the reduction in viscosity. With a shear applied, R_g increases, and the increase in the expansion ratio that is defined as the ratio of R_g to its value at zero shear was more pronounced at poor solvent conditions. Litvinov et al. [213] used SDPD to investigate static and dynamic behavior of DNA tethered to a wall under shear flow. The simulations demonstrated that the shear flow affects the single chain dynamics, for example, mean square end-end distance increases with shear rate (Fig. 10b).

Liquid-liquid phase separation in polymer-solvent systems is another important phenomena, the de-mixing of polymer solutions is used as a cost-effective method in purifying polymers, for example, during a solution polymerization. Freeman and Rowlinson [214] observed phase separation of polymer-solvent systems at lower critical solution temperature (LCST). Van Vliet et al. [215] performed DPD simulations of polymer-solvent phase behavior and used pressure and temperature-dependent repulsion parameters to mimic LCST behavior. Dynamics of de-mixing was studied for linear and branched polymers, and it was observed that branching reduces radius of gyration and promotes de-mixing.

Qian et al. [216] examined surface diffusion of a polymer chain adsorbed on a surface. When strongly adsorbed, the polymer chain resides completely on the surface with heights normal to the surface roughly of the order of the monomer size. DPD simulations [216] were performed with smooth and rough (with sticking points or obstacles) surfaces and found that the polymer diffusion coefficient obeys Rouse scaling $D \sim N^{-1}$ in the case of smooth surfaces, while it exhibits reptation-like behavior $D \sim N^{-3/2}$ for rough inhomogeneous surfaces,

which comply with experiments on surface dynamics of polymers.

Yang et al. [217] performed DPD simulations to analyze forced polymer translocation through a nanopore across a membrane. In this study, the polymer was initially placed on the *cis* side (Fig. 11a) of a cylindrical cell, with one of its ends inside the pore. The polymer was subject to uniform electrostatic or hydrostatic force that drives it towards the *trans* side, and the simulations analyzed the dependence of translocation time τ on various factors, such as chain length, solvent quality that is controlled by the polymer-solvent repulsion parameter a_{ps} , (Fig. 11b-c) and the driving force, E . In general, for coil-like polymers, in good solvent conditions, the scaling correlations $\tau \sim E^{-\xi}$ and $\tau \sim N^\beta$ were found to hold, while such correlations could not be established for globular chains.

Groot [218] considered polymer-surfactant complexes using DPD simulations. The morphologies of the polymer-surfactant complexes depend on the details of the interaction between the two molecules, for example, a hydrophobic polymer induced *bottle-brush* conformations, in which surfactant tails are adsorbed on to the polymer, while a hydrophilic polymer interact favorably with surfactant head groups, leading to *necklace* morphologies of surfactant micelles adsorbed on the polymer. Rahatekar et al. [219] analyzed percolation in solutions of rigid rod-like nano fibers under electric field. The critical concentration for the electric field-induced percolation in such systems depends on the aspect ratio (length to diameter) and the orientation of the fibers.

5.1.2. Concentrated polymer solutions and melts

In concentrated polymer solutions or polymer melts, entanglements are crucial as they determine the dynamical behavior of the chains, the topological constraints imposed by the presence of other chains cause the chains to reptate (like a snake), which is described in the reptation theory [206]. However, in standard DPD, the soft nature of the interaction potentials, allow unphysical chain crossing or topological violations across the monomer bonds and as a result, entanglements are not properly captured. This leads to unphysical rheology and dynamics as in earlier DPD studies [205], which showed that the DPD polymer melt obeys $D \sim N^{-1}$, for the diffusion coefficient and $\eta \sim N$ for the viscosity, while the actual exponents being -2 and 3.4 respectively, predicted by reptation theory and experiments. In this scenario, DPD reproduces only the Rouse (phantom chain) limit and not the reptation behavior.

To incorporate uncrossability constraint in the simulations and prevent chain crossing, several methods have been suggested in the literature. Nikunen et al. [220] noted that the chain crossing can be prevented by proper choice of bond parameters and coarse-graining level; if the maximum bond stretches are less than the impenetrable size (region exclusive to other beads) of the polymer beads, then bond crossing will not occur. The impenetrable core size of the CG beads

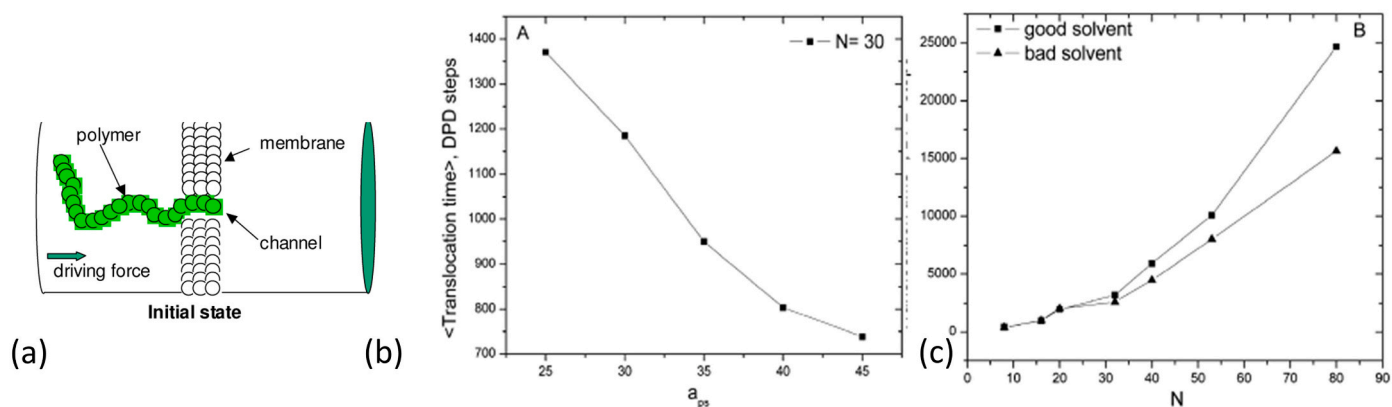


Fig. 11. (a) Initial simulation set up for driven polymer translocation in Yang et al., (b) Translocation time as a function of solvent quality, controlled by the polymer-solvent repulsion parameter a_{ps} . (c) Translocation time vs chain length at different solvent quality. Adapted with permission from Yang et al, ref. [217] copyright 2013, American Chemical Society. (For interpretation of the references to color in this figure legend, the reader is referred to the web version of this article.)

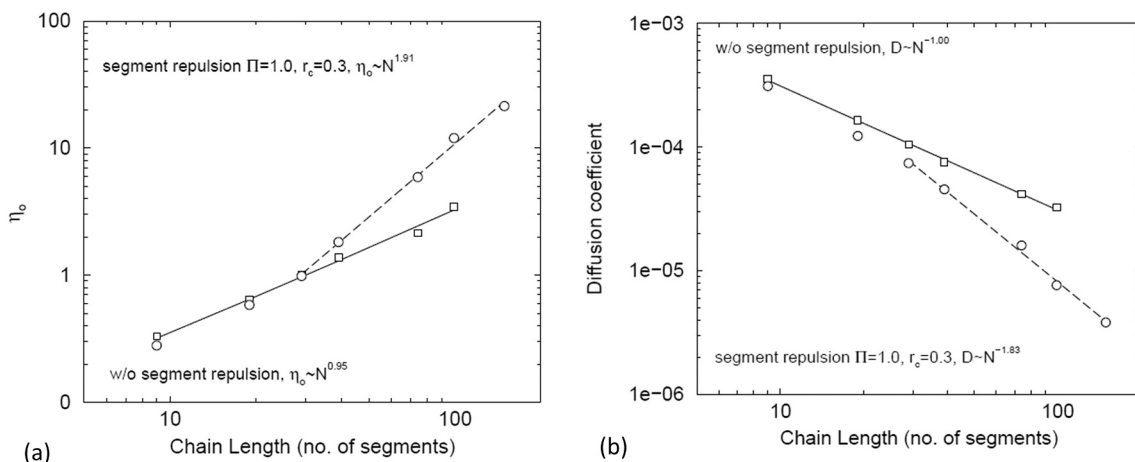


Fig. 12. Effects of entanglements in a DPD polymer melt, in presence of segment repulsion force. (a) Viscosity vs chain length. (b) Diffusion coefficient of the chain as a function of chain length. Adapted from Pan and Manke, ref. [225] with permission of World Scientific Publishing Co., Inc.

depends on the interaction parameter a_{ij} , which can be adjusted with choice of the CG level, while to control bond stretching, FENE bonds, which have finite extension with force being infinite at the cutoff, can be more effective compared to harmonic bonds. In coarse-grained models of polymer melts, obeying Langevin dynamics, Padding and Briels [221] developed an algorithm to prevent chain crossing by introducing *slippery elastic bands* between segments. Later, a multichain slip-spring model was introduced by Chappa et al. [222], and in DPD, this method was used by Langeloth et al. [223] to reproduce reptation dynamics and prevent bond crossing. Slip-springs, which are temporary crosslinks between the beads that moves along the chain according to an MC algorithm, can simulate the tube dynamics, envisioned by Doi and Edwards [206]. In a different approach, force between bonds or the spring-spring forces were used to enforce entanglements, introduced originally by Kumar and Larson [224] in Brownian Dynamics simulations. In DPD, such forces were introduced by Pan and Manke [225], via segmental repulsive potentials (SRP) of the same form as the DPD conservative potential but with larger repulsion strength and smaller interaction cut off, acting through the nearest contact distance between two bonds, which was found to prevent bond crossing. With the segmental repulsion, the authors observed that $D \sim N^{-1.8}$ for $N > 30$, which is close to the reptation behavior, while the viscosity behavior was found to be $\eta \sim N^2$, which is strongly non-Rouse but with the exponent that is well below the actual exponent 3.4 (Fig. 12a-b). Entanglement forces originating from segment repulsion were also used

by Goujon et al. [226], to study lubrication between two polymer brushes, while Sirk et al. [240] refined the use of such segmental repulsive potentials [225,227] and obtained a scaling $D \sim N^{-2.04}$.

The representation of polymers as chains of spherical beads is the reason why the unphysical chain crossing and topology violations occur, as the spherical beads leave low energy saddle points along the chains, as observed by Goujon et al. in very recent work [228]. In this work, the authors devised anisotropic beads to model polymers, that interact with anisotropic ellipsoidal potentials. In systems of polymer chains with prolate-shaped beads that orient along the backbone, the chain crossing probability was found to be significantly suppressed. Anisotropic bead models are promising, as they are more realistic when modelling polymers, and their effectiveness in reproducing polymer dynamics and computational implementation are to be explored.

Guerrault et al. [229] studied unentangled polyethylene and cis-polybutadiene polymer melts using DPD, by deriving the interaction parameters from potential of mean force obtained from microscopic MC simulations. They obtained scaling behavior consistent with Rouse dynamics, as shown earlier by Spensley [205]. Lahmar and Rousseau [230] studied unentangled melts, with DPD conservative parameters calculated with the same approach and specifically analyzed the effects of the friction coefficient (γ) and the cutoff distance (r_c) on the dynamics of the melts. In fact, the choice of r_c influences the friction force through the weight function w^D , and therefore γ and r_c can be combined to define an effective friction coefficient. The authors found that while structural

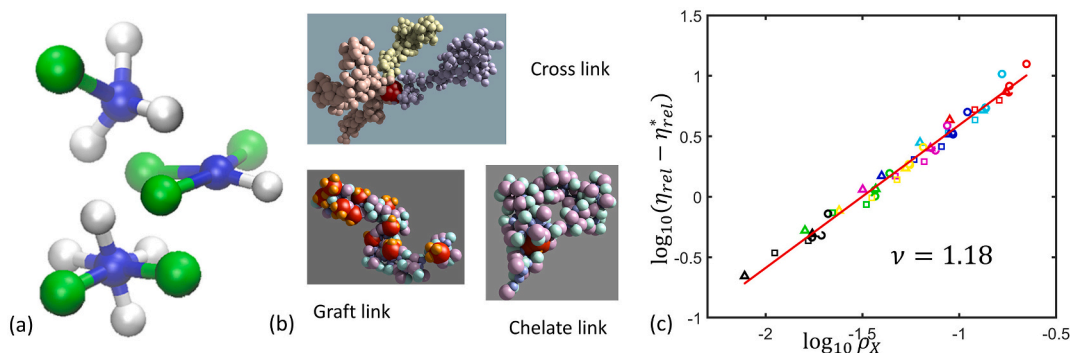


Fig. 13. (a) DPD models of coordinating metal ion. The central metal atom (blue) has coordinating sites bonded to it in a specific coordination geometry. To represent neutral metal chlorides, some of the coordination sites are assumed to be occupied by the chloride atoms (green) and other vacant sites (white) are available for coordination with other ligands. (b) Inter chain crosslinks, and intrachain chelate and graft links formed by metal complexation (red-vacant sites, orange-chlorine atoms) on the PVP polymer in solvent DMF. (c) Variation of the change in viscosity due to addition of metal chlorides as a function of the crosslink density ρ_X . Adapted from Santo et al., ref. [131] with permission, Copyright 2018, American Chemical Society. (For interpretation of the references to color in this figure legend, the reader is referred to the web version of this article.)

properties of the melts are unaffected by the choice of sufficiently large values of these parameters, the deviations from Rouse behavior of the melt observed within certain range. Yamanoi et al. [231] addressed additional problem of the effects of coarse-graining level on the flow properties of polymer melts, as a larger coarse-graining level increases repulsion parameter which eventually leads to system freezing. They circumvented this issue by introducing entanglement forces between the chains using the method of Goujon et al. [226] (see above) that can be tuned with the CG level, but setting the conservative forces turned off. Their approach reproduced various aspects of viscoelastic behavior, such as transition from Rouse to entanglement regimes. Wang and co-workers [232] studied conformational characteristics of chains in polyethylene/polypropylene blends in extension-dominated and shear-dominated flows. Sefiddashti et al. [233] developed a DPD model that is highly consistent with MD simulation data, for entangled polyethylene melts.

Systematic coarse-graining methods for entangled polymer melts have been reviewed by Padding and Briels [234].

5.1.3. Metal-polymer complexation

Santo and coworkers [131] introduced a novel DPD model for metal complexation in polymer systems and studied morphological and viscoelastic properties (Fig. 13). In this non-electrostatic model, to incorporate complexation effects, the metal atom is described as consisting of a central atom that is bonded to surrounding dummy atoms acting as coordination sites, that are arranged in a specific coordination geometry (Fig. 13a) such as planar, tetrahedral and octahedral. The dummy sites D, the number of which is equal to the coordination number of the metal, do not interact with any other bead ($a_{Dj} = 0$) but interact with ligands (specific polymer and solvent beads) via a truncated and smoothed Morse potential representing the coordination interaction. The effectiveness of the metal complexation model [131] was demonstrated by studying effects of addition of metal chlorides on the morphology and rheology of concentrated solutions of polyvinyl pyrrolidone (PVP) in dimethyl formamide (DMF). The simulations showed formation of different types of crosslinks (Fig. 13b), such as interchain crosslinks (X-links) in which the metal ion connects ligand beads from two different chains, the intrachain or chelate links (C-links) which connect ligand beads of the same chain, and the graft links (G-links) formed by metal ion coordinating with just one polymer ligand bead. The coordination bonds thus formed are reversible, as the Morse potential is of finite strength, and the effects of such reversible crosslinks on the viscosity of the polymers solutions was investigated. The analysis predicted a power law dependence of viscosity on the interchain crosslink density (Fig. 13c).

5.1.4. Block copolymers

DPD has been extensively used to study properties of block copolymers (BC). Initial studies by Groot et al. [235–236] investigated mesophase separation in block copolymer melts and the influence of hydrodynamic interactions on the separation. Groot and Madden [235] considered linear diblock copolymers (DBC) of the form A_nB_m with varying composition defined by the ratio of the length of the A-block relative to the total chain length $f = n/(n + m)$, with $n + m = N = 10$. According to self-consistent field theory (SCFT) [237], BC phase segregation is controlled by the factor χN and the composition f , where χ is the Flory Huggins parameter between A and B and the phase separation is predicted to start only beyond $\chi N > 10.5$. In DPD, the mismatch parameter Δq_{AB} is given by χ . The authors observed various phases and phase-transitions for high χN (~40–100) as f is varied from 0.1 to 0.5 from the disordered phase with $f < 0.1$, to tubular and spheroidal micelles at $f \geq 0.2$, followed by hexagonal and gyroid phases and finally lamellar phases as the copolymer composition becomes symmetric ($f = 0.5$). While the simulation results were in quantitative agreement with experiments and mean-field theory, the gyroid phase was found to be unstable contrary to theoretical prediction. In the subsequent study,

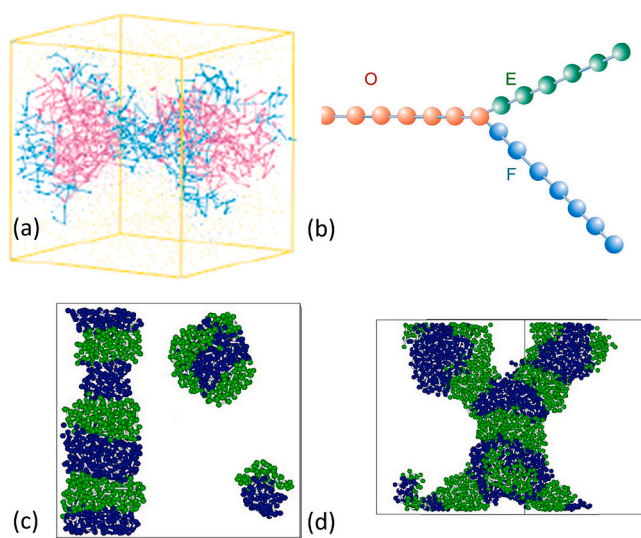


Fig. 14. (a) Intercluster micelles formed by $(EO)_{16}(PO)_{18}$ block copolymer (blue- EO, red-PO) in simulations of Cao et al.; adapted with permission from Cao et al. ref. [241], Copyright 2005, American Chemical Society. (b) The miktoarm TBC with hydrophilic (O), hydrophobic (F) and moderate hydrophobic (E) arms. (c) The segmented worm and sandwich micelles formed by the miktoarm TBC, the O segments surrounding the micelles are not shown for clarity. (d) The network of segmented worms with O segments removed. Adapted from Chou et al., ref. [246] with the permission of AIP publishing. (For interpretation of the references to color in this figure legend, the reader is referred to the web version of this article.)

Groot et al. [236] compared DBC phases in DPD and BD simulations, and showed that hydrodynamic interactions, which are not present in BD systems, play a crucial role in the evolution of the mesophases. Zhang and Manke [238], investigated DBC phases under shear flow and observed flow-induced microstructural transition at sufficiently high shear rates. With $\chi N = 60$, the simulations showed transition from spherical blocks to tubular structures that are oriented in the direction of the shear flow, while the cylindrical phase changed into the lamellar phase. The authors also found that the viscosity is enhanced by the extent of microphase separation in the DBC systems. Gavrilov et al. analyzed the phase diagrams of different types of BCs, monodisperse, polydisperse and random multiblock BCs, at different segregation limits (χN) and composition f [239]. While monodisperse diblocks reproduced the different phases and phase behavior with first order transitions predicted by SCFT and Monte Carlo simulations, polydisperse and random diblocks exhibited substantial deviations in phase behavior with continuous *order-to-disorder* transitions. Moreover, the random multiblock melts formed only lamellar morphologies. Microstructural and rheological properties of linear-dendritic diblock copolymer melts were studied by Liu et al. [240] In this case, the DBC consists of a linear A-block and a dendritic branched B-block, the properties of which were found to depend on the degree of branching.

Amphiphilic BC morphologies in a selective solvent at different levels of concentrations leads to supramolecular structures consisting of different types of micellar and lamellar objects, which are of potential interest in applications such as drug delivery. The micelles formed by BCs in such conditions, have two regions/compartments: the micellar core consisting of the solvophobic block and the micellar corona-the solvophilic outer shell. Cao et al. [241] investigated aggregation of diblock and triblock copolymers (TBC) of polyethylene oxide and polypropylene oxide in water. In the aqueous solutions, these BCs formed several types of micelles such as spherical, cylindrical and inter-cluster micelles (Fig. 14a), lamellae and gels, depending on the concentration. Sheng et al. [242] analyzed micellar characteristics of AB-diblock copolymers in water; the micelles are characterized by the aggregation

number P and micelle core radius R_{core} which are determined by the surface free energy $F_{interface}$ of the micelle core-solvent interface. The authors showed that, weight-averaged mean values of both P and R_{core} decrease as a power law with increase in the length of the soluble fraction, N_A of the polymer; $\langle P \rangle_w \sim N_A^{-\alpha}$; $R_{core} \sim N_A^{-\beta}$, with $\beta = \alpha/3$, and the values of these exponents depend on the inter-component parameter a_{AB} . In a following work, the authors considered micelle structures of $(AB)_n$ and $(BA)_n$ star block copolymers (n being the number of AB diblock arms, A is solvophilic and B is solvophobic) and found that, with large n , $(BA)_n$ formed unimolecular micelles with solvophobic B in the core, however, $(AB)_n$ formed supramolecular structures as a result of B being at the outer edges of the arms and henceforth exposed.

ABA type TBCs in a mid-block selective solvent were studied by Sliozberg and coworkers [243], which formed gel networks of micellar blocks connected by loops and bridges. In this work, TBCs of poly(styrene-isoprene-styrene) were modelled, and the viscoelastic properties of the gels were studied by applying oscillatory shear. The fraction of bridges and elastic moduli were calculated, however, due to lack of entanglement forces in the simulations, the results remained applicable only in the short chain limit. BCs are also used in separating wastewater from crude oil. Alvarez et al. [244] performed DPD simulations of ethylene oxide-propylene oxide-ethylene oxide triblock co-polymers functionalized with diethanolamine in crude oil-water emulsions, and showed that water coalescence rates increased with chain-length. Multi-compartment micelles can be formed by self-assembling polymers with more than two types of blocks. For instance, ABC triblock copolymers, with A, B and C blocks being mutually immiscible, can form micellar morphologies such as core-shell-corona (CSC) and segmented worm (SW) micelles [245]. DPD simulations of miktoarm star and linear ABC copolymers (Fig. 14b-d) in water confirmed existence of CSC and SW forms and other additional morphologies [246]. Guo et al. [247] performed DPD simulations of paclitaxel (PTX), a drug that is used to treat various cancers, and PTX loaded with diblock poly(ethylene oxide)-b-poly(lactide) (PEO-b-PLA) in water. Poor solubility of PTX in water, makes it difficult to be administered as a drug. These simulations showed that while PTX formed fiber or ribbon-like structures in water, PTX loaded with PEO-b-PLA formed micellar structures. Lin et al. [248] studied with experiments and DPD simulations, the release of the cancer drug Doxorubicin (DOX) from poly-caprolactone (PCL)-based $A_2(BC)_2$ type miktoarm block copolymer micelles under changes in pH conditions. Wang et al. [249] studied vesicles formed of mixture of amphiphilic comb-like block copolymers and found that the structural transitions in the vesicles such as fission are governed by line tension between different copolymer phases. Yu et al. [250] studied porous membranes of block copolymers using DPD and studied nanofiltration and transport properties.

5.1.5. Polymer brushes

Polymer brushes (PBs) having polymers with one end grafted on a solid surface constitute another class of important polymeric systems that can be well-described by DPD, an excellent review on which is provided by Binder et al. [251] Applications of polymer brushes include lubrication, colloidal stabilization, oil-recovery process, chromatographic separation and smart microfluidic channels [252]. Properties of polymer-grafted surfaces can be tuned by many parameters, such as grafting density, chain length and solvent quality. A PB in a solvent undergoes conformational changes from expanded to collapsed state as the solvent quality is varied from good to bad. Malfrey and Tildesley [123] analyzed polymer brushes grafted on the either walls of a slit pore in a good solvent and showed that DPD can be efficiently used to study PBs. The PBs exhibited a parabolic density profiles towards the center of the channel in agreement with self-consistent field theory. The thickness of the brushes increased with surface coverage and chain length, while chain ordering increased with chain length for a given surface coverage. Irfachsyad et al. [253], studied two opposing PBs under shear flow created by sliding wall boundary conditions and observed that PB width

is decreased by decreasing the solvent quality as well as increasing the shear rate. Furthermore, a tilt in the orientation of polymer chains in the direction of the flow was observed due to shear. Wijmans and Smit [254] characterized shear flow between two parallel walls in DPD simulation by moving one of the walls and studied effects constant and oscillatory shear on PBs. They also found that the thickness of PB decreases when shear flow is applied, as the PB is stretched along the direction of the flow. Pal and Seidel [255] analyzed PBs and compared the DPD results with previous SCF and MD simulations of LJ systems [256] and showed that DPD effectively reproduces MD results with appropriate parameterization. Pastorino et al. [257–258] compared DPD and Langevin thermostats for shear flow of polymer melts between two opposing PBs and concluded that both methods suffer from artifacts. Cheng et al. [259] analyzed behavior of grafted polymers at different solvent quality in the mushroom and brush regimes, by performing DPD simulations of grafted polymers in a binary solvent consisting of good and bad solvent components at varying composition.

Deng et al. [260] investigated shear-driven (created by moving the upper wall) and pressure-driven flow (created by applying a constant force to solvent beads) over a PB-grafted surface, representing semi-flexible glycocalyx fibers. The brush thickness h was estimated from the first moment of the brush density profiles and the slip length l_{slip} was measured as the hydrodynamic penetration length of the flow into the PB; the flow did not penetrate to full PB interior but to only a small extent on the PB surface. The simulations showed that both brush density profiles and slip length are unaffected in the weak shear regime until a critical shear rate $\dot{\gamma}_0$, which scales as a power law with grafting density, however, both density and slip length are affected by the flow in the strong shear regime above $\dot{\gamma}_0$. Santo et al. [261–262] analyzed Poiseuille flow in a PB-grafted slit-channel and observed that the solvent within the PB is immobile and defined the *hydrodynamic width* of the PB (w_{PB}) as the height of the PB region that is impenetrable to the flow. Li et al. [263] considered solvent flow through PB-grafted cylindrical nanochannels ('smart' channels), at different solvent quality and showed that the internal diameter of the channel pore is determined by the solvent quality, being wider with bad solvent due to PB collapse but narrower with good solvent in which the PB expands and thus tends to close the nano pore.

Forces of compression between two opposing PBs in contact have been analyzed theoretically and using computer simulations, in studying lubrication process. Goujon et al. [264] developed DPD in grand canonical ensemble and studied frictional forces between two PBs as a function of compression, shear rate and solvent quality. The compression forces between the PBs showed good agreement with Alexander-de Gennes theory [265]. The effects of entanglements on the frictional and rheological properties between PBs at different solvent quality were later analyzed [226,266] by introducing *spring-spring* forces between the segments. It was found that the force-distance scaling laws [265] are unaffected by the incorporation of entanglements, however, the reduction in bond crossing led to increase in friction between the PBs and the viscosity, establishing that entanglements are crucial for studying rheological properties of PBs. In later studies [267], the authors considered friction between polyelectrolyte brushes, the charge on the polymers was found to affect the friction between two PBs and the viscosity; the friction coefficient was found to be larger than that of neutral brushes at low compressions, but smaller at high compressions. Additionally, the internal conformational ordering was found increased in charged PBs.

5.1.6. Biopolymers

Symeonidis et al. [268] investigated rheological properties of λ -phase DNA using DPD by modelling the polymer as worm-like chain and using Lowe's thermostat. Fan et al. [121] studied flow of DNA suspension in microchannels using the wormlike chain model for polymer and a modified DPD weight function $\omega^R(r)$. Size-dependent entropic trapping of DNA molecules during the electrophoretic migration though

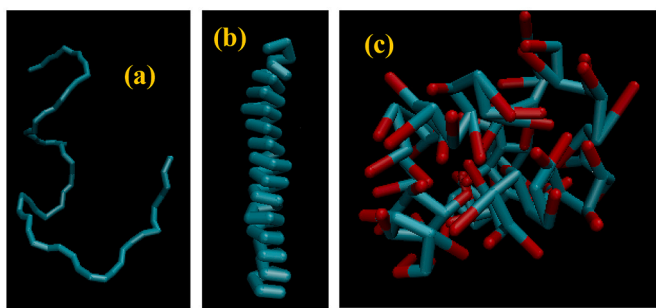


Fig. 15. Different secondary structures of a model peptide (showing only the backbone) (a) random coil and (b) α -helical. (c) Globule structure of another model peptide with considerable α -helical content. Adapted from Vishnyakov et al., ref. [136], Copyright 2012, American Chemical Society. (For interpretation of the references to color in this figure legend, the reader is referred to the web version of this article.)

narrow constrictions, was analyzed by Moeendarbary and coworkers [269–270], who observed that longer DNA chains pass through the channel faster, while the shorter ones get trapped in the deeper regions of the channel, demonstrating the size-dependent DNA separation. In a more recent work, Ranjith et al. [271] used *single-particle DPD* (Section 3.8.1) to analyze size-dependent DNA separation in hydrophobic and hydrophilic channels. Valdivia and Jaime [272] studied spontaneous internalization of single stranded DNA (ssDNA) through a transmembrane single walled carbon nanotube (SWCNT) channel, using a combination of DPD and Monte Carlo, while quantum mechanical DFT is used to parametrize the DPD interaction parameters. This study showed that the ssDNA internalization is slowed by the narrowness of the tube as well as the hydrophobic interactions with the nucleic acid bases.

Flow and aggregation of rod-like proteins through polymer brush grafted channels were studied using DPD by Posel et al. [273] As the solvent quality is varied, the brush undergoes stretch-to-collapse transition; the protein flow is hampered in the stretched (good solvent) brush conditions which causes aggregation of proteins, while protein flow occurs at collapsed brush conditions, suppressing the aggregation. In designing multifunctional porous structures through protein-directed nanoparticle assembly, Li et al. [274] performed DPD simulations to observe various supramolecular structures generated through gelatin-directed self-assembly of carbon-black particles. Wang et al. [275] studied blood clot formation at vascular injury due to non-physiological shear stresses (NPSS) caused by the blood contacting medical devices, by modelling collagen-platelet and inter platelet interactions using DPD. Zhai and coworkers [276] studied the intermediate scattering function (ISF) of the monoclonal antibody (mAb) protein using DPD simulations.

In standard DPD, it is not possible to include hydrogen bonding with the all-repulsive conservative interaction parameter a_{ij} . As a result, details of the protein secondary structure, such as α helices and β sheets cannot be incorporated. Vishnyakov et al. [136], however, introduced a DPD model to simulate protein secondary structures, which incorporates hydrogen bonds through dissociable Morse bonds (Section 3.6). This model successfully demonstrated coil-globule transition involving α -helical and β -hairpin structures of the polypeptide α -synuclein at different pHs (Fig. 15). Peter et al. [277] developed a DPD polarizable protein model along with a polarizable water model. The polarizable protein backbone consisted of electric dipoles that mimic hydrogen bonding along the backbone to reproduce the secondary structures. The model was validated against experimental structures of a number of proteins. Kawai and co-workers [278] analyzed the stability of amyloid β ($A\beta$) dodecamer, with the protein secondary structure modelled using ref. [136] Okuwaki et al. [279] used Morse potentials to perform folding of proteins, using DPD with interaction parameters derived from a fragment molecular orbital (FMO) calculations. Choudhary and Kukse-nok [280] developed the first native-based DPD approach to protein α

helical folding; the folding is demonstrated by choosing a lower repulsion parameter between contact pair residues, which led to folding.

5.1.7. Polysaccharides

DPD has been applied to polysaccharide systems as well. A very recent work by Santo and coworkers [143] presented a multiscale modelling of aqueous solutions of the industrially relevant polysaccharide Xanthan Gum (XG) containing Zn ions. XG is used in many applications, mainly as a viscosity controller in industrial food, cosmetic and healthcare products. The XG conformational and rheological properties are thought to depend on the composition, in terms of the content of pyruvate and acetate groups in the XG chains. The authors devised an approach to model XG chains of different composition and studied the conformational and rheological properties of XG solutions containing Zn salt at different pyruvate and acetate contents. The Zn complexation model with XG chains was modelled following the metal complexation model [131] described in Section 5.1.3. While atomistic simulations revealed strong influence of Zn ions on the conformation of the chains, inducing loop-like structures by crosslinking between side chains, DPD simulations at shear flow showed that chains form bundles by interchain crosslinking and undergo a gel-sol transition at sufficiently high shear rates and polymer concentrations. Overall, it was found that salt effects are enhanced by pyruvate content in the chains, an observation that can have practical implications in the industrial use of XGs.

5.2. Polyelectrolyte solutions and membranes

5.2.1. Polyelectrolyte solutions

DPD simulations of polyelectrolyte (PE) systems became possible when Groot [45] introduced electrostatic interactions in DPD through the smeared charge approach and simulated polyelectrolyte-surfactant interactions. It was shown that the cationic polyelectrolyte wraps around the anionic surfactant due to electrostatic attraction. Ibergay et al. [281] studied polyelectrolyte brushes with both PPPM approach of Groot [45] and Ewald summation of Gonzalez et al. [46] and suggested that PPPM is slightly better. Complex formation between oppositely charged linear polyelectrolytes was investigated by Gonzalez-Melchor and coworkers [282], who observed that the presence of salt enhances the complex formation. Gavrilov et al. [283] analyzed conformational behavior of polyelectrolyte chains with small and bulky counter ions; the small ions were of the same size as the monomers, but bulky ions were larger solid-like particles consisting of several beads strongly bound together with one of bead being charged. Depending on the position of the charged bead in the solid particle, the bulky ions were either symmetric with the charged bead at the center and asymmetric with the charged bead on the surface. The DPD simulations showed that, with small and symmetric bulky ions, the PE assumed a collapsed globular state when the fraction of charged monomers is high, while with asymmetric bulky ions, the chain remained in swollen state without collapsing. Li et al. [284] devised the implicit solvent ionic strength (ISIS) DPD modelling to study self-assembly of block polyelectrolytes at different salt concentrations. The ISIS model captures the electrostatic interactions based on a mean-field approximation of the ionic interactions that reproduces the ionic strength effects in the simulations. However, this model is suitable at sufficiently large ionic strength, where the mean-field approximation holds. DPD studies of polyelectrolyte self-assembly have been reviewed by Lissal et al. [285] The same group [286] studied self-assembly of *co*-polyelectrolytes consisting of a hydrophobic block and a polyelectrolyte block. The formed core-shell micelles having PE shell became unstable with increasing ionization. Another work [287] studied association of copolymers consisting of neutral hydrophilic and a positively or negatively charged polyelectrolyte block. Zhou et al. [288] studied rheological properties of mixed solutions of wormlike micelles and polyelectrolytes. At low shear rates, the addition of polyelectrolytes increased viscosity of the wormlike micelle solution due to entanglement between micelles and the

polymer, while additional influences such as shear hysteresis, shear thickening and increase of viscoelastic moduli were observed at different conditions of shear.

5.2.2. Morphology and water transport in polyelectrolyte membranes

An industrially important PE system is the polyelectrolyte membrane (PEM) such as Nafion of Du Pont. PEMs are used in applications requiring selective transport of ions or molecules, such as fuel cells, gas and liquid separations and water treatment. Nafion is an anionic polyelectrolyte with a hydrophobic backbone and a sulfonate anion present on the pendant side chains. Upon hydration, the membrane undergoes segregation into hydrophilic and hydrophobic phases, with sulfonates, counter ions and water in the hydrophilic phase and the perfluoro alkyl groups in the backbone and the perfluoro ether groups in the side chains of the polymers comprising the hydrophobic phase. The morphology of the hydrated PEM changes with hydration; the swelling increases to reach the saturation and the transport properties such as water and ion diffusion and conductivity increases with hydration, depending on the morphological transitions during hydration increase. Morphologies and water and ionic diffusion in PEMs have been studied using DPD by many authors [138–139,289–293]. Yamamoto and Hyodo [293], studied hydrated Nafion membranes by DPD simulations, parametrizing the system with Flory-Huggins parameters, with water content levels varying from 10 to 30 vol%. They found that the size of the water clusters in the membrane as well as the spacing between them increases with water content in the above-specified range. Dorenbos and Suga [289], analyzed the equivalent weight (EW- grams of Nafion per mole of the sulfonate (SO_3) group) dependence of Nafion morphologies, and found that the average water pore size R_{pore} and inter-cluster distance $D_{\text{cl-cl}}$, increases linearly with EW. The authors calculated the water diffusion

coefficients in the porous membranes using a Monte Carlo approach, which were found to decrease with EW. The same group [290,292] further analyzed water diffusion characteristics of ionomer Nafion membranes on the chain architecture, the side chain distribution along the backbone and length of the side chain. It was found that the diffusion coefficient is larger and percolation threshold is lower for the chains with bi-modal side chain distribution (distance between the successive side chains is short and long alternatively), compared to chains with uniformly distributed side chains. For uniformly distributed chains, the diffusion coefficient increases with side chain length, while it was found to decrease with side chain length for the bi-modal case. However, none of these works considered electrostatic interactions.

Neimark group performed DPD simulations of Nafion and sulfonated polystyrene (sPS) membranes and studied proton and cation conductivity and water diffusion [138–139,142,291]. A DPD model of metal-substituted Nafion membranes, with monovalent metal cations modelled as hydrated ion beads with charge +1, was developed with electrostatic interactions explicitly included using the smeared charge approach. This work analyzed self-assembled morphologies (Fig. 16a), percolation threshold, pore-size distributions, water and cation diffusion coefficients and water sorption isotherms (Fig. 16b) of Nafion membranes of different EW at different hydration levels λ defined as the

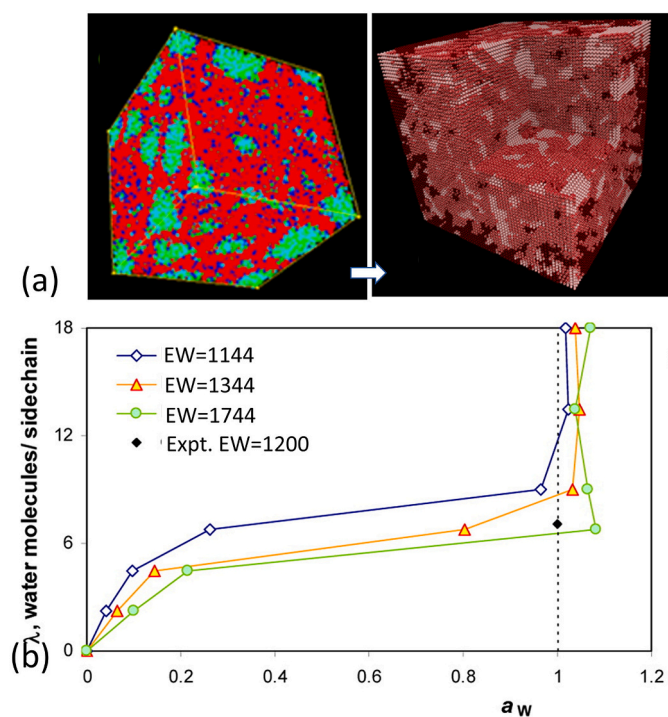


Fig. 16. (a) Left: Morphology of hydrated metal-substituted Nafion membrane (EW 1144) at $\lambda=9$ in DPD simulations. Colors: Nafion backbone and perfluoro ether side chains in red, sulfonate in dark blue, counter ions in green and water in light blue. Right: Digitalized biphasic lattice replica of the morphology on the left- the hydrophilic subphase is shown in light pink. (b) Water adsorption isotherms of Nafion membranes of various EW. Adapted from Vishnyakov and Neimark ref. [291], with permission Copyright 2014, American Chemical Society. (For interpretation of the references to color in this figure legend, the reader is referred to the web version of this article.)

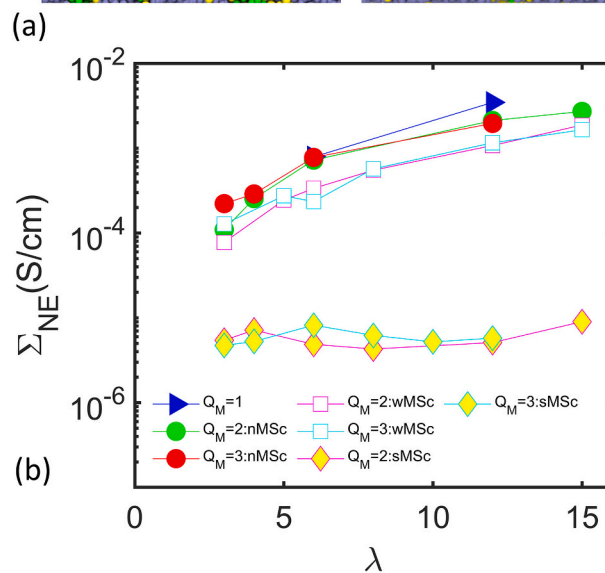
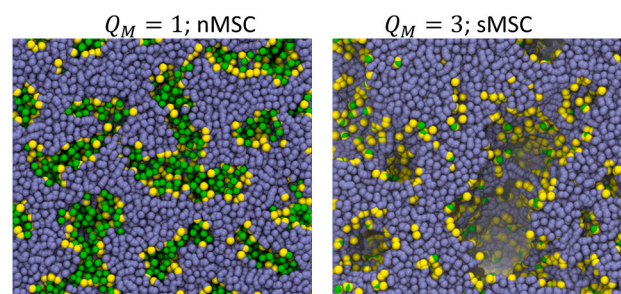


Fig. 17. (a) The change in morphology induced by interfacial crosslinking induced by multivalent ions in Nafion MPEMs. Left: Morphology of monovalent ion-doped membrane at $\lambda = 12$ with no M-S coordination (nMSC) present. Right: Morphology of trivalent ion-doped membrane at the same hydration level, with strong M-S coordination (sMSC). Colors: hydrophobic backbone - iceblue; sulfonate-yellow, metal ion-green. Water particles are not shown to display the porous structure (b) Ionic conductivity of MPEMs containing metal ions of different valency (Q_M) and M-S coordination at different hydration levels. wMSC stands for a case of weak M-S coordination. Adapted from Santo and Neimark, ref. [142] with permission Copyright (2021) from Elsevier. (For interpretation of the references to color in this figure legend, the reader is referred to the web version of this article.)

water to sulfonate *mol* ratio. Furthermore, the authors developed a methodology to calculate water diffusion coefficient by performing random walks in a biphasic lattice corresponding to a membrane morphology at a particular instant (Fig. 16a, right). This *static* diffusion coefficient that is calculated in a morphology at a particular instant does not have contributions of morphological fluctuations over time, which was then compared with *dynamic* diffusion coefficient of water that is calculated from the mean square displacements (MSDs) over time, using Einstein's relation. The water sorption isotherms for different Nafion membranes are obtained by calculating the activity $a_W(\lambda)$ from chemical potential of water in the membrane by a Monte Carlo Widom insertion method (Fig. 16b). The isotherms can be used to determine the hydration level of saturation point for which $a_W \leq 1$.

5.2.3. Metal complexation in polyelectrolytes

In a recent work, the authors [142] developed a metal ion complexation (MIC) model to study the properties of metal complexed polyelectrolyte membranes, called *metallo-polyelectrolyte membranes* (MPEMs). In this model, the metal ion is represented as a central charged atom surrounded with dummy atoms that act as coordination sites, in a specified geometry, as in the previous work [131] (Fig. 13). The coordination interactions were modelled using a Morse potential, parametrized by matching metal-ligand running coordination numbers (RCN) and diffusion coefficient of the ions in water. The MIC model replaces the conventional hydrated charged sphere (HCS) models of metal ions, in the ability to form complexes that leads to formation of crosslinks between the polymers. The authors considered effects of complexation between metal ion (M) and the sulfonate (S) groups of the Nafion chains and found that metal-sulfonate coordination drastically influences the morphological as well as transport characteristics of the MPEMs. As the sulfonate groups reside at the hydrophobic-hydrophilic interface, the crosslinking occurs at the interface and such interfacial crosslinks increases the interfacial tension, leading to change in morphology into more spheroidal water clusters (Fig. 17a). It was found that strong M-S coordination leads to increase in pore sizes (Fig. 17a). Such a change in morphology was analyzed in terms of pore-size distributions and the interfacial area and was found to cause water subdiffusion, and reduction in water diffusion coefficient and ionic conductivity, in semiquantitative agreement with experimental observations. In particular it was found that ionic diffusion and conductivity (Fig. 17b) is better described with the MIC model with inclusion of the

coordination interaction, rather than the HCS models.

5.2.4. DPD model of proton transport

A DPD model for proton dissociation and transfer in aqueous solutions was suggested by Lee et al. [137] In this model, proton is described as a spherical entity of mass $1 \text{ Da} = 1/18 M_W$ (mass of water bead) in the DPD simulations, which interacts with proton-acceptor beads and make dissociable bonds, modelled as a Morse potential, truncated at a certain interaction cut-off r^M . The Morse parameters are optimized by matching with proton mobility in water and the dissociation constant with benzene sulfonic acid. The proton that is associated with a water particle can be transferred to other water particles, through a mechanism depicted in Fig. 18a which involves stages of complex formation with water, a transient state upon interaction with another water bead, and the subsequent breakup. The potential energy profile of this interaction is given in Fig. 18b as function of water-water distance as reaction coordinate. With this model, the proton hopping between water beads was demonstrated as predicted by Grotthuss mechanism. In subsequent works [138–139] on the morphological and transport properties of hydrated Nafion and sulfonated polystyrene (sPS) membranes, the proton hopping model was employed to analyze proton transport in the membranes at different hydration levels. The ratio of proton to water self-diffusion coefficients was found to depend on the hydration level in good agreement with experimental results.

5.2.5. Polyelectrolytes on surfaces

Alarcon et al. [294] analyzed adsorption of weak polyelectrolytes on neutral surfaces and oppositely and likely charged surfaces, and observed that adsorption reduces with increase of degree of ionization of the PE. Cao et al. [295] considered electrophoresis of branched bottle-brush polyelectrolytes (BPEs), through a nanochannel. The BPEs were found to migrate through the channels at strong electric fields, and a stretching-shrinking motion was observed when the channel is narrow. Yan and Guo [296] investigated conformational properties of polyelectrolyte chains grafted on single-walled carbon nanotubes and analyzed orientational behavior of the chains at different salt contents. In this case, increasing the counter ion valency led to changes in PE orientation over the SWCNTs. The same group [297] also performed DPD simulations of cylindrical polyelectrolyte brushes (CPBs), which are polymer chains with densely grafted with multiple side-chains. The authors showed that conformational properties of the CPBs are greatly

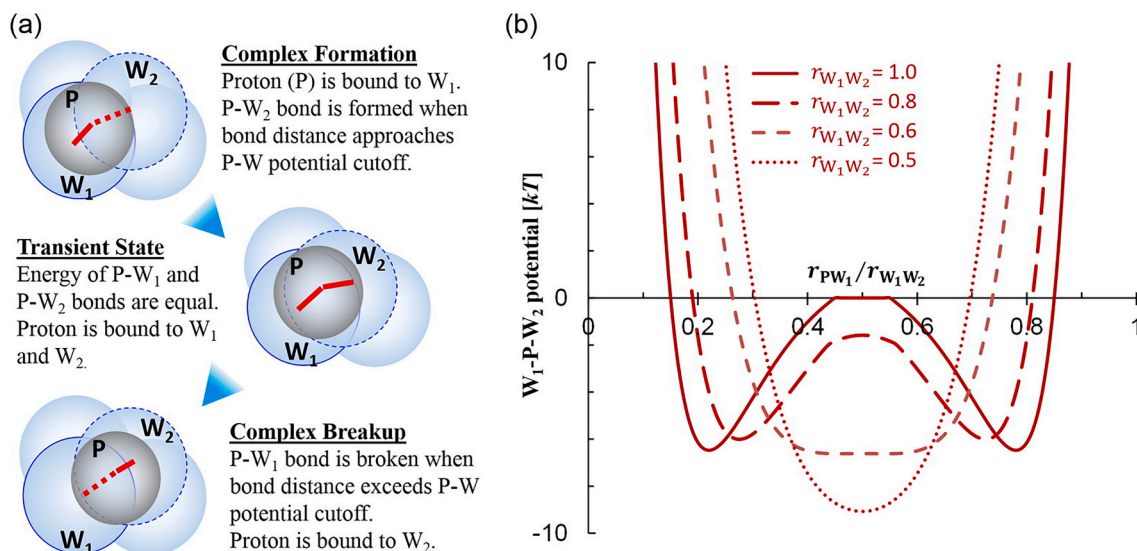


Fig. 18. (a) Schematic representation of the proton association and break-up with water. (b) The potential energy of the W-P-W complex along the reaction coordinate of proton transfer. Adapted from Lee et al., ref. [137], Copyright 2015, American Chemical Society. (For interpretation of the references to color in this figure legend, the reader is referred to the web version of this article.)

tuned by the valency of the counter ions. Nagarajan and Chen [298] performed DPD simulations of the translocation of star polyelectrolytes through a nanopore. The critical electric field for translocation was found to increase with number of arms in the star, while the mechanism of translocation differed considerably from the linear polymer translocation, with significant delay for the branch point to enter the pore. Smiatek and Schmid [299] showed that the mobility of PEs during electrophoresis in nanochannels is influenced by the electroosmotic flow. Sirchabesan and Giasson [300] studied polyelectrolyte brushes under compression and lateral shear force. They observed that the mutual interpenetration of the charged brushes upon compression is negligible, while interpenetration increases with electrostatic screening or when the PEs are weakly charged. The friction between the brushes increases with and is directly correlated to the interpenetration thickness.

5.3. Surfactant solutions

5.3.1. Self-assembled surfactant structures

Venturoli and Smit [301–302] showed that DPD can be used to simulate surfactant self-assembly into bilayer membranes and studied the effects of surfactant chain length and stiffness on the properties of the membranes. Groot studied formation of polymer-surfactant complexes in water [218]. In this work, two modes of polymer-surfactant adsorption were observed depending on the specifics of polymer-surfactant interaction: if the polymer dominantly interact with hydrophobic tails of the surfactant, then continuous surfactant adsorption occurs forming bottle-brush or swollen cage conformations, while if the polymer interact more strongly with the head groups, then the surfactant first form micelles which then adsorb on the polymer, leading to necklaces of micelles on the polymer. Yamamoto et al. [303] used DPD to study vesicles formation of amphiphilic molecules and shape changes; the authors simulated spontaneous formation of vesicles from initial random and bilayer configurations and showed that two-tailed amphiphiles form vesicles faster. Subsequent studies from the authors analyzed shape deformation and fission dynamics of two-component vesicles [304] and the crossing dynamics at an entanglement point between thread-like micelles consisting of different surfactants [305]. Multicomponent vesicle dynamics, the 2D phases and budding, was also studied by Laradji and Sunil Kumar [306].

Shang and coworkers [307] performed DPD simulations of Gemini surfactant-SDS mixtures and showed that the vesicles formed are mostly multilamellar. Li et al. [308] investigated the conditions influencing micelle-to-vesicle transitions in *catanionic* mixtures of SDS and DTAB. Li et al. showed that incorporation of bond-angle potentials, which was discarded in the previous works, are essential to simulate inverted lipid phases, such as inverted cubic, hexagonal and bicontinuous phases [309]. Fluorinated surfactants are another class of surfactants with fluorocarbon tails. Sun et al. [310] studied aggregation of fluorinated surfactants and analyzed the difference between their hydrocarbon analogues. The fluorocarbon-tailed surfactants were found to exhibit similar sequences of self-assembled structures as in the case of hydrocarbon-tailed ones, while some differences were in the formation of lamellar and hexagonal phases with little curvature and in the formation of rod-like micelles and ellipsoids at low concentrations, instead of spherical micelles. Yang and coworkers [311] investigated aqueous phase behavior of the anionic surfactant aerosol OT which exhibits lamellar phase predominantly for a wide range of concentration and temperature. Anderson et al. [194] studied phase behavior of sodium lauryl ethoxy sulfate in aqueous solutions.

5.3.2. Surfactant monolayers and interfacial properties

Several studies analyzed surfactant monolayers, such as sodium dodecyl sulfate (SDS) layers at oil/water interface [312–313]. Dong et al. [314] investigated monolayers of sodium dodecyl sulfonate and sodium dodecyl sulfate at water/CCl₄ interface, and showed, by

monitoring the root mean-square end-to-end distance of the chains, that stretching and ordering of chains increases with increase of surfactant concentration as well as on addition of salt. Li et al. [313] studied by experiments and by means of DPD simulations, the interfacial activity of sodium dodecyl benzene sulfonate (SDBS) and sodium oleate (OAS) surfactants at oil/water interface. The authors reported that the interfacial activity depends on the surfactant concentration as well as packing of hydrophobic tails within the oil phase, the packing is compact when both surfactant tails and the oil molecules have similar structure. For instance, SDBS reduces interfacial tension of toluene/water interface to a lower value than it does for *n*-octane/water interface, while OAS reduces *n*-octane/water tension much lower than it does for toluene/water. This is ascribed to the presence of phenyl/alkyl groups of the surfactants influencing the interfacial packing.

Rekvič et al. [315], investigated the efficiency of surfactants in reducing interfacial tension at oil-water interface, in regard to their size and structure. The study found that the interfacial tension is lowered as the surfactant length, and the size and ionicity of the head groups increased. Furthermore, they found that branched surfactants are more efficient than their linear counterparts if the head group is hydrophilic enough to form a layer despite steric repulsions between the tails, or the oil-head repulsion is sufficiently strong. Surfactants with linear tails were found to adsorb faster when placed in the bulk water phase. The same group studied surface forces between surfactant monolayer-coated emulsion droplets [112], which determine the emulsion stability. In the case of water droplets in oil (water-in-oil emulsions), steric repulsion between the monolayer tails facing each other, tends to prevent the coalescence between them. Oil droplets in water (oil-in-water emulsions) are more prone to merge, in the absence of such repulsion between the facing head groups. In another work, the group used DPD simulations to study the surfactant chain length dependence of bending modulus of monolayers at oil-water interfaces [316], and obtained a power law dependence of the modulus on the chain length, with the exponent values in the range 1–2, similar to but lower than the mean-field theory and experimental predictions. Deguillard et al. [317] showed that the interfacial tension of the oil-water surfactant system depends strongly on intramolecular forces, the parameters such as bond force constants and bond lengths. Ginzberg et al. [318] compared SCFT and DPD models of interfacial tension of oil-water interface containing alkyl ethoxylate surfactant, and found a good semi-quantitative agreement between the two models and the experiments. Khedr and Striolo [319] compared DPD parameterization methods based on the Hildebrand and Hansen solubility parameters, mapped into the Flory-Huggins theory (Section 4.1), for simulating oil-water interface and aqueous surfactant systems. The authors found that by utilizing Hansen solubility parameters, high degree of coarse-graining and realistic interfacial tensions can be achieved. The effects of hydrophile-lipophile balance (HLB) [320] of the surfactants on the oil-in-water emulsion stability was investigated by Liang et al. [321], who found that the interfacial tension is minimum at a value of HLB equal to 13 for nonionic surfactants.

In an effort to overcome the limitation that standard DPD cannot simulate liquid-vapor coexistence [4], Wang et al. [174] suggested a novel DPD gas model for simulating surfactant adsorption at gas-liquid interface, by modelling the gas phase composed of beads that interact with liquid phase particles through a hard core interaction potential (Section 3.8.1) [173]. The parameters of gas-liquid interaction potential was estimated by a scheme that reproduces surface tension and gas-liquid interfacial density profiles. Such a model is simple and draws comparison from the *free volume* approaches in self-consistent theory [322], however, the effectiveness of this model in quantitatively predicting interfacial tension of surfactant-adsorbed air-water interface below CMC was found to be excellent, considering the fact that most of the existing atomistic and CG water models severely underestimate air-water surface tension.

5.3.3. Critical micelle concentration

Pool and Bolhuis [323] compared micelle formation in hard core LJ systems with soft core DPD systems and found that while the LJ systems exhibited critical micelle concentration (CMC) in the experimental range, CMC in the DPD systems were several orders of magnitude lower. This raised the question that whether soft potentials can correctly describe the micellization process. Vishnyakov and coworkers [159] argued that this was due to lack of quantitative modelling based on experimental data. This work introduced a DPD parameterization scheme based on matching infinite dilution activity coefficients (Section 4.2) and obtained CMC of several nonionic surfactants in quantitative agreement with experiments. In a subsequent study, the authors [157] showed that chain rigidity of the surfactants has significant influence on the CMC, rigid surfactants have smaller CMC and better-defined micelles. The CMC of ionic surfactants and effects of salts on micellization was then analyzed [158] with the same approach augmented with electrostatic interactions incorporated using the smeared charge approach of Melchor et al. [46]

Self-assembled structures of the Gemini surfactant dodecyl sulfonate sodium, were studied by Deng et al. [324] who observed several micellar and lamellar morphologies and calculated CMC in agreement with experimental results. Surfactant adsorption on single-walled carbon nanotubes (SWCNT) below CMC was studied by Angelikopoulos et al. [325], who observed that micelle-like adsorption on the tubes starts and completes at surfactant concentrations much below CMC (<0.5 CMC). Li et al. [326] analyzed effects of difference in molecular structure on the surfactant self-assembly, and observed that, as the tail length increases the CMC decreases, while the micellar size increases. However, the increase in head group length leads to increase in CMC. Also, having branched tails was found to promote micellization. Mai et al. [327] developed a DPD parameterization scheme for alkyl sulfate surfactants, in which the interaction parameters such as repulsion parameters and angle parameters controlling the rigidity of the surfactant are adjusted to reproduce experimental CMC and average micelle aggregation number (N_{agg}). Anderson et al. [193] used DPD parametrization based on matching density and water-octanol partition coefficients (Section 4.7), to study micelle formation of alkyl sulfates and obtained CMC in good agreement with experiments.

5.4. Lipid membranes

Lipid membranes constitute biological cell membranes that protect the cell, the properties of which is vital in the biological functions of the

cell. Cell membranes are complex mixtures of charged and zwitterionic lipids; mostly comprised of phospholipids, such as phosphatidyl choline (PC), phosphatidyl serine (PS), phosphatidyl ethanolamine (PE), phosphatidyl Inositol (PI), cholesterol, sphingolipids and glycolipids. Besides lipids, the cell membrane also contains integral membrane proteins. Given the micrometer range length scale and inhomogeneity of cell membranes, mesoscale methods are essential to study the properties of such systems; DPD becomes a natural choice to study material and structural properties of lipid membranes and membrane-protein interactions.

Stability of mixed bilayers containing PE lipids and non-ionic surfactants was investigated by Groot and Rabbone [41], in order to study the cell membrane damage in presence of non-ionic surfactants. The interaction parameters are developed by reproducing the solubility and compressibility of reference compounds. The simulations showed that as the surfactant fraction is increased in the bilayer, transient holes started to appear which became permanent at high surfactant fractions. Surfactants reduced extensibility and mechanical strength of the membranes. Shillcock and Lipowsky [328] performed DPD simulations of bilayers formed by single- and double-tailed amphiphiles to analyze in detail the equilibrium structure of the bilayers depicted by density profiles and lateral pressure profiles. The authors found that strong tail stiffness is essential to create lamellar order. Kranenberg et al. [302] analyzed the formation of liquid crystalline L_α phase, and interdigitated $L_{\beta I}$ and non-interdigitated L_β gel phases in lipid bilayers (Fig. 19). The authors found that although $L_{\beta I}$ is predicted only for double-tailed lipids, single-tailed lipids may also form $L_{\beta I}$ phase for sufficiently large head-head repulsion. Li and coworkers [329] devised a MARTINI-like DPD parameterization scheme with 4-1 mapping for phospholipids and analyzed bilayer characteristics such as bending rigidity, flipflops and rupture behavior.

Applications of DPD in studying dynamics of membrane-protein systems was reviewed by Guigas et al. [330] Proteins that are embedded in the cell membrane are usually modelled in DPD [331–334] as rod-like or cylindrical objects made of mainly two types of beads, hydrophobic and hydrophilic. The *hydrophobic mismatch* of the proteins along the bilayer thickness is the important factor that keeps them embedded within the membrane, which controls protein-induced perturbation quantified by the bilayer hydrophobic thickness profile around protein and the protein tilt angle. Venturoli et al. [331] first applied DPD to analyze the effects of different protein hydrophobic lengths and sizes, and found that the bilayer response the large hydrophobic mismatch depends on the size of the protein. Guigas et al.

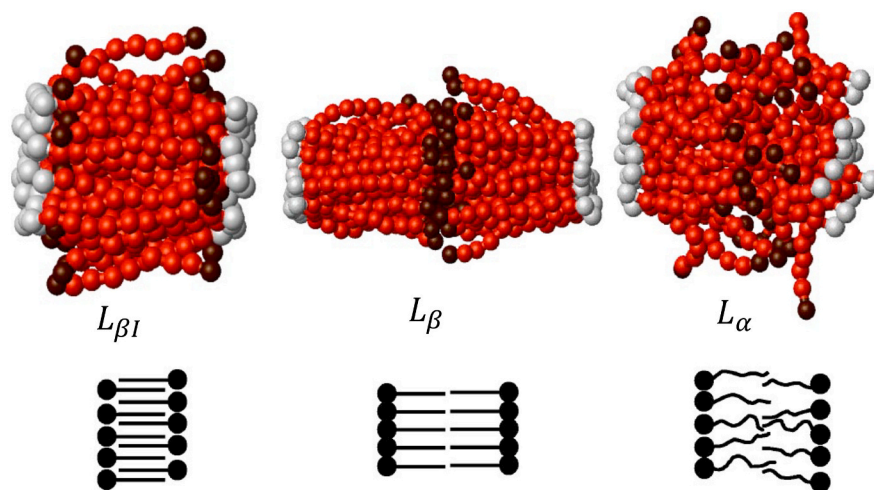


Fig. 19. The $L_{\beta I}$, L_β and L_α phases in lipid bilayers. The head groups are represented by grey beads, tails in red beads and end tail beads in darker color. Adapted from Kranenberg et al., ref. [302], with permission, of API publishing. (For interpretation of the references to color in this figure legend, the reader is referred to the web version of this article.)

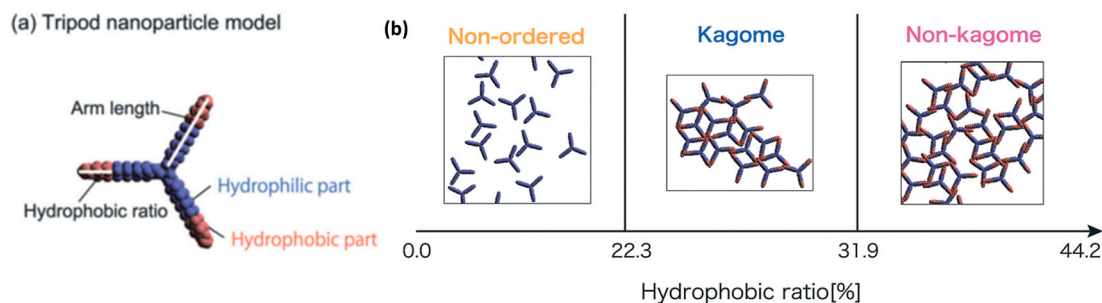


Fig. 20. (a) Tripod nanoparticle model. (b) Aggregate structures of tripod NPs as a function of the hydrophobic ratio. Reproduced from Sazali et al., ref. [340] with permission from the Royal Society of Chemistry. (For interpretation of the references to color in this figure legend, the reader is referred to the web version of this article.)

[332,334] showed that the hydrophobic mismatch induces protein clustering in the membrane, but it influences protein mobility within the membrane only slightly. The protein diffusion coefficients were found to scale with the protein size R_p as $1/R_p^2$, above a critical size. de Mayer et al. [335] calculated the potential of mean force of the lipid-mediated interaction between transmembrane proteins and found that the protein-protein interaction is regulated by hydrophobic forces, which depends on the hydrophobic mismatch as well as the bilayer characteristics. DPD was applied to study the reverse micelle protein extraction of papain, in systems containing water, surfactant CTAB and organic solvents [336]. The simulations showed that papain can be extracted with an efficiency of 76%.

5.5. Nanoparticle systems

5.5.1. Nanoparticle suspensions

DPD offers perhaps the most feasible way to simulate solid particles of the nanoscale, which enabled studies of systems such as colloidal suspensions, polymer nanocomposites (PNCs) and other nanoparticle systems. Simulation of nanoparticle (NP) systems is still beyond the reach of atomistic MD simulations with reasonable computer resources. In DPD, solid particles can be modelled by rigid objects consisting of several beads that are frozen or by groups of beads that are connected with very strong nearest neighbor bonds. Original works of Hoogerbrugge and Koelman studied rheology of suspensions of solid particles [15–16] created by *local freezing* of the fluid. The reduced viscosity of suspensions of solid spheres at high shear rate, was found to be in excellent agreement with experiments. Energy conserving DPD was applied to heat conduction in nanoparticle suspensions (nanofluids) by He and Qiao [337] who found that heat conduction is not affected by Brownian motion of nanoparticles. Effects of Al_2O_3 nanoparticles on heat transfer in Al_2O_3 -water nanofluids was studied by Abu-Nada [338] who predicted an enhancement of heat transfer with addition of NPs. Li and Drazer [339] measured mobility and diffusion coefficient of colloidal particles using DPD and found very good agreement with experiments.

Anisotropic nanoparticles such as nanorods, tripods, octapods etc. can self-assemble into different patterns, leading to materials with varying mechanical, optical, electrical and thermal properties. Sazali et al. [340] studied self-assembly of amphiphilic tripod nanoparticles (Fig. 20a) in water, which consist of three amphiphilic arms with interior hydrophilic and exterior hydrophobic blocks. The armlength was varied from 2.1 to 4.5 nm, while the percentage of hydrophobic beads in the NP, defined as the hydrophobic ratio as varied from 0 to 44%. The simulations showed formation of non-ordered, linear, *kagome* and *non-kagome* structures, at varying hydrophobic ratio and arm length (Fig. 20b). Elliot and Windle [341] used DPD to examine assemblies of spherical and non-spherical (cubic) filler particles used in manufacturing polymer-composite, and observed entropy-driven demixing in the sphere-cube mixtures. Colloidal particle adsorption on surfaces grafted by polymers was studied by Gibson et al. [342], who

reported that the adsorption is reduced by increasing the size and density of the polymers. Phase separation and domain growth of binary mixture of fluids containing nanospheres were studied by Laradji and Hore [343], who found that addition of NPs slows down the domain growth.

5.5.2. Nanoparticle composites

In polymer nanocomposites, NPs can enhance the mechanical and optical properties, the NP-NP and NP-polymer interactions are of critical importance in the aggregation and phase behavior. DPD simulations were performed [344] to study the effects of spherical nanoparticles in the lamellar phase separation of diblock copolymers. It was found that NPs affect the phase separation, forming a new bicontinuous morphology, consistent with experimental results. The cooperative self-assembly of NPs [345] and mixtures of NPs [346] in lamellar and hexagonal diblock copolymer phases were studied using DPD, elucidating the molecular details of the NP-NP and NP-polymer interactions that cause NP aggregation. NP aggregation in aqueous copolymer phases was also studied using DPD; while Chen et al. [347] analyzed conditions of stabilization of gold nanoparticles by PEO-PPO-PEO block copolymer micelles, Chen and Ruckenstein [348] investigated NP aggregation in block copolymer bilayers. The presence of NPs affects the viscoelastic behavior of diblock copolymer phases as observed in the nanorod-BCP composites [349]. High concentrations of nanorods induced reorientation and morphological changes of the copolymer phase at high shear. Spaeth et al. [350] studied the *Flash Nano-Precipitation process*, that is used to prepare NPs consisting of aggregated solute particles ‘protected’ by diblock copolymers wrapped over it. They developed and compared implicit solvent BD and explicit solvent DPD models of the process that involves self-assembly of block copolymer-NP systems in a solvent and concluded that BD simulations may become inappropriate when hydrodynamic interactions are important.

DPD simulations of Bianchino et al. [351] of oleic acid (OA) coated NPs embedded in polymethyl methacrylate (PMMA) matrix, showed that the NPs segregate into the OA-rich regions at low OA concentrations, but become homogeneously distributed in the region at high concentrations of the surfactant. Huang et al. [352] studied hydrophobic NP aggregation in the presence of double hydrophilic block copolymers (DHBC) that are used in controlled aggregation/crystallization of inorganic particles. Here, NPs repel solvent strongly and form aggregates in the pure solvent, but interact with polymer blocks favorably and differently, leading to change in aggregation states and dissolution as the polymer concentration is increased. Ma and coworkers [353] designed a new type of polymer-NP substrate that can differentiate between cancer and normal cells by performing DPD simulations of the substrate interaction with representative lipid vesicles. Here, vesicles representing cancer cells were distinguished by a high content of receptor lipids and the study showed that NP uptake of cancer cell type vesicles from the substrate could be much higher.

Reaction-limited cluster aggregation (RLCA) of NPs in presence of

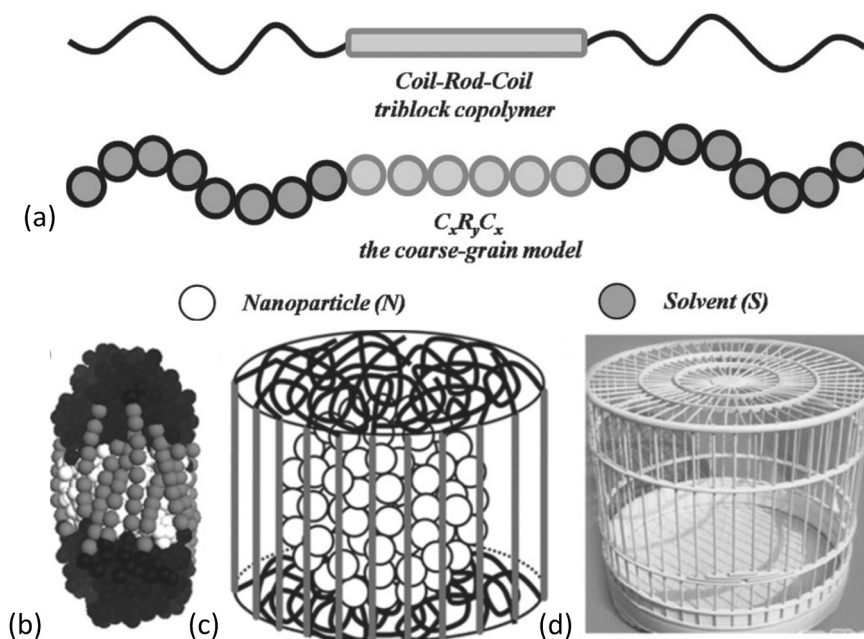


Fig. 21. (a) The coil-rod-coil triblock polymer model. (b-c) The cage-like structures formed by polymer and NPs resembling real bird cage. Adapted from Zhou et al., ref. [356] with permission of John Wiley and Sons.

diblock copolymers that form lamellar phase was modelled by introducing a soft aggregation potential by Magee and Sliperstein [354], who observed demixing of the NPs and the polymer phase in the strong aggregation limit. The presence of nanorods in polymer melts leads to increase in entanglements. DPD simulations [355] showed a decrease in the topological entanglement length and consequently an increase in number of entanglements in polymer-nanocomposites containing nanorods, in comparison with polymer melts. An interesting category of PNCs is the coil-rod-coil triblock polymer-nanocomposites (Fig. 21a), DPD simulations have showed that such systems self-assemble in a solvent to form nanocages, in which the NPs are trapped in a cage-like morphology that resembles a real bird cage (Fig. 21b-d), which can be potentially used in drug delivery and other applications such as nano-reactors [356]. Ma et al. [357] investigated self-assembly of polymer tethered NPs, giant amphiphiles formed by hydrophilic NPs tethered with hydrophobic polymers and hydrophobic NPs tethered with amphiphilic copolymers, and reported various assemblies such as rod-like segmented micelles, nanowire, nano-ring and nanoclusters. Yang et al. [358] studied self-assembly of NPs and amphiphilic diblock copolymers and reported NP encapsulated morphologies of spherical, rod-like, disk-like and branched micelles. Nair et al. [359] studied polymer-grafted NPs at oil-water interface at different salinity in the context of *polymer flooding* method of oil recovery and found that the equilibrium location of the grafted NPs depends on the salinity and grafting density. Vo and Papavassiliou [360] investigated the effect of shearing force on physisorption of PVP on carbon nanoparticles of various shapes and showed that the polymer may remain adsorbed, shear-affected or desorbed depending on the strength of the shear rate.

PEMs are used in fuel cells as the membrane separator between the anode and cathode compartments, and NPs are added to increase efficiency and chemical and thermal stability. NP-mediated polyelectrolyte self-assembly was investigated by Kobayashi and Arai [361], in which hydrophilic, hydrophobic and Janus NPs were studied. Water diffusion was found to slow down with the presence of hydrophilic NPs which tend to associate with water particles, while the diffusion coefficient is also reduced with the increasing number NPs.

5.5.3. Interactions of NP with polymer brushes

NP interaction and aggregation within PBs in a solvent depend on the

solvent quality and NP-polymer interactions. Polymer-insoluble NPs were observed to organize at the PB-solvent interface being repelled from the denser PB interior [362]. Aggregation of nanoparticles can be controlled by grafting polymers over them, as the steric interactions between the grafted polymers lead to repulsion between the NPs. Self-assembly of polymer-grafted nanorods, with different polymer length and grafting density was analyzed by Khani et al. [363], who found that it is more difficult to prevent aggregation of nanorods of high aspect ratio by polymer-grafting compared to spherical NPs due to entropic reasons. The aggregation was prevented only with long-enough chains at high grafting density. Nguyen et al. [364] investigated tribological properties PB-NP systems by performing DPD simulations of nano-bearings consisting of grafted NPs between two polymer-grafted surface. The nano-bearings help with the poor mechanical stability of the brushes, by reducing the sliding contacts between the PBs while shearing.

Free energy landscapes of NP-PB interactions were calculated by Cheng et al. [259] by devising the original Ghost Tweezer's (GT) method which emulates force measurements by optical or magnetic tweezers in experiments. In GT method, the NP is pinned at a position by its identical 'ghost' twin by weak harmonic potentials, and the total force on the NP at this position by the surroundings is measured. The potential of mean force or the free energy landscape of NP-PB interaction, can be calculated by integrating the force profile thus obtained, as the mechanical work needed to bring the NP to PB from the bulk. The authors showed that the free energy of NP-PB interaction is governed by the interplay of polymer configurational entropic and enthalpic attractive forces between NP and PB. Depending on solvent quality and NP-polymer interactions, this interplay can lead to repulsion of NPs from PB, as well as adsorption at PB surface and immersion into the PB interior.

Santo et al. [261–262], investigated using DPD simulations, the chromatographic separation of ligand-grafted functionalized NPs with different surface properties. By the conventional chromatography techniques, NPs may be separated according to their shape and size, but such techniques cannot separate NPs by the surface chemistry, such as degree of hydrophobicity. Ideally, this is possible if there exists a critical point for NP adsorption, where entropic and enthalpic contribution to the NP-PB interaction balances so that NP elution through the PB grafted channel is size-independent but depends only on the critical point that is

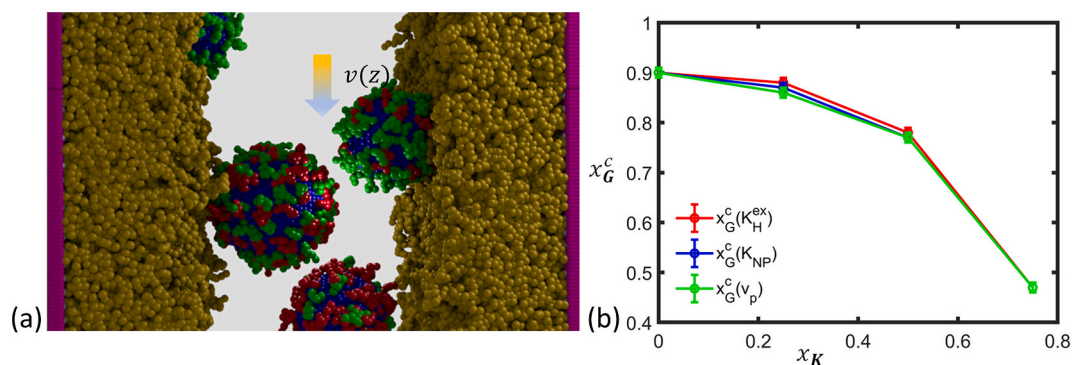


Fig. 22. (a) Functionalized NPs (blue) of different surface chemistry, characterized by the fraction of hydrophilic ligands (red) moving in polymer-grafted column (polymer-yellow, substrate -indigo, hydrophobic ligands green). (b) The critical solvent composition of NP adsorption obtained from the simulations as a function of NP hydrophilicity x_K . Adapted from Santo et al., ref. [262], with permission Copyright 2019, American Chemical Society. (For interpretation of the references to color in this figure legend, the reader is referred to the web version of this article.)

function of the NP surface chemistry. Such chromatographic separation of NP, called interaction nanoparticle chromatography (INPC), is similar to interaction mode in polymer chromatography [365]. In these works, the authors performed extensive DPD simulations to estimate the energetics of interaction of NPs with PB-grafted walls (Fig. 22a) as a function of NP size, NP surface chemistry, PB grafting density, solvent type and solvent quality. The solvent quality in the simulations was varied by changing composition of a binary solvent containing good and bad components, while the NP hydrophilicity was varied by changing the fraction of hydrophilic ligands grafted on the NP (Fig. 22a). The free energy landscapes of NP-PB interactions were calculated, which allowed the calculation of the thermodynamic Henry constants of adsorption, the partition coefficient, the mean NP velocity under a Poiseuille-like solvent flow, and isocratic and gradient elution time distributions. The study observed critical conditions of size-independent NP elution as a function of NP hydrophilicity (Fig. 22b) and suggested that NPs can be separated according to their surface chemistry in the gradient mode of chromatography near the critical point of adsorption. Burgess et al. [366] performed DPD simulations of flow of bare and ligand-functionalized NPs through polymer-grafted channels and analyzed the deviation of the mean NP velocity from the mean solvent velocity as a function of channel width. The ratio of the mean NP to solvent velocities was found to scale consistent with experimental results as the channel width decreased.

5.5.4. NP-lipid membrane interactions

Understanding NP interactions with cell membranes is important in

the biomedical applications such as targeted drug delivery. Key processes include NP targeting and internalization via processes such as endocytosis, NP cargo mechanisms, and NP toxicity to the cell. Several DPD works addressed nanoparticle interactions with cell membranes, recently reviewed by Tian et al. [367] DPD simulations of the kinetics of ligand-functionalized NP targeting on cell surfaces with high concentrations of receptors showed that the number of bound ligands on the surfaces grows as $1 - \exp(-t/\tau)$, where τ is the life-time that increases with ligand-receptor binding strength [368]. To understand the endocytosis of NPs by cell membranes, interaction of different shaped hydrophilic NPs with vesicles were studied using DPD by Yang and coworkers [369], who found that NP rotation at the vesicle contact plays a role in the NP internalization by the vesicles. The same group [370] investigated through experiments and DPD simulations, the internalization of ligand-charged NPs and found that multiply positively charged NPs can enter the cells more easily by *cooperative endocytosis* between the NPs. Liu et al. [371] also studied cooperative effects of NP aggregation in entering the biological cells.

Yue and Zhang [372] investigated cell membrane responses to NP adhesion, by performing *N-varied* DPD simulations of receptor-mediated interactions of ligand-coated NPs with lipid membranes and observed, NP-induced membrane rupture, NP adhesion, NP penetration and receptor-mediated endocytosis, depending on the membrane tension, NP size and ligand density. The same group also studied [177] membrane curvature generation and vesiculation due to self-assembly of anchored proteins, and interplay between nanoparticle wrapping and the aggregation of inner-anchored membrane proteins in receptor-

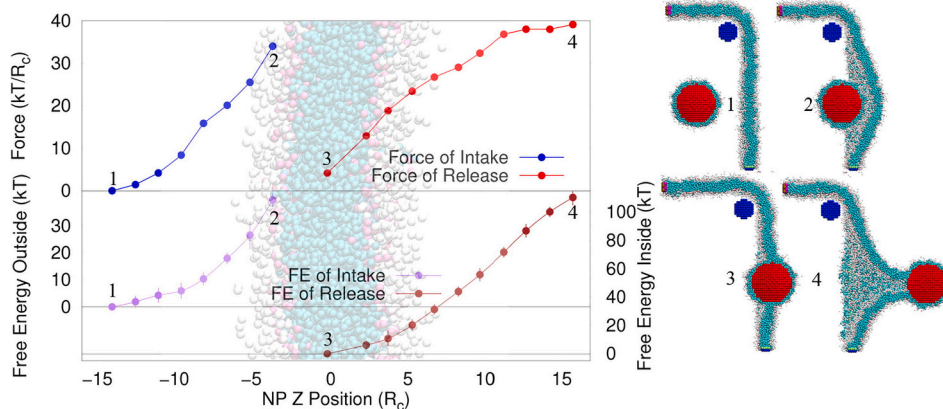


Fig. 23. Left: The free energy and force profiles of monolayer coated NP of 8 nm in diameter, across DMPC membrane as a function of NP position with respect to the membrane central plane. Right: configuration of the 'isotension' system during various stages of NP (red) translocation. Adapted from Burgess et al., ref. [374], with permission Copyright(2020) from Elsevier. (For interpretation of the references to color in this figure legend, the reader is referred to the web version of this article.)

mediated endocytosis. Burgess et al. [373] investigated the kinetics of hydrophobic NP-induced rupture of membranes at different tensions, and elucidated the mechanism of membrane rupture that occurs through heterogeneous nucleation of pores near the NP surface. The thermodynamics of the process is analyzed by introducing an effective contact angle at the NP-membrane contact and the results agreed well with the predictions of Derjaguin-Gutop theory. In a subsequent work from the group [374], the authors studied adhesion, intake and release of monolayer-coated hydrophobic NPs of various size, through DMPC bilayers (Fig. 23). In this work, a novel setup for performing DPD simulations at isotension conditions was introduced and the free energy landscape of the translocation process is elucidated by the Ghost-tweezers method [259]. The simulations showed that the free energy barrier for uptake increases as the NP size increases and becomes prohibitively high for NP of diameter 8 nm. For release, the simulation results and a dynamical analysis based on Fokker-Planck equation, predicted an optimal NP size for unforced translocation.

Nanosopic vesicles may be used as cargos for NPs in applications such as targeted drug-delivery, Yong et al. [375] showed that lipid vesicles moving by a flow on an adhesive surface, can pick up Janus NPs on the surface and drop them into trenches. The drug cargo liposomes are often PEG-ylated to prevent protein adsorption in the blood, however a recent DPD study [376] showed that mobility of PEGs on the liposome surface and PEG aggregation near the membrane can delay endocytosis, compared to PEGylated rigid NPs, that makes the cellular uptake inefficient. Membrane adhesion of lipid-polymer-hybrid (LPH) NPs, a novel class of targeted drug delivery systems, was studied by Li and Gorfe [377]. The ligand-tethered LPH was found to adhere following a first-order kinetics and was shown to be more efficient with enhancement of receptor-ligand interactions. Ines et al. [378] showed by DPD simulations that different patterns of self-assembled monolayers of immiscible surfactants on NPs can be formed by the mechanism of free energy minimization, that leads to different types of monolayer-patterned NPs, such as Cerberus, Neapolitan, Striped Janus, Alternating Stripes, and Spotted particles.

5.6. Other systems

This review cannot embrace the whole spectrum of DPD applications. Several other systems studied by DPD include phase separating immiscible liquids [379], graphene [380], caprolactam systems [381] and asphaltenes in crude oil [382]. Rheology of bubble suspensions has been studied using a hard-core DPD model [173]. Some of the works utilizing other forms of DPD are reviewed above in Section 3.

6. Concluding remarks

Dissipative particle dynamics is an efficient mesoscopic computational approach, applied to multifarious colloid and interfacial systems. The main advantage of DPD compared with other coarse-grained techniques is the computational efficiency and availability of various parameterization schemes that are customized for specific applications. DPD methods are widely used for predicting physico-chemical, mechanical, and transport properties of complex solutions, surfactant and polymeric systems, polyelectrolytes and biopolymers, lipid membranes, and nanoparticle systems. In this review, we were not able to embrace the whole spectrum of DPD applications, however, a substantially extensive overview of studies on various topics using the DPD method is presented.

DPD is most useful in studying polymeric systems. Several characteristics of dilute and semi-dilute polymer solutions such as excluded volume and hydrodynamic interactions, solvent effects and scaling laws, are well-described by DPD, while the method has been widely used study polymers in confined spaces as well, such as polymeric flow in nano channel and polymer translocation through a pore. For studying concentrated polymer solutions melts, additional potentials or methods

to capture entanglement effects were developed. DPD has been effectively applied to investigate mesoscopic phases of diblock copolymer melts and aqueous solutions as well as polymer brushes. With specially developed models capable of describing interactions such as complexation and hydrogen bonding, structural features of biopolymers such as DNA and proteins as well as rheology of metal-complexed polymer solutions were studied. DPD has been extensively applied to study the behavior of polyelectrolyte solutions and membranes; PE solution rheology, PE-surfactant and PE-surface interactions and PE flow through channels were studied. To study PEM morphology and transport behavior, the DPD method has been mostly used, with novel models developed for studying proton transport and effects of metal-complexation.

Extensive literature of DPD studies of surfactant systems exists pertaining to both industrial and biological applications; DPD is extremely useful in describing surfactant self-assembly and phase behavior in aqueous solutions, such as formation of micellar, cylindrical, bilayer, hexagonal and other phases. Behavior of surfactant monolayers at liquid-liquid interfaces was analyzed in several works, while novel models developed for investigating monolayers at gas-liquid interfaces. Critical micelle concentrations several surfactants were reproduced by DPD modelling with the progress over the years. The structural and mechanical characteristics of phospholipid membranes were also studied by DPD. The DPD method has been most widely employed to study nanoparticle systems that are used in various applications, such as nanoparticle suspensions, polymer nanocomposites, and nanoparticle-polymer brush and nanoparticle-lipid membranes systems. Self-assembly of NPs of several types and shapes and the resulting supramolecular structures, adsorption of NPs on surfaces and their correlations between NP aggregation and the NP structural features, were investigated in many works. Other studies include NP aggregation in a polymer matrix in PNCs as well as NP flow in PB-grafted channels. NP-cell membrane interactions were studied in many works in the context of drug delivery to cells.

DPD simulation methods are implemented in most common open-source software packages such as LAMMPS [383], ESPResSo [384] and DL-MESO [385], that can be used by non-experts. The recent HOOMD-blue package developed in the Glotzer lab [386] and the GALAMOST package [387] allow GPU-accelerated DPD simulations.

It is important to understand the limitations and deficiency of DPD methodology. Originally formulated as a momentum conserving, Galilean invariant coarse-grained method, DPD was explicated providing with a statistical mechanical base, numerical scheme and a parameterization procedure. The numerical schemes faced impediments arising from the velocity dependence of the forces, and several attempts to develop other efficient numerical schemes and thermostats were performed. DPD as originally formulated has several limitations, including the ineptitude to simulate vapor-liquid coexistence, which led to several alternate forms of DPD, SDDP, MDDP, FPM and DPDE. Another limitation is in simulating of solid-liquid interface, where slips occur when there is a fluid flow. The issues of low coarse-graining limits due to compressibility scaling with mapping number, and equal bead sizes and intracomponent parameters have been addressed with subsequent improvements on parameterization, but a completely rigorous parameterization scheme is still lacking. Incorporation of electrostatic interaction required finite charge distributions, instead of point charges, and the smeared charge distributions have been employed in various forms, including linear, Slater, Gaussian, and Bessel type distributions. Despite the aforementioned limitations, DPD remains as a highly versatile, efficient and constantly improving mesoscale simulation method.

Declaration of Competing Interest

The authors declare that they have no known competing financial interests or personal relationships that could have appeared to influence the work reported in this paper.

Acknowledgements

This work was supported in parts by NSF-CBET grants 1264702, 1510993, and 2040302.

References

- [1] Zimmerman MI, Porter JR, Ward MD, Singh S, Vithani N, Meller A, et al. SARS-CoV-2 simulations go exascale to predict dramatic spike opening and cryptic pockets across the proteome. *Nat Chem* 2021;13:651–9.
- [2] Nakano A, Kalia RK, Nomura K-I, Sharma A, Vashishta P, Shimojo F, et al. A divide-and-conquer/cellular-decomposition framework for million-to-billion atom simulations of chemical reactions. *Comput Mater Sci* 2007;38(4):642–52.
- [3] Groot RD. Applications of dissipative particle dynamics. In: Karttunen M, Lukkarinen A, Vattulainen I, editors. *Novel methods in soft matter simulations*. Berlin, Heidelberg: Springer Berlin Heidelberg; 2004. p. 5–38.
- [4] Groot RD, Warren PB. Dissipative particle dynamics: bridging the gap between atomistic and mesoscopic simulation. *J Chem Phys* 1997;107(11):4423–35.
- [5] Noid WG. Perspective: coarse-grained models for biomolecular systems. *J Chem Phys* 2013;139(9).
- [6] Reith D, Pütz M, Müller-Plathe F. Deriving effective mesoscale potentials from atomistic simulations. *J Comput Chem* 2003;24(13):1624–36.
- [7] Lyubartsev AP, Laaksonen A. Calculation of effective interaction potentials from radial distribution functions: a reverse Monte Carlo approach. *Phys Rev E* 1995;52(4):3730–7.
- [8] Izvekov S, Voth GA. A multiscale coarse-graining method for biomolecular systems. *J Phys Chem B* 2005;109(7):2469–73.
- [9] Shell MS. The relative entropy is fundamental to multiscale and inverse thermodynamic problems. *J Chem Phys* 2008;129(14):144108.
- [10] Schweizer KS. Microscopic theory of the dynamics of polymeric liquids - general formulation of a mode mode-coupling approach. *J Chem Phys* 1989;91(9):5802–21.
- [11] Mori H. Transport, collective motion, and Brownian motion. *Prog Theor Phys* 1965;33(3):423–55.
- [12] Donev A, Vanden-Eijnden E. Dynamic density functional theory with hydrodynamic interactions and fluctuations. *J Chem Phys* ;140(23).
- [13] Landau LD, Lifshitz EM. *Fluid mechanics*. New York: Pergamon Press; 1987.
- [14] Donev A, Fai TG, Vanden-Eijnden E. A reversible mesoscopic model of diffusion in liquids: from giant fluctuations to Fick's law. *J Stat Mech Theory Exp* 2014;2014:P04004.
- [15] Hoogerbrugge PJ, Koelman JMVA. Simulating microscopic hydrodynamic phenomena with dissipative particle dynamics. *Europhys Lett* 1992;19(3):155.
- [16] Koelman JMVA, Hoogerbrugge PJ. Dynamic simulations of hard-sphere suspensions under steady shear. *Europhys Lett* 1993;21(3):363.
- [17] Español P, Warren P. Statistical mechanics of dissipative particle dynamics. *Europhys Lett* ;30(4):191.
- [18] Erban R. From molecular dynamics to Brownian dynamics ;470(2167):20140036.
- [19] Marrink SJ, Risselada HJ, Yefimov S, Tieleman DP, de Vries AH. The MARTINI force field: coarse grained model for biomolecular simulations. *J Phys Chem B* 2007;111(27):7812–24.
- [20] Ladd AJC. Short-time motion of colloidal particles: numerical simulation via a fluctuating lattice-Boltzmann equation. *Phys Rev Lett* 1993;70(9):1339–42.
- [21] Frisch U, Hasslacher B, Pomeau Y. Lattice-gas automata for the Navier-stokes equation. *Phys Rev Lett* 1986;56(14):1505–8.
- [22] Anderson RL, Bray DJ, Ferrante AS, Noro MG, Stott IP, Warren PB. Dissipative particle dynamics: systematic parametrization using water-octanol partition coefficients. *J Chem Phys* 2017;147(9):094503.
- [23] Travis KP, Bankhead M, Good K, Owens SL. New parametrization method for dissipative particle dynamics. *J Chem Phys* 2007;127(1):014109.
- [24] Saathoff J. Effectively parameterizing dissipative particle dynamics using COSMO-SAC: a partition coefficient study. *J Chem Phys* 2018;148(15):154102.
- [25] Minkara MS, Hembree RH, Jamadagni SN, Ghobadi AF, Eike DM, Siepmann JI. A new equation of state for homo-polymers in dissipative particle dynamics. *J Chem Phys* 2019;150(12):124104.
- [26] Pivkin IV, Caswell B, Karniadakis GE. Dissipative particle dynamics. In: Lipkowitz KB, editor. *Rev. Comput. Chem.*; 2010.
- [27] Moendarbary E, Ng TY, Zangeneh M. Dissipative particle dynamics in soft matter and polymeric applications — a review. *Int J Appl Mech* 2010;2:161–90.
- [28] Español P, Warren PB. Perspective: dissipative particle dynamics. *J Chem Phys* 2017;146(15):150901.
- [29] Warren PB. Vapor-liquid coexistence in many-body dissipative particle dynamics. *Phys Rev E* 2003;68(6):066702.
- [30] Warren PB. Hydrodynamic bubble coarsening in off-critical vapor-liquid phase separation. *Phys Rev Lett* 2001;87(22):225702.
- [31] Español P. Fluid particle dynamics: a synthesis of dissipative particle dynamics and smoothed particle dynamics. *Europhys Lett* ;39(6):605.
- [32] Español P, Revenga M. Smoothed dissipative particle dynamics. *Phys Rev E* 2003;67(2):026705.
- [33] Español P. Fluid particle model. *Phys Rev E* 1998;57(3):2930–48.
- [34] Avalos JB, Mackie AD. Dissipative particle dynamics with energy conservation. *Europhys Lett* 1997;40(2):141–6.
- [35] Avalos JB, Mackie AD. Dynamic and transport properties of dissipative particle dynamics with energy conservation. *J Chem Phys* 1999;111(11):5267–76.
- [36] Español P. Dissipative particle dynamics with energy conservation. *Europhys Lett* ;40(6):631.
- [37] Ripoll M, Español P, Ernst MH. Dissipative particle dynamics with energy conservation: heat conduction. *Int J Mod Phys C* 1998;09(08):1329–38.
- [38] Lásal Martin, Brennan John K, Smith WR. Mesoscale simulation of polymer reaction equilibrium: combining dissipative particle dynamics with reaction ensemble Monte Carlo. I. Polydispersed polymer systems. *J Chem Phys* 2006;125(16):164905.
- [39] Lásal M, Brennan JK, Smith WR. Mesoscale simulation of polymer reaction equilibrium: combining dissipative particle dynamics with reaction ensemble Monte Carlo. II. Supramolecular diblock copolymers. *J Chem Phys* 2009;130(10):104902.
- [40] Lásal M, Larentzos JP, Sellers MS, Schweigert IV, Brennan JK. Dissipative particle dynamics with reactions: application to RDX decomposition. *J Chem Phys* 2019;151(11):114112.
- [41] Groot RD, Rabone KL. Mesoscopic simulation of cell membrane damage, morphology change and rupture by nonionic surfactants. *Biophys J* 2001;81(2):725–36.
- [42] Lee M-T, Mao R, Vishnyakov A, Neimark AV. Parametrization of chain molecules in dissipative particle dynamics. *J Phys Chem B* 2016;120(22):4980–91.
- [43] Kacar G, Peters EA, de With G. Mesoscopic simulations for the molecular and network structure of a thermoset polymer. *Soft Matter* 2013;9(24):5785–93.
- [44] Kacar G, Peters EA, With GD. A generalized method for parameterization of dissipative particle dynamics for variable bead volumes. *Europhys Lett* 2013;102(4):40009.
- [45] Groot RD. Electrostatic interactions in dissipative particle dynamics—simulation of polyelectrolytes and anionic surfactants. *J Chem Phys* 2003;118(24):11265–77.
- [46] Gonzalez-Melchor M, Mayoral E, Velazquez ME, Alejandro J. Electrostatic interactions in dissipative particle dynamics using the Ewald sums. *J Chem Phys* 2006;125(22).
- [47] Warren PB, Vlasov A, Anton L, Masters AJ. Screening properties of Gaussian electrolyte models, with application to dissipative particle dynamics. *J Chem Phys* 2013;138(20):204907.
- [48] Warren PB, Vlasov A. Screening properties of four mesoscale smoothed charge models, with application to dissipative particle dynamics. *J Chem Phys* 2014;140(8).
- [49] Eslami H, Khani M, Müller-Plathe F. Gaussian charge distributions for incorporation of electrostatic interactions in dissipative particle dynamics: application to self-assembly of surfactants. *J Chem Theory Comput* 2019;15:4197–207.
- [50] Forrest BM, Suter UW. Accelerated equilibration of polymer melts by time-coarse-graining. *J Chem Phys* 1995;102(18):7256–66.
- [51] Liu M, Meakin P, Huang H. Dissipative particle dynamics with attractive and repulsive particle-particle interactions. *Phys Fluids* 2006;18(1):017101.
- [52] Allen MP, Tildesley DJ. *Computer simulation of liquids*. New York: Clarendon Press; 1987.
- [53] Marsh CA, Yeomans JM. Dissipative particle dynamics: the equilibrium for finite time steps. *Europhys Lett* 1997;37(8):511.
- [54] Nikunen P, Karttunen M, Vattulainen I. How would you integrate the equations of motion in dissipative particle dynamics simulations? *Comput Phys Commun* 2003;153(3):407–23.
- [55] Vattulainen I, Karttunen M, Besold G, Polson JM. Integration schemes for dissipative particle dynamics simulations: from softly interacting systems towards hybrid models. *J Chem Phys* 2002;116(10):3967–79.
- [56] Allen MP. Configurational temperature in membrane simulations using dissipative particle dynamics. *J Phys Chem B* 2006;110(8):3823–30.
- [57] Novik KE, Coveney PV. Finite-difference methods for simulation models incorporating nonconservative forces. *J Chem Phys* 1998;109(18):7667–77.
- [58] Pagonabarraga I, Hagen MHJ, Frenkel D. Self-consistent dissipative particle dynamics algorithm. *Europhys Lett* 1998;42(4):377.
- [59] Gibson JB, Chen K, Chynoweth S. The equilibrium of a velocity-verlet type algorithm for DPD with finite time steps. *Int J Mod Phys C* 1999;10(01):241–61.
- [60] Otter WKD, Clarke JHR. A new algorithm for dissipative particle dynamics. *Europhys Lett* 2001;53(4):426.
- [61] Shardlow T. Splitting for dissipative particle dynamics. *SIAM J Sci Comput* 2003;24(4):1267–16.
- [62] Serrano M, De Fabritiis G, Español P, Coveney PV. A stochastic trotter integration scheme for dissipative particle dynamics. *Math Comput Simul* 2006;72(2):190–4.
- [63] Thalmann F, Farago J. Trotter derivation of algorithms for Brownian and dissipative particle dynamics. *J Chem Phys* 2007;127(12):124109.
- [64] Lowe CP. An alternative approach to dissipative particle dynamics. *Europhys Lett* 1999;47(2):145.
- [65] Symeonidis V, Karniadakis GE. A family of time-staggered schemes for integrating hybrid DPD models for polymers: algorithms and applications. *J Comput Phys* 2006;218(1):82–101.
- [66] Andersen HC. Molecular dynamics simulations at constant pressure and/or temperature. *J Chem Phys* 1980;72(4):2384–93.
- [67] Symeonidis V, Karniadakis GE, Caswell B. Schmidt number effects in dissipative particle dynamics simulation of polymers. *J Chem Phys* 2006;125(18):184902.
- [68] Peters EA. Elimination of time step effects in DPD. *Europhys Lett* 2004;66(3):311.
- [69] Stoyanov SD, Groot RD. From molecular dynamics to hydrodynamics: a novel Galilean invariant thermostat. *J Chem Phys* 2005;122(11):114112.
- [70] Leimkuhler B, Shang X. Pairwise adaptive thermostats for improved accuracy and stability in dissipative particle dynamics. *J Comput Phys* 2016;324:174–93.

- [71] Junghans C, Praprotnik M, Kremer K. Transport properties controlled by a thermostat: an extended dissipative particle dynamics thermostat. *Soft Matter* 2008;4(1):156–61.
- [72] Qiao R, He P. Mapping of dissipative particle dynamics in fluctuating hydrodynamics simulations. *J Chem Phys* 2008;128(12):126101.
- [73] Flekkøy EG, Coveney PV. From molecular dynamics to dissipative particle dynamics. *Phys Rev Lett* 1999;83(9):1775–8.
- [74] Flekkøy EG, Coveney PV, De Fabritiis G. Foundations of dissipative particle dynamics. *Phys Rev E* 2000;62(2):2140–57.
- [75] Serrano M, Español P. Thermodynamically consistent mesoscopic fluid particle model. *Phys Rev E* 2001;64(4):046115.
- [76] Öttinger HC, Grmela M. Dynamics and thermodynamics of complex fluids. II. Illustrations of a general formalism. *Phys. Rev. E* 1997;56(6):6633–55.
- [77] Serrano M. Comparison between smoothed dissipative particle dynamics and Voronoi fluid particle model in a shear stationary flow. *Phys A Stat Mech Appl* 2006;362(1):204–9.
- [78] Kulkarni PM, Fu C-C, Shell MS, Leal LG. Multiscale modeling with smoothed dissipative particle dynamics. *J Chem Phys* 2013;138(23).
- [79] Litvinov S, Xie Q, Hu X, Adams N, Ellero M. Simulation of individual polymer chains and polymer solutions with smoothed dissipative particle dynamics. *Fluids* ;1(1).
- [80] Bian X, Litvinov S, Qian R, Ellero M, Adams NA. Multiscale modeling of particle in suspension with smoothed dissipative particle dynamics. *Phys Fluids* 2012;24(1).
- [81] Thieulot C, Janssen L, Espanol P. Smoothed particle hydrodynamics model for phase separating fluid mixtures. I. General equations. *Phys Rev E* ;72(1).
- [82] Katanov D, Gompper G, Fedosov DA. Microvascular blood flow resistance: role of red blood cell migration and dispersion. *Microvasc Res* 2015;99:57–66.
- [83] Müller K, Fedosov DA, Gompper G. Margination of micro- and nano-particles in blood flow and its effect on drug delivery. *Sci Rep* 2014;4:4871.
- [84] Vazquez-Quesada A, Ellero M, Espanol P. Smoothed particle hydrodynamic model for viscoelastic fluids with thermal fluctuations. *Phys Rev E* ;79(5).
- [85] Petsev ND, Leal LG, Shell MS. Hybrid molecular-continuum simulations using smoothed dissipative particle dynamics. *J Chem Phys* 2015;142(4).
- [86] Müller K, Fedosov DA, Gompper G. Smoothed dissipative particle dynamics with angular momentum conservation. *J Comput Phys* 2015;281:301–15.
- [87] Boryczko K, Dzwiniel WA, Yuen D. Dynamical clustering of red blood cells in capillary vessels. *J Mol Model* 2003;9(1):16–33.
- [88] Boryczko K, Dzwiniel W, Yuen DA. Modeling fibrin aggregation in blood flow with discrete-particles. *Comput Methods Programs Biomed* 2004;75(3):181–94.
- [89] Dzwiniel W, Yuen DA. Mesoscopic dispersion of colloidal agglomerate in a complex fluid modelled by a hybrid fluid–particle model. *J Colloid Interface Sci* 2002;247(2):463–80.
- [90] Krzysztof B, Witold D, Yuen DA. Parallel implementation of the fluid particle model for simulating complex fluids in the mesoscale. *Concurr Comput Pract Exp* 2002;14(2):137–61.
- [91] Pagonabarraga I, Frenkel D. Dissipative particle dynamics for interacting systems. *J Chem Phys* 2001;115(11):5015–26.
- [92] Trofimov SY, Nies ELF, Michels MAJ. Thermodynamic consistency in dissipative particle dynamics simulations of strongly nonideal liquids and liquid mixtures. *J Chem Phys* 2002;117(20):9383–94.
- [93] Ghoufi A, Malfreyt P. Mesoscale modeling of the water liquid-vapor interface: a surface tension calculation. *Phys Rev E* 2011;83(5):051601.
- [94] Tiwari A, Abraham J. Dissipative-particle-dynamics model for two-phase flows. *Phys Rev E* 2006;74(5):056701.
- [95] Arienti M, Pan W, Li X, Karniadakis G. Many-body dissipative particle dynamics simulation of liquid/vapor and liquid/solid interactions. *J Chem Phys* ;134(20).
- [96] Ghoufi A, Malfreyt P. Calculation of the surface tension from multibody dissipative particle dynamics and Monte Carlo methods. *Phys Rev E* ;82(1).
- [97] Atashafrooz M, Mehdipour M. Many-body dissipative particle dynamics simulation of liquid-vapor coexisting curve in sodium. *J Chem Eng Data* 2016;61(10):3659–64.
- [98] Ghoufi A, Emile J, Malfreyt P. Recent advances in many body dissipative particles dynamics simulations of liquid-vapor interfaces. *Eur Phys J E* ;36(1).
- [99] Espanol P, Serrano M, Pagonabarraga I, Zuniga I. Energy-conserving coarse-graining of complex molecules. *Soft Matter* 2016;12(21):4821–37.
- [100] Bonet Avalos J, Lísal M, Larentzos JP, Mackie AD, Brennan JK. Generalized energy-conserving dissipative particle dynamics revisited: insight from the thermodynamics of the mesoparticle leading to an alternative heat flow model. *Phys Rev E* 2021;103(6):062128.
- [101] Willemsen SM, Hoefsloot HCJ, Visser DC, Hamersma PJ, Iedema PD. Modelling phase change with dissipative particle dynamics using a consistent boundary condition. *J Comput Phys* 2000;162(2):385–94.
- [102] Willemsen SM, Hoefsloot HCJ, Iedema PD. Mesoscopic simulation of polymers in fluid dynamics problems. *J Stat Phys* 2002;107(1):53–65.
- [103] Qiao R, He P. Simulation of heat conduction in nanocomposite using energy-conserving dissipative particle dynamics. *Mol Simul* 2007;33(8):677–83.
- [104] Yamada T, Kumar A, Asako Y, Gregory OJ, Faghri M. Forced convection heat transfer simulation using dissipative particle dynamics. *Numer Heat Transf A Appl* 2011;60(8):651–65.
- [105] Maillet JB, Bourasseau E, Desbiens N, Vallverdu G, Stoltz G. Mesoscopic simulations of shock-to-detonation transition in reactive liquid high explosive. *Epl* 2011;96(6).
- [106] Ganzemüller GC, Hiermaier S, Steinhauser MO. Shock-wave induced damage in lipid bilayers: a dissipative particle dynamics simulation study. *Soft Matter* 2011;7(9):4307–17.
- [107] Chaudhri A, Lukes JR. Multicomponent energy conserving dissipative particle dynamics: a general framework for mesoscopic heat transfer applications. *J Heat Transf* 2009;131(3).
- [108] Pastewka L, Kauzlaric D, Greiner A, Korvink JG. Thermostat with a local heat-bath coupling for exact energy conservation in dissipative particle dynamics. *Phys Rev E* 2006;73(3):037701.
- [109] Jakobsen AF. Constant-pressure and constant-surface tension simulations in dissipative particle dynamics. *J Chem Phys* 2005;122(12):124901.
- [110] Trofimov SY, Nies ELF, Michels MAJ. Constant-pressure simulations with dissipative particle dynamics. *J Chem Phys* 2005;123(14):144102.
- [111] Lísal M, Brennan JK, Avalos JB. Dissipative particle dynamics at isothermal, isobaric, isoenergetic, and isoenthalpic conditions using Shardlow-like splitting algorithms. *J Chem Phys* 2011;135(20).
- [112] Rekvig L, Hafskjold B, Smit B. Molecular simulations of surface forces and film rupture in oil/water/surfactant systems. *Langmuir* 2004;20(26):11583–93.
- [113] Goujon F, Malfreyt P, Tildesley Dominic J. Dissipative particle dynamics simulations in the grand canonical ensemble: applications to polymer brushes. *Chem Phys Chem* 2004;5(4):457–64.
- [114] Cieplak M, Koplik J, Banavar JR. Boundary conditions at a fluid-solid interface. *Phys Rev Lett* 2001;86(5):803–6.
- [115] Lees AW, Edwards SF. The computer study of transport processes under extreme conditions. *J Phys C Solid State Phys* 1972;5(15):1921.
- [116] Backer JA, Lowe CP, Hoefsloot HCJ, Iedema PD. Poiseuille flow to measure the viscosity of particle model fluids. *J Chem Phys* 2005;122(15):154503.
- [117] Revenga M, Zúñiga I, Espanol P. Boundary conditions in dissipative particle dynamics. *Comput Phys Commun* 1999;121-122:309–11.
- [118] Revenga M, Zúñiga I, Espanol P, Pagonabarraga I. Boundary models in DPD. *Int J Mod Phys C* 1998;09(08):1319–28.
- [119] Chen S, Phan-Thien N, Khoo BC, Fan XJ. Flow around spheres by dissipative particle dynamics. *Phys Fluids* 2006;18(10):103605.
- [120] Fan X, Phan-Thien N, Yong NT, Wu X, Xu D. Microchannel flow of a macromolecular suspension. *Phys Fluids* 2003;15(1):11–21.
- [121] Fan X, Phan-Thien N, Chen S, Wu X, Ng TY. Simulating flow of DNA suspension using dissipative particle dynamics. *Phys Fluids* 2006;18(6):063102.
- [122] Willemsen SM, Hoefsloot HCJ, Iedema PD. No-slip boundary condition in dissipative particle dynamics. *Int J Mod Phys C* 2000;11(5):881–90.
- [123] Malfreyt P, Tildesley DJ. Dissipative particle dynamics simulations of grafted polymer chains between two walls. *Langmuir* 2000;16(10):4732–40.
- [124] Jones LJ, Lal M, Noel Ruddock J, Spenay AN. Dynamics of a drop at a liquid/solid interface in simple shear fields: a mesoscopic simulation study. *Faraday Discuss* 1999;112(0):129–42.
- [125] Pivkin IV, Karniadakis GE. A new method to impose no-slip boundary conditions in dissipative particle dynamics. *J Comput Phys* 2005;207(1):114–28.
- [126] Pivkin IV, Karniadakis GE. Controlling density fluctuations in wall-bounded dissipative particle dynamics systems. *Phys Rev Lett* 2006;96(20):206001.
- [127] Duong-Hong D, Phan-Thien N, Fan X. An implementation of no-slip boundary conditions in DPD. *Comput Mech* 2004;35(1):24–9.
- [128] Xu Z, Meakin P. A phase-field approach to no-slip boundary conditions in dissipative particle dynamics and other particle models for fluid flow in geometrically complex confined systems. *J Chem Phys* ;130(23).
- [129] Boek ES, Coveney PV, Lekkerkerker HNW. Computer simulation of rheological phenomena in dense colloidal suspensions with dissipative particle dynamics. *J Phys Condens Matter* 1996;8(47):9509.
- [130] Boek ES, Coveney PV, Lekkerkerker HNW, van der Schoot P. Simulating the rheology of dense colloidal suspensions using dissipative particle dynamics. *Phys Rev E* 1997;55(3):3124–33.
- [131] Santo KP, Vishnyakov A, Kumar R, Neimark AV. Elucidating the effects of metal complexation on morphological and rheological properties of polymer solutions by a dissipative particle dynamics model. *Macromolecules* 2018;51(14):4987–5000.
- [132] Çağın T, Pettitt BM. Molecular dynamics with a variable number of molecules. *Mol Phys* 1991;72(1):169–75.
- [133] Escobedo FA, de Pablo JJ. Expanded grand canonical and Gibbs ensemble Monte Carlo simulation of polymers. *J Chem Phys* 1996;105(10):4391–4.
- [134] Maillet JB, Souillard L, Stoltz G. A reduced model for shock and detonation waves. II. The reactive case. *Europhys Lett* 2007;78(6):68001.
- [135] Kroonblawd MP, Sewell TD, Maillet J-B. Characteristics of energy exchange between inter- and intramolecular degrees of freedom in crystalline 1,3,5-triamino-2,4,6-trinitrobenzene (TATB) with implications for coarse-grained simulations of shock waves in polyatomic molecular crystals. *J Chem Phys* 2016;144(6):064501.
- [136] Vishnyakov A, Talaga DS, Neimark AV. DPD simulation of protein conformations: from α -helices to β -structures. *J Phys Chem Lett* 2012;3(21):3081–7.
- [137] Lee M-T, Vishnyakov A, Neimark AV. Modeling proton dissociation and transfer using dissipative particle dynamics simulation. *J Chem Theory Comput* 2015;11(9):4395–403.
- [138] Lee M-T, Vishnyakov A, Neimark AV. Coarse-grained model of water diffusion and proton conductivity in hydrated polyelectrolyte membrane. *J Chem Phys* 2016;144(1):014902.
- [139] Vishnyakov A, Mao R, Lee M-T, Neimark AV. Coarse-grained model of nanoscale segregation, water diffusion, and proton transport in Nafion membranes. *J Chem Phys* 2018;148(2):024108.
- [140] Clark JA, Santos EE, Frischknecht AL. Morphology and proton diffusion in a coarse-grained model of sulfonated poly(phenylenes). *J Chem Phys* 2019;151(10):104901.

- [141] Kacar G, de With G. Parametrizing hydrogen bond interactions in dissipative particle dynamics simulations: the case of water, methanol and their binary mixtures. *J Mol Liq* 2020;302:112581.
- [142] Santo KP, Neimark AV. Effects of metal-polymer complexation on structure and transport properties of metal-substituted polyelectrolyte membranes. *J Colloid Interface Sci* 2021;602:654–68.
- [143] Santo KP, Fabijanic KI, Cheng C-Y, Potanin A, Neimark AV. Modeling of the effects of metal complexation on the morphology and rheology of xanthan gum polysaccharide solutions. *Macromolecules* 2021;142.
- [144] Maiti Amitesh, McGrother S. Bead-bead interaction parameters in dissipative particle dynamics: relation to bead-size, solubility parameter, and surface tension. *J Chem Phys* ;120(3):1594–601.
- [145] Liyana-Arachchi TP, Jamadagni SN, Eike D, Koenig PH, Siepmann JI. Liquid-liquid equilibria for soft-repulsive particles: improved equation of state and methodology for representing molecules of different sizes and chemistry in dissipative particle dynamics. *J Chem Phys* 2015;142(4):044902.
- [146] Español P. Dissipative particle dynamics for a harmonic chain: a first-principles derivation. *Phys Rev E* 1996;53(2):1572–8.
- [147] Cubero D, Yaliraki SN. Formal derivation of dissipative particle dynamics from first principles. *Phys Rev E* 2005;72(3):032101.
- [148] Cubero D, Yaliraki SN. Inhomogeneous multiscale dynamics in harmonic lattices. *J Chem Phys* 2005;122(3):034108.
- [149] Español P, Serrano M. Dynamical regimes in the dissipative particle dynamics model. *Phys Rev E* 1999;59(6):6340–7.
- [150] Español P, Serrano M, Ottinger HC. Thermodynamically admissible form for discrete hydrodynamics. *Phys Rev Lett* 1999;83(22):4542–5.
- [151] Hijon C, Serrano M, Espanol P. Markovian approximation in a coarse-grained description of atomic systems. *J Chem Phys* ;125(20).
- [152] Kinjo T, Hyodo S-A. Equation of motion for coarse-grained simulation based on microscopic description. *Phys Rev E* 2007;75(5):051109.
- [153] Hijon C, Espanol P, Vanden-Eijnden E, Delgado-Buscalioni R. Mori-Zwanzig formalism as a practical computational tool. *Faraday Discuss* 2010;144:301–22.
- [154] Li Z, Bian X, Caswell B, Karniadakis GE. Construction of dissipative particle dynamics models for complex fluids via the Mori-Zwanzig formulation. *Soft Matter* 2014;10(43):8659–72.
- [155] Sepehr F, Paddison SJ. Dissipative particle dynamics interaction parameters from ab initio calculations. *Chem Phys Lett* 2016;645:20–6.
- [156] Okuwaki K, Mochizuki Y, Doi H, Ozawa T. Fragment molecular orbital based parametrization procedure for mesoscopic structure prediction of polymeric materials. *J Phys Chem B* 2018;122(1):338–47.
- [157] Lee M-T, Vishnyakov A, Neimark AV. Calculations of critical micelle concentration by dissipative particle dynamics simulations: the role of chain rigidity. *J Phys Chem B* 2013;117(35):10304–10.
- [158] Mao R, Lee M-T, Vishnyakov A, Neimark AV. Modeling aggregation of ionic surfactants using a smeared charge approximation in dissipative particle dynamics simulations. *J Phys Chem B* 2015;119(35):11673–83.
- [159] Vishnyakov A, Lee M-T, Neimark AV. Prediction of the critical Micelle concentration of nonionic surfactants by dissipative particle dynamics simulations. *J Phys Chem Lett* 2013;4(5):797–802.
- [160] Padding JT, Briels WJ. Time and length scales of polymer melts studied by coarse-grained molecular dynamics simulations. *J Chem Phys* 2002;117(2):925–43.
- [161] Reith D, Meyer H, Müller-Plathe F. Mapping atomistic to coarse-grained polymer models using automatic simplex optimization to fit structural properties. *Macromolecules* 2001;34(7):2335–45.
- [162] Deichmann G, Marcon V, van der Vegt NFA. Bottom-up derivation of conservative and dissipative interactions for coarse-grained molecular liquids with the conditional reversible work method. *J Chem Phys* 2014;141(22).
- [163] Yoshimoto Y, Kinefuchi I, Mima T, Fukushima A, Tokumasu T, Takagi S. Bottom-up construction of interaction models of non-Markovian dissipative particle dynamics. *Phys Rev E* ;88(4).
- [164] Eriksson A, Jacobi MN, Nystroem J, Tunstrom K. Using force covariance to derive effective stochastic interactions in dissipative particle dynamics. *Phys Rev E* 2008; 77(1).
- [165] Eriksson A, Jacobi MN, Nystrom J, Tunstrom K. On the microscopic foundation of dissipative particle dynamics. *Epl* 2009;86(4).
- [166] Li Z, Lee HS, Darve E, Karniadakis GE. Computing the non-Markovian coarse-grained interactions derived from the Mori-Zwanzig formalism in molecular systems: application to polymer melts. *J Chem Phys* 2017;146(1):014104.
- [167] Trément S, Schnell B, Petitjean L, Couty M, Rousseau B. Conservative and dissipative force field for simulation of coarse-grained alkane molecules: a bottom-up approach. *J Chem Phys* 2014;140(13):134113.
- [168] Español P, Zúñiga I. Obtaining fully dynamic coarse-grained models from MD. *Phys Chem Chem Phys* 2011;13(22):10538–45.
- [169] Harmandaris V, Kalligiannaki E, Katsoulakis M, Plecháč P. Path-space variational inference for non-equilibrium coarse-grained systems. *J Comput Phys* 2016;314: 355–83.
- [170] Dequidt A, Solano Canchaya JG. Bayesian parametrization of coarse-grain dissipative dynamics models. *J Chem Phys* 2015;143(8):084122.
- [171] Pan W, Caswell B, Karniadakis GE. Rheology, microstructure and migration in Brownian colloidal suspensions. *Langmuir* 2010;26(1):133–42.
- [172] Pan W, Pivkin IV, Karniadakis GE. Single-particle hydrodynamics in DPD: A new formulation. *Epl* 2008;84(1).
- [173] Tran-Duc T, Phan-Thien N, Khoo BC. Rheology of bubble suspensions using dissipative particle dynamics. Part I: a hard-core DPD particle model for gas bubbles. *J. Rheol.* 2013;57(6):1715–37.
- [174] Wang X, Santo KP, Neimark AV. Modeling gas-liquid interfaces by dissipative particle dynamics: adsorption and surface tension of cetyl trimethyl ammonium bromide at the air-water interface. *Langmuir* 2020;36(48):14686–98.
- [175] Hong B, Qiu F, Zhang H, Yang Y. Budding dynamics of individual domains in multicomponent membranes simulated by N-varied dissipative particle dynamics. *J Phys Chem B* 2007;111(21):5837–49.
- [176] Yue T, Li S, Zhang X, Wang W. The relationship between membrane curvature generation and clustering of anchored proteins: a computer simulation study. *Soft Matter* 2010;6(24):6109–18.
- [177] Yue TT, Li SX, Xu Y, Zhang XR, Huang F. Interplay between nanoparticle wrapping and clustering of inner anchored membrane proteins. *J Phys Chem B* 2016;120(42):11000–9.
- [178] Pivkin IV, Karniadakis GE. Coarse-graining limits in open and wall-bounded dissipative particle dynamics systems. *J Chem Phys* 2006;124(18):184101.
- [179] Dzwiniel W, Yuen DA. Matching macroscopic properties of binary fluids to the interactions of dissipative particle dynamics. *Int J Mod Phys C* 2000;11(01):1–25.
- [180] Fuchslin RM, Fellermann H, Eriksson A, Ziock H-J. Coarse graining and scaling in dissipative particle dynamics. *J Chem Phys* 2009;130(21):214102.
- [181] Wijmans CM, Smit B, Groot RD. Phase behavior of monomeric mixtures and polymer solutions with soft interaction potentials. *J Chem Phys* 2001;114(17): 7644–54.
- [182] Fredenslund Aage, Jones Russell L, Prausnitz John M. Group-contribution estimation of activity coefficients in nonideal liquid mixtures. *AIChE J* 1975;21 (6):1086–99.
- [183] Klamt A, Schüürmann G. COSMO: a new approach to dielectric screening in solvents with explicit expressions for the screening energy and its gradient. *J Chem Soc Perkin Trans* ;2(5):799–805.
- [184] Kushare SK, Shaikh VR, Terdale SS, Dagade DH, Kolhapurkar RR, Patil KJ. Thermodynamics of aqueous polyethylene-glycol (PEG) solutions at 298.15K: activity, activity coefficients and application of molecular theories. *J Mol Liq* 2013;187:129–36.
- [185] Backer JA, Lowe CP, Hoefsloot H CJ, Iedema PD. Combined length scales in dissipative particle dynamics. *J Chem Phys* 2005;123(11):114905.
- [186] Spaeth JR, Dale T, Kevrekidis IG, Panagiotopoulos AZ. Coarse-graining of chain models in dissipative particle dynamics simulations. *Ind Eng Chem Res* 2011;50 (1):69–77.
- [187] Kacar G, Peters EA, de With G. Multi-scale simulations for predicting material properties of a cross-linked polymer. *Comput Mater Sci* 2015;102:68–77.
- [188] Kacar G, Albers PTM, Esteves ACC, de With G. Mesoscopic structure and swelling properties of crosslinked polyethylene glycol in water. *J Coat Technol Res* 2018; 15(4):691–701.
- [189] Kacar G. Molecular understanding of interactions, structure, and drug encapsulation efficiency of Pluronic micelles from dissipative particle dynamics simulations. *Colloid Polym Sci* 2019;297(7):1037–51.
- [190] Kacar G. Thermodynamic stability of ibuprofen loaded poloxamer micelles. *Chem Phys* 2020;533:110713.
- [191] Tang X, Zou W, Koenig PH, McConaughy SD, Weaver MR, Eike DM, et al. Multiscale modeling of the effects of salt and perfume raw materials on the rheological properties of commercial thredlike Micellar solutions. *J Phys Chem B* 2017;121(11):2468–85.
- [192] Johnson JK, Mueller EA, Gubbins KE. Equation of state for Lennard-Jones chains. *J Phys Chem* 1994;98(25):6413–9.
- [193] Anderson RL, Bray DJ, Del Regno A, Seaton MA, Ferrante AS, Warren PB. Micelle formation in alkyl sulfate surfactants using dissipative particle dynamics. *J Chem Theory Comput* 2018;14(5):2633–43.
- [194] Panoukidou M, Wand CR, Del Regno A, Anderson RL, Carbone P. Constructing the phase diagram of sodium laurylthioxysulfate using dissipative particle dynamics. *J Colloid Interface Sci* 2019;557:34–44.
- [195] Beckers JVL, Lowe CP, De Leeuw SW. An iterative PPPM method for simulating coulombic systems on distributed memory parallel computers. *Mol Simul* 1998;20 (6):369–83.
- [196] González-Melchor M, Mayoral E, Velázquez ME, Alejandre J. Electrostatic interactions in dissipative particle dynamics using the Ewald sums. *J Chem Phys* 2006;125(22):224107.
- [197] Kiss PT, Segal M, Baranyai A. Efficient handling of Gaussian charge distributions: an application to polarizable molecular models. *J Chem Theory Comput* 2014;10 (12):5513–9.
- [198] Coslovich D, Hansen J-P, Kahl G. Ultra-soft primitive model of polyionic solutions: structure, aggregation, and dynamics. *J Chem Phys* 2011;134(24):244514.
- [199] Warren PB, Masters AJ. Phase behaviour and the random phase approximation for ultra-soft restricted primitive models. *J Chem Phys* 2013;138(7):074901.
- [200] Wang H, Tang X, Eike DM, Larson RG, Koenig PH. Scission free energies for wormlike surfactant micelles: development of a simulation protocol, application, and validation for personal care formulations. *Langmuir* 2018;34(4):1564–73.
- [201] Kong Y, Manke CW, Madden WG, Schlijper AG. Simulation of a confined polymer in solution using the dissipative particle dynamics method. *Int J Thermophys* 1994;15(6):1093–110.
- [202] Kong Y, Manke CW, Madden WG, Schlijper AG. Effect of solvent quality on the conformation and relaxation of polymers via dissipative particle dynamics. *J Chem Phys* 1997;107(2):592–602.
- [203] Schlijper AG, Hoogerbrugge PJ, Manke CW. Computer simulation of dilute polymer solutions with the dissipative particle dynamics method. *J Rheol* 1995; 39(3):567–79.
- [204] Kong Y, Manke CW, Madden WG, Schlijper AG. Modeling the rheology of polymer solutions by dissipative particle dynamics. *Tribol Lett* 1997;3(1):133–8.

- [205] Spenley NA. Scaling laws for polymers in dissipative particle dynamics. *Europhys Lett* 2000;49(4):534.
- [206] Masao Doi SFE. The theory of polymer dynamics. New York: Oxford University Press; 1986.
- [207] Chrissopoulou K, Anastasiadis SH. Effects of nanoscopic-confinement on polymer dynamics. *Soft Matter* 2015;11(19):3746–66.
- [208] Fedosov DA, Karniadakis GE, Caswell B. Dissipative particle dynamics simulation of depletion layer and polymer migration in micro- and nanochannels for dilute polymer solutions. *J Chem Phys* 2008;128(14):144903.
- [209] Millan JA, Jiang W, Laradji M, Wang Y. Pressure driven flow of polymer solutions in nanoscale slit pores. *J Chem Phys* 2007;126(12):124905.
- [210] Segré G, Silberberg A. Radial particle displacements in Poiseuille flow of suspensions. *Nature* 1961;189(4760):209–10.
- [211] Millan JA, Laradji M. Cross-stream migration of driven polymer solutions in nanoscale channels: a numerical study with generalized dissipative particle dynamics. *Macromolecules* 2009;42(3):803–10.
- [212] Pan G, Manke CW. Effects of solvent quality on the dynamics of polymer solutions simulated by dissipative particle dynamics. *J Rheol* 2002;46(5):1221–37.
- [213] Litvinov S, Hu XY, Adams NA. Numerical simulation of tethered DNA in shear flow. *J Phys Condens Matter* 2011;23(18).
- [214] Freeman PI, Rowlinson JS. Lower critical points in polymer solutions. *Polymer* 1960;1:20–6.
- [215] van Vliet RE, Dreischor MW, Hoefsloot HCJ, Iedema PD. Dynamics of liquid–liquid demixing: mesoscopic simulations of polymer solutions. *Fluid Phase Equilib* 2002;201(1):67–78.
- [216] Qian H-J, Chen L-J, Lu Z-Y, Li Z-S. Surface diffusion dynamics of a single polymer chain in dilute solution. *Phys Rev Lett* 2007;99(6):068301.
- [217] Yang K, Vishnyakov A, Neimark AV. Polymer translocation through a Nanopore: DPD study. *J Phys Chem B* 2013;117(13):3648–58.
- [218] Groot RD. Mesoscopic simulation of polymer–surfactant aggregation. *Langmuir* 2000;16(19):7493–502.
- [219] Rabatekar SS, Hamm M, Shaffer MSP, Elliott JA. Mesoscale modeling of electrical percolation in fiber-filled systems. *J Chem Phys* 2005;123(13):134702.
- [220] Nikunen P, Vattulainen I, Karttunen M. Reptational dynamics in dissipative particle dynamics simulations of polymer melts. *Phys Rev E* ;75(3).
- [221] Padding JT, Briels WJ. Uncrossability constraints in mesoscopic polymer melt simulations: non-Rouse behavior of C120H242. *J Chem Phys* 2001;115(6):2846–59.
- [222] Chappa VC, Morse DC, Zippelius A, Müller M. Translationally invariant slip-spring model for entangled polymer dynamics. *Phys Rev Lett* 2012;109(14):148302.
- [223] Langeloth M, Masubuchi Y, Böhm MC, Müller-Plathe F. Recovering the reptation dynamics of polymer melts in dissipative particle dynamics simulations via slip-springs. *J Chem Phys* 2013;138(10):104907.
- [224] Kumar S, Larson RG. Brownian dynamics simulations of flexible polymers with spring–spring repulsions. *J Chem Phys* 2001;114(15):6937–41.
- [225] Pan G, Manke CW. Developments toward simulation of entangled polymer melts by dissipative particle dynamics (DPD). *Int J Mod Phys B* 2003;17(01n02):231–5.
- [226] Goujon F, Malfreyt P, Tildesley DJ. Mesoscopic simulation of entanglements using dissipative particle dynamics: application to polymer brushes. *J Chem Phys* 2008;129(3):034902.
- [227] Sirk TW, Slizoberg YR, Brennan JK, Lital M, Andzelm JW. An enhanced entangled polymer model for dissipative particle dynamics. *J Chem Phys* 2012;136(13):134903.
- [228] Goujon F, Martzel N, Dequidt A, Latour B, Garruchet S, Devémy J, et al. Backbone oriented anisotropic coarse grains for efficient simulations of polymers. *J Chem Phys* 2020;153(21):214901.
- [229] Guerrault X, Rousseau B, Farago J. Dissipative particle dynamics simulations of polymer melts. I. Building potential of mean force for polyethylene and cis-polybutadiene. *J Chem Phys* 2004;121(13):6538–46.
- [230] Lahmar F, Rousseau B. Influence of the adjustable parameters of the DPD on the global and local dynamics of a polymer melt. *Polymer* 2007;48(12):3584–92.
- [231] Yamanoi M, Pozo O, Maia JM. Linear and non-linear dynamics of entangled linear polymer melts by modified tunable coarse-grained level Dissipative Particle Dynamics. *J Chem Phys* 2011;135(4).
- [232] Wang J, Chen X, Cao C, Yu D. Chain conformation and dynamics in ultrahigh molecular weight polyethylene melts undergoing extensional–shear coupled flow: insight from dissipative particle dynamics simulation. *Polym Int* 2020;69(12):1213–9.
- [233] Nafar Sefiddashti MH, Boudaghi-Khajejhnobar M, Edwards BJ, Khomami B. High-fidelity scaling relationships for determining dissipative particle dynamics parameters from atomistic molecular dynamics simulations of polymeric liquids. *Sci Rep* 2020;10(1):4458.
- [234] Padding JT, Briels WJ. Systematic coarse-graining of the dynamics of entangled polymer melts: the road from chemistry to rheology. *J Phys Condens Matter* 2011;23(23):233101.
- [235] Groot RD, Madden TJ. Dynamic simulation of diblock copolymer microphase separation. *J Chem Phys* 1998;108(20):8713–24.
- [236] Groot RD, Madden TJ, Tildesley DJ. On the role of hydrodynamic interactions in block copolymer microphase separation. *J Chem Phys* 1999;110(19):9739–49.
- [237] Bates FS, Fredrickson GH. Block copolymer thermodynamics: theory and experiment. *Annu Rev Phys Chem* 1990;41(1):525–57.
- [238] Zhang K, Manke CW. Simulation of diblock copolymer melts by dissipative particle dynamics. *Comput Phys Commun* 2000;129(1):275–81.
- [239] Gavrillov AA, Kudryavtsev YV, Chertovich AV. Phase diagrams of block copolymer melts by dissipative particle dynamics simulations. *J Chem Phys* 2013;139(22):224901.
- [240] Liu DH, Zhong CL. Dissipative particle dynamics simulation of microphase separation and properties of linear-dendritic diblock copolymer melts under steady shear flow. *Macromol Rapid Commun* 2005;26(24):1960–4.
- [241] Cao X, Xu G, Li Y, Zhang Z. Aggregation of poly(ethylene oxide)–poly(propylene oxide) block copolymers in aqueous solution: DPD simulation study. *J Phys Chem A* 2005;109(45):10418–23.
- [242] Sheng Y-J, Wang T-Y, Chen WM, Tsao H-K. A–B Diblock copolymer Micelles: effects of soluble-block length and component compatibility. *J Phys Chem B* 2007;111(37):10938–45.
- [243] Slizoberg YR, Andzelm JW, Brennan JK, Vanlandingham MR, Pryamitsyn V, Ganesan V. Modeling viscoelastic properties of triblock copolymers: a DPD simulation study. *J Polym Sci B* 2010;48(1):15–25.
- [244] Alvarez F, Flores EA, Castro LV, Hernández JG, López A, Vázquez F. Dissipative particle dynamics (DPD) study of crude oil–water emulsions in the presence of a functionalized co-polymer. *Energy Fuel* 2011;25(2):562–7.
- [245] Zhou Z, Li Z, Ren Y, Hillmyer MA, Lodge TP. Micellar shape change and internal segregation induced by chemical modification of a Tryptich block copolymer surfactant. *J Am Chem Soc* 2003;125(34):10182–3.
- [246] Chou S-H, Tsao H-K, Sheng Y-J. Morphologies of multicompartiment micelles formed by triblock copolymers. *J Chem Phys* 2006;125(19):194903.
- [247] Guo XD, Tan JPK, Kim SH, Zhang LJ, Zhang Y, Hedrick JL, et al. Computational studies on self-assembled paclitaxel structures: templates for hierarchical block copolymer assemblies and sustained drug release. *Biomaterials* 2009;30(33):6556–63.
- [248] Lin WJ, Nie SY, Chen Q, Qian Y, Wen XF, Zhang LJ. Structure–property relationship of pH-sensitive (PCL)₂(PDEA-b-PPEGMA)₂ micelles: experiment and DPD simulation. *AIChE J* 2014;60(10):3634–46.
- [249] Wang H, Liu Y-T, Qian H-J, Lu Z-Y. Dissipative particle dynamics simulation study on complex structure transitions of vesicles formed by comb-like block copolymers. *Polymer* 2011;52(9):2094–101.
- [250] Yu H, Qiu X, Moreno N, Ma Z, Calo VM, Nunes SP, et al. Self-assembled asymmetric block copolymer membranes: bridging the gap from ultra- to nanofiltration. *Angew Chem Int Ed* 2015;54(47):13937–41.
- [251] Binder K, Kreer T, Milchev A. Polymer brushes under flow and in other out-of-equilibrium conditions. *Soft Matter* 2011;7(16):7159–72.
- [252] Ionov L, Houbenov N, Sidorenko A, Stamm M, Minko S. Smart microfluidic channels. *Adv Funct Mater* 2006;16(9):1153–60.
- [253] Irfachsyad D, Tildesley D, Malfreyt P. Dissipative particle dynamics simulation of grafted polymer brushes under shear. *Phys Chem Chem Phys* 2002;4(13):3008–15.
- [254] Wijmans CM, Smit B. Simulating tethered polymer layers in shear flow with the dissipative particle dynamics technique. *Macromolecules* 2002;35(18):7138–48.
- [255] Pal S, Seidel C. Dissipative particle dynamics simulations of polymer brushes: comparison with molecular dynamics simulations. *Macromol Theory Simul* 2006;15(9):668–73.
- [256] Seidel C, Netz RR. Individual polymer paths and end-point stretching in polymer brushes. *Macromolecules* 2000;33(2):634–40.
- [257] Pastorino C, Kreer T, Müller M, Binder K. Comparison of dissipative particle dynamics and Langevin thermostats for out-of-equilibrium simulations of polymeric systems. *Phys Rev E* 2007;76(2):026706.
- [258] Pastorino C, Müller M. Mixed brush of chemically and physically adsorbed polymers under shear: inverse transport of the physisorbed species. *J Chem Phys* 2014;140(1):014901.
- [259] Cheng J, Vishnyakov A, Neimark AV. Morphological transformations in polymer brushes in binary mixtures: DPD study. *Langmuir* 2014;30(43):12932–40.
- [260] Deng M, Li X, Liang H, Caswell B, Karniadakis GE. Simulation and modelling of slip flow over surfaces grafted with polymer brushes and glycoalyx fibres. *J Fluid Mech* 2012;711:192–211.
- [261] Santo KP, Vishnyakov A, Brun Y, Neimark AV. Adhesion and separation of nanoparticles on polymer-grafted porous substrates. *Langmuir* 2018;34(4):1481–96.
- [262] Santo KP, Vishnyakov A, Brun Y, Neimark AV. Critical conditions of adhesion and separation of functionalized nanoparticles on polymer grafted substrates. *J Phys Chem C* 2019;123:16091–106.
- [263] Li N, Zuo C, Cao Q. Nanopores with solvent-sensitive polymer brushes: a dissipative particle dynamics simulation. *J Macromol Sci Phys* 2012;51(2):275–87.
- [264] Goujon F, Malfreyt P, Tildesley DJ. Dissipative particle dynamics simulations in the grand canonical ensemble: applications to polymer brushes. *Chem Phys Chem* 2004;5(4):457–64.
- [265] de Gennes PG. Polymers at an interface; a simplified view. *Adv Colloid Interface Sci* 1987;27(3):189–209.
- [266] Goujon F, Malfreyt P, Tildesley DJ. Mesoscopic simulation of entangled polymer brushes under shear: compression and rheological properties. *Macromolecules* 2009;42(12):4310–8.
- [267] Goujon F, Ghoufi A, Malfreyt P, Tildesley DJ. Frictional forces in polyelectrolyte brushes: effects of sliding velocity, solvent quality and salt. *Soft Matter* 2012;8(17):4635–44.
- [268] Symeonidis V, Em Karniadakis G, Caswell B. Dissipative particle dynamics simulations of polymer chains: scaling Laws and Shearing response compared to DNA experiments. *Phys Rev Lett* 2005;95(7):076001.

- [269] Pan H, Ng TY, Li H, Moendarbary E. Dissipative particle dynamics simulation of entropic trapping for DNA separation. *Sensors Actuators A Phys* 2010;157(2): 328–35.
- [270] Moendarbary E, Ng TY, Pan H, Lam KY. Migration of DNA molecules through entropic trap arrays: a dissipative particle dynamics study. *Microfluid Nanofluid* 2010;8(2):243–54.
- [271] Ranjith SK, Patnaik BSV, Vedantam S. Transport of DNA in hydrophobic microchannels: a dissipative particle dynamics simulation. *Soft Matter* 2014;10(23):4184–91.
- [272] Valdivia A, Jaime C. Carbon nanotube transmembrane channel formation and single-stranded DNA spontaneous internalization: a dissipative particle dynamics study. *Soft Matter* 2021;17(4):1028–36.
- [273] Posel Z, Svoboda M, Colina CM, Lísal M. Flow and aggregation of rod-like proteins in slit and cylindrical pores coated with polymer brushes: an insight from dissipative particle dynamics. *Soft Matter* 2017;13(8):1634–45.
- [274] Li C, Fu X, Zhong W, Liu J. Dissipative particle dynamics simulations of a protein-directed self-assembly of nanoparticles. *ACS Omega* 2019;4(6):10216–24.
- [275] Wang L, Chen Z, Zhang J, Zhang X, Wu ZJ. Modeling clot formation of shear-injured platelets in flow by a dissipative particle dynamics method. *Bull Math Biol* 2020;82(7):83.
- [276] Zhai Y, Martys NS, George WL, Curtis JE, Nayem J, Liu Y. Intermediate scattering functions of a rigid body monoclonal antibody protein in solution studied by dissipative particle dynamic simulation. *Struct Dyn* 2021;8(2):024102.
- [277] Peter EK, Lykov K, Pivkin IV. A polarizable coarse-grained protein model for dissipative particle dynamics. *Phys Chem Chem Phys* 2015;17(37):24452–61.
- [278] Kawai R, Chiba S, Okuwaki K, Kanada R, Doi H, Ono M, et al. Stabilization mechanism for a nonfibrillar amyloid β oligomer based on formation of a hydrophobic core determined by dissipative particle dynamics. *ACS Chem Neurosci* 2020;11(3):385–94.
- [279] Okuwaki K, Doi H, Fukuzawa K, Mochizuki Y. Folding simulation of small proteins by dissipative particle dynamics (DPD) with non-empirical interaction parameters based on fragment molecular orbital calculations. *Appl Phys Express* 2019;13(1):017002.
- [280] Choudhury CK, Kuksenok O. Native-based dissipative particle dynamics approach for α -helical folding. *J Phys Chem B* 2020;124(50):11379–86.
- [281] Ibergay C, Malfreyt P, Tildesley DJ. Interaction between two polyelectrolyte brushes: a mesoscale modelling of the compression. *Soft Matter* 2011;7(10): 4900–7.
- [282] Meneses-Juárez E, Márquez-Beltrán C, Rivas-Silva JF, Pal U, González-Melchor M. The structure and interaction mechanism of a polyelectrolyte complex: a dissipative particle dynamics study. *Soft Matter* 2015;11(29):5889–97.
- [283] Gavrilov AA, Chertovich AV, Kramarenko EY. Conformational behavior of a single polyelectrolyte chain with bulky counterions. *Macromolecules* 2016;49(3): 1103–10.
- [284] Li NK, Kuang H, Fuss WH, Zauscher S, Kokkoli E, Yingling YG. Salt responsive morphologies of ssDNA-based triblock polyelectrolytes in semi-dilute regime: effect of volume fractions and polyelectrolyte length. *Macromol Rapid Commun* 2017;38(20):1700422.
- [285] Lísal M, Sındelka K, Suchá L, Limpouchová Z, Procházka K. Dissipative particle dynamics simulations of polyelectrolyte self-assemblies. Methods with explicit electrostatics. *Polymer Sci Ser C* 2017;59(1):77–101.
- [286] Lísal M, Limpouchová Z, Procházka K. The self-assembly of copolymers with one hydrophobic and one polyelectrolyte block in aqueous media: a dissipative particle dynamics study. *Phys Chem Chem Phys* 2016;18(24):16127–36.
- [287] Sındelka K, Limpouchová Z, Lísal M, Procházka K. Dissipative particle dynamics study of electrostatic self-assembly in aqueous mixtures of copolymers containing one neutral water-soluble block and one either positively or negatively charged polyelectrolyte block. *Macromolecules* 2014;47(17):6121–34.
- [288] Zhou H, Han Y, Mei Y, Wei Y, Wang H. Study on response behaviors of mixed solution of polyelectrolytes and worms under shear. *J Polym Res* 2014;21(2):351.
- [289] Dorenbos G, Suga Y. Simulation of equivalent weight dependence of Nafion morphologies and predicted trends regarding water diffusion. *J Membr Sci* 2009; 330(1):5–20.
- [290] Dorenbos G. Competition between side chain length and side chain distribution: searching for optimal polymeric architectures for application in fuel cell membranes. *J Power Sources* 2015;276:328–39.
- [291] Vishnyakov A, Neimark AV. Self-assembly in Nafion membranes upon hydration: water mobility and adsorption isotherms. *J Phys Chem B* 2014;118(38): 11353–64.
- [292] Dorenbos G. Dependence of percolation threshold on side chain distribution within amphiphilic polyelectrolyte membranes. *RSC Adv* 2013;3(40):18630–42.
- [293] Yamamoto S, Hyodo S-A. A computer simulation study of the mesoscopic structure of the polyelectrolyte membrane Nafion. *Polym J* 2003;35:519.
- [294] Alarcón F, Pérez E, Gama Goicochea A. Dissipative particle dynamics simulations of weak polyelectrolyte adsorption on charged and neutral surfaces as a function of the degree of ionization. *Soft Matter* 2013;9(14):3777–88.
- [295] Cao Q, Zuo C, Li L, Zhang Y. Electrophoresis of bottle-brush polyelectrolytes in an attractive Nanochannel. *Macromol Theory Simul* 2012;21(7):492–9.
- [296] Yan L-T, Guo R. Effects of multivalent counterions on the morphology and interactions of polyelectrolyte chains grafted on carbon nanotubes. *Soft Matter* 2012;8(3):660–6.
- [297] Yan L-T, Xu Y, Ballauff M, Müller AHE, Böker A. Influence of Counterion Valency on the conformational behavior of cylindrical polyelectrolyte brushes. *J Phys Chem B* 2009;113(15):5104–10.
- [298] Nagarajan K, Chen SB. Translocation of star polyelectrolytes through a Nanopore. *J Phys Chem B* 2019;123(14):3124–34.
- [299] Smiatek J, Schmid F. Mesoscopic simulations of polyelectrolyte electrophoresis in nanochannels. Berlin, Heidelberg: Springer Berlin Heidelberg; 2011. p. 53–67.
- [300] Sirchabesan M, Giasson S. Mesoscale simulations of the behavior of charged polymer brushes under normal compression and lateral shear forces. *Langmuir* 2007;23(19):9713–21.
- [301] Venturoli M, Smit B. Simulating the self-assembly of model membranes. *PhysChemComm* 1999;2(10):45–9.
- [302] Kranenburg M, Venturoli M, Smit B. Molecular simulations of mesoscopic bilayer phases. *Phys Rev E* ;67(6).
- [303] Yamamoto S, Maruyama Y, Hyodo S-A. Dissipative particle dynamics study of spontaneous vesicle formation of amphiphilic molecules. *J Chem Phys* 2002;116(13):5842–9.
- [304] Yamamoto S, Hyodo S-A. Budding and fission dynamics of two-component vesicles. *J Chem Phys* 2003;118(17):7937–43.
- [305] Yamamoto S, Hyodo S-A. Mesoscopic simulation of the crossing dynamics at an entanglement point of surfactant threadlike micelles. *J Chem Phys* 2005;122(20): 204907.
- [306] Laradji M, Sunil Kumar PB. Dynamics of domain growth in self-assembled fluid vesicles. *Phys Rev Lett* 2004;93(19):198105.
- [307] Shang YZ, Xu Y, Liu HL, Hu Y. The formation and properties of multilamellar vesicles in Gemini/SDS/H₂O system. *J Dispers Sci Technol* 2006;27(1):105–8.
- [308] Li Y, Zhang H, Wang Z, Bao M. Micelle-vesicle transitions in cationic mixtures of SDS/DTAB induced by salt, temperature, and selective solvents: a dissipative particle dynamics simulation study. *Colloid Polym Sci* 2014;292(9):2349–60.
- [309] Li DW, Liu XY, Feng YP. Bond-angle-potential-dependent dissipative particle dynamics simulation and lipid inverted phase. *J Phys Chem B* 2004;108(30): 11206–13.
- [310] Sun HY, Xu GY, Li YM, Chen YJ. Mesoscopic simulation of the aggregation behavior of fluorinated surfactant in aqueous solution. *J Fluor Chem* 2006;127(2):187–92.
- [311] Yang CJ, Chen X, Qiu HY, Zhuang WC, Chai YC, Hao JC. Dissipative particle dynamics simulation of phase behavior of aerosol OT/water system. *J Phys Chem B* 2006;110(43):21735–40.
- [312] Yuan SL, Cai ZT, Xu GY. Mesoscopic systems simulation of aggregates in surfactant/oil/water. *Chin J Chem* 2003;21(2):112–6.
- [313] Li Y, Zhang P, Dong FL, Cao XL, Song XW, Cui XH. The array and interfacial activity of sodium dodecyl benzene sulfonate and sodium oleate at the oil/water interface. *J Colloid Interface Sci* 2005;290(1):275–80.
- [314] Dong FL, Li Y, Zhang P. Mesoscopic simulation study on the orientation of surfactants adsorbed at the liquid/liquid interface. *Chem Phys Lett* 2004;399(1–3):215–9.
- [315] Rekvig L, Kranenburg M, Vreede J, Hafskjold B, Smit B. Investigation of surfactant efficiency using dissipative particle dynamics. *Langmuir* 2003;19(20):8195–205.
- [316] Rekvig L, Hafskjold B, Smit B. Chain length dependencies of the bending modulus of surfactant monolayers. *Phys Rev Lett* 2004;92(11):116101.
- [317] Deguillard E, Pannacci N, Creton B, Rousseau B. Interfacial tension in oil-water-surfactant systems: On the role of intra-molecular forces on interfacial tension values using DPD simulations. *J Chem Phys* ;138(14).
- [318] Ginzburg VV, Chang K, Jog PK, Argenton AB, Rakesh L. Modeling the interfacial tension in oil-water-nonionic surfactant mixtures using dissipative particle dynamics and self-consistent field theory. *J Phys Chem B* 2011;115(16):4654–61.
- [319] Khedr A, Striolo A. DPD parameters estimation for simultaneously simulating water-oil interfaces and aqueous nonionic surfactants. *J Chem Theory Comput* 2018;14(12):6460–71.
- [320] Griffin WC. Classification of surface-active agents by 'HLB'. *J Soc Cosmet Chem* 1949;1:311–26.
- [321] Liang XP, Wu JQ, Yang XG, Tu ZB, Wang Y. Investigation of oil-in-water emulsion stability with relevant interfacial characteristics simulated by dissipative particle dynamics. *Colloids Surf A Physicochem Eng Asp* 2018;546:107–14.
- [322] Santo KP, Kovalenko A, Stepanova M. Self-consistent field modeling of three-dimensional morphologies of branched lipid surfactant at air-water interface. *Macromol Theory Simul* 2010;19(5):228–39.
- [323] Pool R, Bolhuis PG. Can purely repulsive soft potentials predict micelle formation correctly? *Phys Chem Chem Phys* 2006;8(8):941–8.
- [324] Deng XJ, Yang Y, Ma Y, Sun XL, Zhou GG, Wu HC, et al. Self-assembled structure of sulfonic gemini surfactant solution. *AIP Adv* 2018;8(7).
- [325] Angelikopoulos P, Gromov A, Leen A, Nerushev O, Bock H, Campbell EEB. Dispersing individual single-wall carbon nanotubes in aqueous surfactant solutions below the cmc. *J Phys Chem C* 2010;114(1):2–9.
- [326] Li YM, Zhang HX, Bao MT, Chen QG. Aggregation behavior of surfactants with different molecular structures in aqueous solution: DPD simulation study. *J Dispers Sci Technol* 2012;33(10):1437–43.
- [327] Mai ZH, Couallier E, Rakib M, Rousseau B. Parameterization of a mesoscopic model for the self-assembly of linear sodium alkyl sulfates. *J Chem Phys* 2014;140(20).
- [328] Shillcock JC, Lipowsky R. The computational route from bilayer membranes to vesicle fusion. *J Phys Condens Matter* 2006;18(28):S1191–219.
- [329] Li X, Gao L, Fang W. Dissipative particle dynamics simulations for phospholipid membranes based on a four-to-one coarse-grained mapping scheme. *PLoS One* 2016;11(5):e0154568.
- [330] Guigas G, Morozova D, Weiss M. Exploring membrane and protein dynamics with dissipative particle dynamics. In: Christov C, editor. *Advances in protein chemistry and structural biology*, vol 85: computational chemistry methods in structural biology. Vol. 85; 2011. p. 143–82.

- [331] Venturoli M, Smit B, Sperotto MM. Simulation studies of protein-induced bilayer deformations, and lipid-induced protein tilting, on a mesoscopic model for lipid bilayers with embedded proteins. *Biophys J* 2005;88(3):1778–98.
- [332] Guigas G, Weiss M. Influence of hydrophobic mismatching on membrane protein diffusion. *Biophys J* 2008;95(3):L25–7.
- [333] Guigas G, Weiss M. Size-dependent diffusion of membrane inclusions. *Biophys J* 2006;91(7):2393–8.
- [334] Schmidt U, Guigas G, Weiss M. Cluster formation of transmembrane proteins due to hydrophobic mismatching. *Phys Rev Lett* ;101(12).
- [335] de Meyer FJ-M, Venturoli M, Smit B. Molecular simulations of lipid-mediated protein-protein interactions. *Biophys J* 2008;95(4):1851–65.
- [336] Lin MX, Yu TT, Wan JF, Cao XJ. Prediction of the reverse micellar extraction of papain using dissipative particle dynamics simulation. *Appl Biochem Biotechnol* 2017;181(4):1338–46.
- [337] He P, Qiao R. Self-consistent fluctuating hydrodynamics simulations of thermal transport in nanoparticle suspensions. *J Appl Phys* 2008;103(9):094305.
- [338] Abu-Nada E. Dissipative particle dynamics investigation of heat transfer mechanisms in Al₂O₃-water nanofluid. *Int J Therm Sci* 2018;123:58–72.
- [339] Li Z, Drazer G. Hydrodynamic interactions in dissipative particle dynamics. *Phys Fluids* 2008;20(10):103601.
- [340] Bin Szali MA, Kobayashi Y, Taniguchi Y, Nakashima T, Arai N. Self-assembled morphology of tripod nanoparticle solutions: the effect of arm length and hydrophobic ratio. *Mol Syst Des Eng* 2018;3(3):572–80.
- [341] Elliott JA, Windle AH. A dissipative particle dynamics method for modeling the geometrical packing of filler particles in polymer composites. *J Chem Phys* 2000;113(22):10367–76.
- [342] Gibson JB, Chen K, Chynoweth S. Simulation of particle adsorption onto a polymer-coated surface using the dissipative particle dynamics method. *J Colloid Interface Sci* 1998;206(2):464–74.
- [343] Laradji M, Hore MJA. Nanospheres in phase-separating multicomponent fluids: a three-dimensional dissipative particle dynamics simulation. *J Chem Phys* 2004;121(21):10641–7.
- [344] He LL, Zhang LX, Liang HJ. The effects of nanoparticles on the lamellar phase separation of diblock copolymers. *J Phys Chem B* 2008;112(14):4194–203.
- [345] Chen H, Ruckenstein E. Nanoparticle aggregation in the presence of a block copolymer. *J Chem Phys* 2009;131(24):244904.
- [346] Liu D, Zhong C. Cooperative self-assembly of nanoparticle mixtures in lamellar diblock copolymers: a dissipative particle dynamics study. *Macromol Rapid Commun* 2006;27(6):458–62.
- [347] Chen S, Guo C, Hu GH, Liu HZ, Liang XF, Wang J, et al. Dissipative particle dynamics simulation of gold nanoparticles stabilization by PEO-PPO-PEO block copolymer micelles. *Colloid Polym Sci* 2007;285(14):1543–52.
- [348] Chen H, Ruckenstein E. Aggregation of nanoparticles in a block copolymer bilayer. *J Colloid Interface Sci* 2011;363(2):573–8.
- [349] He LL, Pan ZQ, Zhang LX, Liang HJ. Microphase transitions of block copolymer/nanorod composites under shear flow. *Soft Matter* 2011;7(3):1147–60.
- [350] Spaeth JR, Kevrekidis IG, Panagiotopoulos AZ. A comparison of implicit- and explicit-solvent simulations of self-assembly in block copolymer and solute systems. *J Chem Phys* 2011;134(16).
- [351] Bianchino E, Pioletti S, Mavelli F, Curri ML, Striccoli M. DPD simulations of PMMA-oleic acid mixture behaviour in organic capped nanoparticle based polymer nanocomposite. *Macromol Symp* 2009;286:156–63.
- [352] Huang J, Luo M, Wang Y. Dissipative particle dynamics simulation on a ternary system with nanoparticles, double-hydrophilic block copolymers, and solvent. *J Phys Chem B* 2008;112(22):6735–41.
- [353] Huang LY, Yu YS, Lu X, Ding HM, Ma YQ. Designing a nanoparticle-containing polymeric substrate for detecting cancer cells by computer simulations. *Nanoscale* 2019;11(5):2170–8.
- [354] Magee JE, Siperstein FR. Formation of ordered mesoporous materials under slow aggregation conditions. *J Phys Chem C* 2009;113(5):1680–5.
- [355] Karatrantos A, Clarke N, Composto RJ, Winey KI. Topological entanglement length in polymer melts and nanocomposites by a DPD polymer model. *Soft Matter* 2013;9(14):3877–84.
- [356] Zhou Y, Long XP, Zeng QX, Zhang CY. A novel nanocage from the cooperative self-assembly of coil-rod-coil triblock copolymers and nanoparticles. *Macromol Rapid Commun* 2013;34(10):883–6.
- [357] Ma SY, Hu Y, Wang R. Amphiphilic block copolymer aided design of hybrid assemblies of nanoparticles: nanowire, nanoring, and nanocluster. *Macromolecules* 2016;49(9):3535–41.
- [358] Yang JY, Hu Y, Wang R, Xie DQ. Nanoparticle encapsulation in vesicles formed by amphiphilic diblock copolymers. *Soft Matter* 2017;13(43):7840–7.
- [359] Nair N, Park M, Handgraaf JW, Cassiola FM. Coarse-grained simulations of polymer-grafted nanoparticles: structural stability and interfacial behavior. *J Phys Chem B* 2016;120(35):9523–39.
- [360] Vo MD, Papavassiliou DV. The effects of shear and particle shape on the physical adsorption of polyvinyl pyrrolidone on carbon nanoparticles. *Nanotechnology* 2016;27(32).
- [361] Kobayashi Y, Arai N. Janus or homogeneous nanoparticle mediated self-assembly of polymer electrolyte fuel cell membranes. *RSC Adv* 2018;8(33):18568–75.
- [362] Guskova OA, Pal S, Seidel C. Organization of nanoparticles at the polymer brush-solvent interface. *Europhys Lett* 2009;88(3):38006.
- [363] Khani S, Jamali S, Boromand A, Hore MJA, Maia J. Polymer-mediated nanorod self-assembly predicted by dissipative particle dynamics simulations. *Soft Matter* 2015;11(34):6881–92.
- [364] Nguyen VP, Phi PQ, Choi ST. Tribological behavior of grafted nanoparticle on polymer-brushed walls: a dissipative particle dynamics study. *ACS Appl Mater Interfaces* 2019;11(12):11988–98.
- [365] Brun Y, Foster P. Characterization of synthetic copolymers by interaction polymer chromatography: separation by microstructure. *J Sep Sci* 2010;33(22):3501–10.
- [366] Burgess S, Santo KP, Brun Y, Neimark AV. Nanoparticle flow in polymer grafted channels. *J Phys Chem C* 2020;124(2):1478–83.
- [367] Tian FL, Yue TT, Li Y, Zhang XR. Computer simulation studies on the interactions between nanoparticles and cell membrane. *Sci China-Chem* 2014;57(12):1662–71.
- [368] Djohari H, Dormidontova EE. Kinetics of nanoparticle targeting by dissipative particle dynamics simulations. *Biomacromolecules* 2009;10(11):3089–97.
- [369] Li Y, Yue TT, Yang K, Zhang XR. Molecular modeling of the relationship between nanoparticle shape anisotropy and endocytosis kinetics. *Biomaterials* 2012;33(19):4965–73.
- [370] Li Y, Yuan B, Yang K, Zhang XR, Yan B, Cao DP. Counterintuitive cooperative endocytosis of like-charged nanoparticles in cellular internalization: computer simulation and experiment. *Nanotechnology* 2017;28(8).
- [371] Liu F, Wu D, Chen K. The cooperative effect analysis when nanoparticles enter a biological cell. *Nano* ;14(4).
- [372] Yue T, Zhang X. Molecular understanding of receptor-mediated membrane responses to ligand-coated nanoparticles. *Soft Matter* 2011;7(19):9104–12.
- [373] Burgess S, Vishnyakov A, Tsovkov C, Neimark AV. Nanoparticle-engendered rupture of lipid membranes. *J Phys Chem Lett* 2018;9(17):4872–7.
- [374] Burgess S, Wang Z, Vishnyakov A, Neimark AV. Adhesion, intake, and release of nanoparticles by lipid bilayers. *J Colloid Interface Sci* 2020;561:58–70.
- [375] Yong X, Crabb EJ, Moellers NM, Balazs AC. Self-healing vesicles deposit lipid-coated Janus particles into nanoscopic trenches. *Langmuir* 2013;29(52):16066–74.
- [376] Shen ZQ, Ye HL, Kroger M, Li Y. Aggregation of polyethylene glycol polymers suppresses receptor-mediated endocytosis of PEGylated liposomes. *Nanoscale* 2018;10(9):4545–60.
- [377] Li ZL, Gorfé AA. Receptor-mediated membrane adhesion of lipid-polymer hybrid (LPH) nanoparticles studied by dissipative particle dynamics simulations. *Nanoscale* 2015;7(2):814–24.
- [378] Pons-Siepermann IC, Glotzer SC. Design of patchy particles using ternary self-assembled monolayers. *Soft Matter* 2012;8(23):6226–31.
- [379] Alasiri H, Chapman WG. Dissipative particle dynamics (DPD) study of the interfacial tension for alkane/water systems by using COSMO-RS to calculate interaction parameters. *J Mol Liq* 2017;246:131–9.
- [380] Kauzlaric D, Meier JT, Español P, Succi S, Greiner A, Korvink JG. Bottom-up coarse-graining of a simple graphene model: the blob picture. *J Chem Phys* 2011;134(6):064106.
- [381] Shi K, Lian C, Bai Z, Zhao S, Liu H. Dissipative particle dynamics study of the water/benzene/caprolactam system in the absence or presence of non-ionic surfactants. *Chem Eng Sci* 2015;122:185–96.
- [382] Ruiz-Morales Y, Mullins OC. Coarse-grained molecular simulations to investigate asphaltene at the oil–water interface. *Energy Fuel* 2015;29(3):1597–609.
- [383] Plimpton S. Fast parallel algorithms for short-range molecular dynamics. *J Comput Phys* 1995;117(1):1–19.
- [384] Limbach HJ, Arnold A, Mann BA, Holm C. ESPResSo—an extensible simulation package for research on soft matter systems. *Comput Phys Commun* 2006;174(9):704–27.
- [385] Seaton MA, Anderson RL, Metz S, Smith W. DL_MESO: highly scalable mesoscale simulations. *Mol Simul* 2013;39(10):796–821.
- [386] Anderson JA, Glaser J, Glotzer SC. HOOMD-blue: a python package for high-performance molecular dynamics and hard particle Monte Carlo simulations. *Comput Mater Sci* 2020;173:109363.
- [387] Zhu Y-L, Liu H, Li Z-W, Qian H-J, Milano G, Lu Z-Y. GALAMOST: GPU-accelerated large-scale molecular simulation toolkit. *J Comput Chem* 2013;34(25):2197–211.